Fakultät für Elektrotechnik und Informationstechnik
Professur für Neuroelektronik

Microwire arrays for studying the influence of temperature gradients on the cellular behavior

Truong Ka My Dang

Vollständiger Abdruck der von der Fakultät für Elektrotechnik und Informationstechnik der Technischen Universität München zur Erlangung des akademischen Grades eines

Doktor-Ingenieurs (Dr.-Ing.)

genehmigten Dissertation.

Vorsitzende: Prof. Dr.-Ing.Christian Jirauschek

Prüfer der Dissertation:

1. Prof. Dr. Bernhard Wolfrum
2. Prof. Dr. Oliver Hayden

Die Dissertation wurde am 13.08.2018 bei der Technischen Universität München eingereicht und durch die Fakultät für Elektrotechnik und Informationstechnik am 03.12.2018 angenommen.

ABSTRACT

Temperature plays an important role in regulating the biological function of cellular development. Over the past few decades, the development of microfabrication technology has enabled highly localized temperature control at the scale of a few microns. This allows the study of thermal influences on biological microsystems. In this context, the present thesis investigates the changes of cellular behavior depending on temperature gradients using microwire arrays. In addition, the thesis also introduces a sacrificial layer approach to fabricate microchannels for studying neuronal guidance. The integration of the microwire array into microchannels presented in this thesis proposes a novel method for governing neuronal networks under the influences of temperature gradients.

The first part of this thesis presents the application of microwire arrays to study the effects of localized temperature gradients on signal propagation in cardiac cell networks. In order to investigate the effects of temperature on cellular networks, a monolayer of cardiomyocytes is cultured onto the chip. The localized temperature is induced by using a power supply connected to microwire arrays. A calcium imaging method is performed to evaluate changes in signal propagation under local heat stimulation. Calcium signals are recorded using a high speed and low light camera. Also in this part, the velocity of the calcium signal propagation in cellular networks is locally increased upon heat stimulation. Additionally, this part presents a relocation of the pacemaker cell and a deformation of the calcium wavefront caused by an increase of the local temperature.

In the second part, the growth of neurons is investigated under the influence of temperature gradients. In this study, the PC12 neuron-like cells are cultured on the microwire array chip. The effects of temperature gradients on neurons are examined, focusing on the speed and direction of neurite outgrowth. The growth of neurites under local heat stimulation is recorded using a time-lapse imaging method. The images are then analyzed to estimate the development of neurons within temperature gradients. The result indicates that the growth speed of neurons increases with heat stimulation. Moreover, the evidence that temperature gradients affect the growth direction of neurites is observed in a long-term period experiment (24 h after heating).

The last part of the thesis presents a promising fabrication approach, based on standard clean room fabrication and sacrificial layer etching, for combining microwire arrays with a set of perpendicular axon-guiding microchannels. This approach enables the positioning of neurites, as well as control over their polarity. In particular, an array of asymmetrical microchannels with wide inlets and narrow outlets is fabricated to allow neurites to grow in one direction. The experiment with neurites from PC12 cells demonstrates that neurites can grow from the entrance to the exit of the microchannels. Furthermore, the fabrication of microchannels, integrated with microwire arrays, allows the study of temperature gradients effects on the formation of functional neuronal networks.

Overall, this thesis focuses on investigating thermal impacts on cellular behavior using the localized heating generated by microwire arrays. This work demonstrates the important role of microscopic heating in regulating signal propagation, as well as the growing properties of cellular networks. Specifically, the temperature highly confined in a small area governs the calcium signal propagation of cardiomyocytes and the growth of neurites towards the heat source. Other than that, concerning the technical aspects, the fabrication of thin microwire enables us to control high temperature in a microscopic area. Furthermore, the fabrication of sacrificial microchannels contributes benefits for neuronal guidance,

such as reducing a number of fabrication steps and improving the adhesion between microchannels and the chip's surface.

CONTENTS

CHAPTER 1

INTRODUCTION

Temperature is an important physical parameter affecting every life process. In mammals, temperature is well known as an essential vital sign that indicates sickness or health. Additionally, temperature plays a crucial role in regulating a variety of mechanisms in biological systems. It has been demonstrated that cells decrease their growth rate under low temperature conditions [1, 2]. Conversely, the proliferation rate of cells rises in response to an increase of ambient temperature [3]. In line with this, the previous study of Kang *et al.* [4] shows that temperature has a comprehensive influence on intracellular calcium dynamics, which manipulates most biochemical processes such as neural transmission, muscle contraction, and heart beat. In fact, many studies have demonstrated that temperature has a profound effect on living systems such as birth length [5], life span [6] and aging-associated diseases [7].

Together with temperature itself, temperature gradients also play a significant role in regulating the living systems. Spatial and temporal variation of temperature induces changes in the nature of chemical reactions and alters the configuration of atoms that build up nucleic acids, proteins, lipids and other biomolecules [8]. A spatial temperature gradient has been demonstrated to be a guidance cue for the migration of organisms. Many studies indicate that thermotaxis can cause an organism to move up or down according to a gradient temperature [9–11]. An exper-

iment with *Caenorhabditis elegans*, a transparent nematode (roundworm), has shown that *Caenorhabditis elegans* migrates to a certain temperature when subjected to a spatial temperature gradient [12]. While the temperature sensitivity of organisms is well known, it has been not well understood how individual cells respond to different temperatures. The study of temperature sensitivity at a cellular level has been a challenging engineering problem, possibly due to the lack of microscopic systems which can produce temperature at microscales.

Over the past few decades, microtechnology has been developed as a new approach for studies in biophysics and physical chemistry [13–15]. Microtechnology employs fabrication methods (e.g. photolithography) to create microsystems on chips, such as lab-on-a-chip or micro-total-analysis-systems. As a result of the development of microelectromechanical systems (MEMS) and microfluidic devices, scientists are now able to investigate and manipulate biological systems at a cellular level [16–19]. MEMS offer the ability to precisely manipulate cells on microscales, which makes it possible to study cellular interactions with physical and chemical microenvironments surrounding them [17, 20]. These interactions offer deep insights into the fundamental behaviors of biological microsystems, such as pacemaker cells, calcium concentrations, neuronal outgrowth, cellular viability, and cellular locomotion.

This thesis aims to study cellular networks regulating and responding to local heating generated by microwire array chips. Particularly, the influence of localized temperature gradients on calcium signal propagation in cardiomyocytes will be investigated. A rise of local temperature will cause an increase in the propagation speed of these signals. This results in a deformation of the calcium wave in the cardiac networks. Additionally, the local temperature will be used to stimulate cells in the heated zone. This stimulation causes the cells to become more active. This results in the relocation of pacemaker cells to the heated area. Moreover, the effects of temperature gradients on neuron-like cells will be examined in this work. Temperature gradients could accelerate the speed of neurite outgrowth and be a guidance cue for neurites. To access cellular

behavior in response to localized heating, a fabrication approach which combines microheaters and microfluidic channels for neurite guidance will be introduced in this thesis.

The local heating with high spatial accuracy induced from microwire array chips provides an effective approach to study heat effects at cellular levels. Studying the influence of heat on living cells at a microscale creates a pathway to understanding how cells are sensed by the adjacent cells and communicate with each other in response to temperature changes.

The thesis contains six chapters. In the introduction, the motivation for the research is presented. The second chapter takes up the fundamentals and methods. This chapter describes the basic concepts of biology and physics which are used in the following experiments and studies. The third chapter presents the study of local heat stimulation for modulating signal propagation in cardiomyocyte-like cell (HL-1 cells) networks. The study of the effect of heat activation on the guidance of neurite outgrowth will be conducted in the fourth chapter. The next chapter describes the fabrication of microchannels perpendicular to microwire arrays for studying the effects of thermal gradients on neurite outgrowth and neuronal guidance. The last chapter presents the conclusions and outlook, which suggests possible applications of microwire arrays in studies of neuronal regeneration, cell migration, and dopamine releases.

CHAPTER 2

FUNDAMENTALS & THEORY

2.1 THE CELL

2.1.1 THE CELL STRUCTURE

The cell is the basic unit of biological activity. The name "cell" was suggested by Robert Hooke in 1665. The meaning is derived from the Latin *cella* which means storeroom or chamber [21]. There are two different types of cells, prokaryotic cells and eukaryotic cells. The structure of prokaryotic cells is very simple, whereas the structure of eukaryotic cells is more complex. The cells from plants and animals are all eukaryotic cells. Since the cells used in this work are cardiomyocyte-like cells and neuron-like cells, only the structure of eukaryotic cells is described in detail.

The size of eukaryotic cells is between 1 and 100 µm. The structure of eukaryotes is shown in Figure 2.1. Surrounding the cell is the plasma membrane, which protects and separates the cell from the external environment. The cell membrane contains many biomolecules such as proteins. These proteins form ion channels which are embedded in the membrane to allow substances to cross through the cell membrane. Inside the cell, many subcellular components work together to maintain the cell's activity. The nucleus contains genetic information, which controls the activity of the cell by regulating gene expression. Gene expression is the process used to synthesize a functional protein from a gene [22]. Within the nucleus is the nucleolus where ribosomes are synthesized. Ribosomes are found "free" in the cytoplasm or attached to the rough endoplasmic reticulum to produce proteins.

Another type of endoplasmic reticulum is the smooth endoplasmic reticulum, which plays an important role in the metabolism and the synthesis of lipids. In muscle cells, the sarcoplasmic reticulum is a special type of the smooth endoplasmic reticulum that stores and releases calcium for moderating the excitation and contraction process. Proteins produced in the endoplasmic reticulum are transported to the membrane or lysosomes by vesicles via the Golgi apparatus. Inside the lysosome,

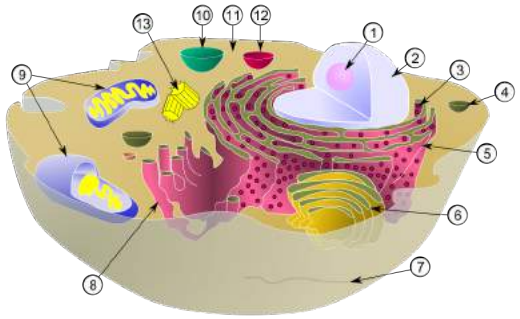

FIGURE 2.1: Structure of the eukaryotic cell contains many structural subunits: 1) Nucleolus, 2) Nucleus, 3) Ribosome, 4) Vesicle, 5) Rough endoplasmic reticulum, 6) Golgi apparatus, 7) Cytoskeleton, 8) Smooth endoplasmic reticulum, 9) Mitochodria, 10) Vacuoles, 11) Cytoplasm, 12) Lysosomes, 13) Centriole.

biomolecules, including macromolecules such as proteins, nucleic acids, or small molecules, are disassembled by hydrolytic enzymes. This process is similar to the activity of digestion [22].

Besides the degradation process of molecules, lysosomes also participate in recycling processes inside the cell. To maintain the shape and the size of the cell, the cytoskeleton is present in all cells. The cytoskeleton is a dynamic structure which is involved in the rapid growth of the cell. Three main kinds of cytoskeletal filaments are microfilaments, microtubules, and intermediate filaments [22]. Microfilaments are also called actin filaments, which are made of actin proteins that act as tracks for the movement of myosin molecules.

In muscle cells, the binding of myosin on actin generates forces which perform the contraction in cardiomyocyte. Microtubules serve as tracks for organelles to move along within the cell. Interactions between microtubules and microflilaments play a crucial role in processes of neurite outgrowth and neurite guidance [23]. Intermediate filaments together with microfilaments maintain the cell shape and form cell-cell connections. The centriole consists of two bundles of microtubules which are involved in cell polarity. To supply energy for the cell, mitochondria generate the energy and transform it into adenoine triphosphate (ATP). For this reason, they are sometimes considered as the “powerhouse” of the cell.

2.1.2 MEMBRANE POTENTIAL

As described in subsection 2.1.1, numerous types of ion channels are embedded in the cell membranes. These ion channels serve as conduits that regulate the flow of ions through the cell membrane. The influx and efflux of ions through the cell membrane result in a difference in electrical potential between the intracellular and extracellular environment. This potential difference is called membrane potential.

Signals are transmitted through the cell by opening or closing the ion channels in the membrane, causing a local change of membrane potential. The movement of ions results in an asymmetric distribution, causing ion gradients to cross through the cell membrane. Cells control and use the ion gradients in different ways to help them communicate with their surrounding environment. In electrogenic cells such as neurons and muscle cells, the membrane potential triggers action potentials to transmit signals.

When the influx and the efflux of ions are in balance, the cell is at rest and this state is called the resting membrane potential. The equilibrium distribution of ions through the membrane is maintained by the movement of ions. Three important ions which contribute to the membrane potential are sodium (Na^+), potassium (K^+) and chloride (Cl^-). These ions are distributed inside and outside of the cell. Their concentrations are given in Table 2.1 [24]. Since the membrane is more permeable for K^+ than for other ions, the outflow of K^+ is the dominant process needed to maintain the resting potential. The voltage at which the net ion flow through the membrane is zero is called the equilibrium potential. The

TABLE 2.1: Approximate concentrations of intracellular and extrallular ions in mammalian cells (Note: these are concentrations of free ions).

Ion	Intracellular concentration (mM)	Extracellular concentration (mM)
Na^+	15	140
K^+	140	4.5
Cl^-	10	120

equilibrium potential of an ion can be calculated using the Nernst equation. This equation calculates the equilibrium potential for an ion based on the charge of the ion and its concentration gradient across the membrane. For example, the equilibrium potential for K^+ can be calculated as follows:

$$E_{\mathrm{eq},K^+} = \frac{RT}{zF_a} \ln \frac{[K^+]_{\mathrm{out}}}{[K^+]_{\mathrm{in}}}, \tag{2.1}$$

where E_{eq,K^+} is the equilibrium potential for K^+ (V), R is the universal gas constant ($\mathrm{J\,mol^{-1}\,K^{-1}}$), T is the absolute temperature (K), z is the number of elementary charges of the ion, F_a is the Faraday constant, $[K^+]_{\mathrm{out}}$ is the extracellular concentration of ion K^+, and $[K^+]_{\mathrm{in}}$ is the intracellular concentration of ion K^+.

The above equation is calculated only for K^+. In real cells, the resting membrane potential is estimated for the ions which give the strongest current through the membrane. In fact, there are contributions from ions Cl^- and Na^+; therefore three ions K^+, Cl^- and Na^+ must be considered. The resting membrane potential for these three ions is given by the Goldman-Hodgkin-Katz equation:

$$E_M = \frac{RT}{F_a} \ln \frac{P_K[K^+]_{\mathrm{out}} + P_{Na}[Na^+]_{\mathrm{out}} + P_{Cl}[Cl^-]_{\mathrm{in}}}{P_K[K^+]_{\mathrm{in}} + P_{Na}[Na^+]_{\mathrm{in}} + P_{Cl}[Cl^-]_{\mathrm{out}}}, \tag{2.2}$$

where P_K, P_{Na} and P_{Cl} are the relative permeabilities of the ion K^+, Na^+ and Cl^- respectively. Normally, permeability values are reported as relative permeability with P_K. In most cells at resting membrane potential, the permeability of K^+ is higher than Na^+ and Cl^-. The charge z is not explicitly present as it was considered within the terms of the individual K^+. A sketch of various ion channels embedded in the plasma membrane is shown in Figure 2.2.

2.1.3 ACTION POTENTIALS AND SIGNAL PROPAGATION

As described in subsection 2.1.2, the electrical potential difference is caused by the different concentrations of ions through the membrane. Rapid changes in the membrane potential result in changes in the volt-

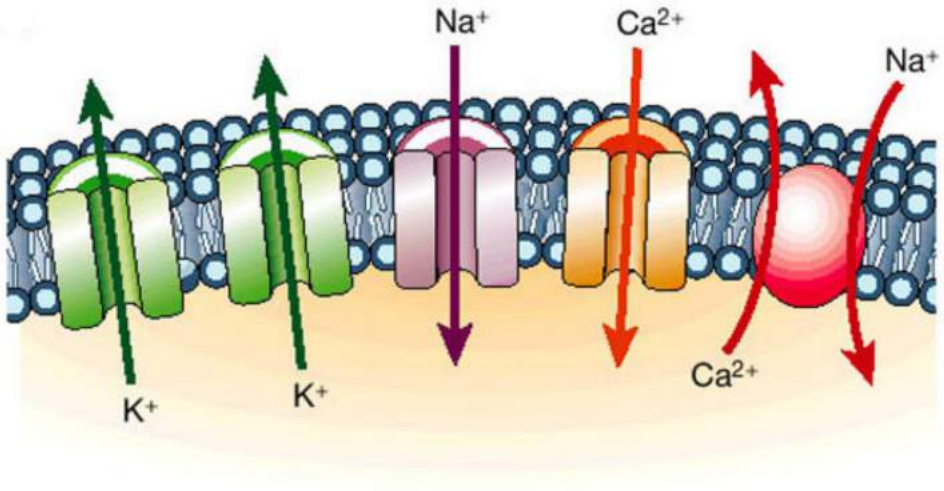

FIGURE 2.2: Schematic of the ion channels are embedded in the plasma membrane. Image reprinted with permission from [25].

age through the membrane, which leads to the propagation of action potentials. The action potential can be divided into three main phases. A typical action potential is shown in Figure 2.3. The initial phase is a rapid change in membrane potential from resting state to the equilibrium potential of the ions. This phase is called depolarization. In this phase, a stimulus causes the channels to open, leading to an influx of Na^+ ions, which in turn produces an increase in the membrane potential from negative to positive values. For example, in neuronal cells, the membrane potential changes from $-70\,\mathrm{mV}$ at rest to $40\,\mathrm{mV}$ in the depolarization phase [26].

The second phase is called repolarization, which is a return to resting membrane potential. In this phase, potassium channels are opened, leading to an outward flow of K^+ ions, which causes the membrane to return to the resting state. The third phase is a short period of time after repolarization, which is called the refractory period. In this phase, sodium channels are inactivated and some potassium ion channels are still open to let the K^+ ions flow out of the membrane. After this phase, Na^+/K^+ pumps eventually bring the membrane back to the resting state.

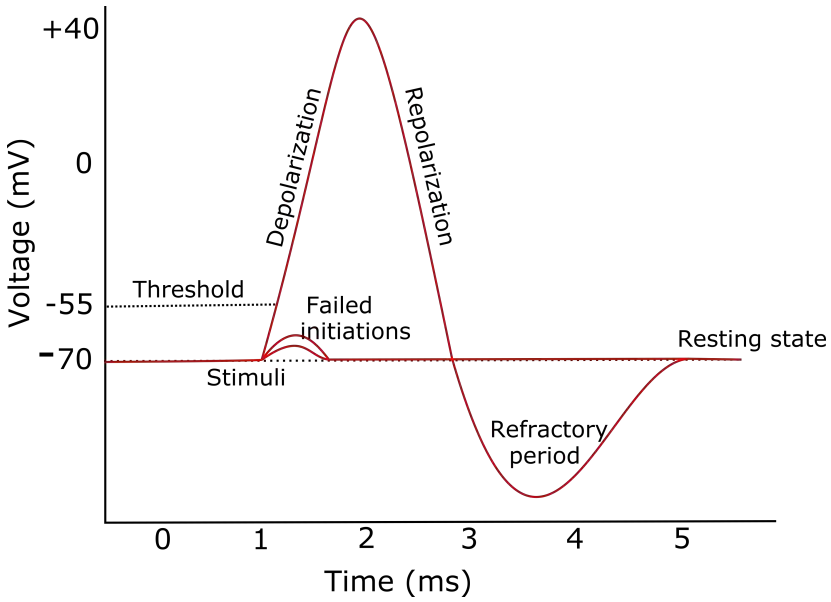

FIGURE 2.3: A schematic shows various phases of a typical action potential.

CARDIAC ACTION POTENTIALS Cardiac action potentials differ from action potentials found in other electrogenic cells, which are initiated by nervous activity. The cardiac action potential is generated by specific cells within cardiac cells (pacemaker cells). A typical action potential of cardiac cells is shown in Figure 2.4. As shown from the schematic, there are five phases of the cardiac action potential. Before the action potential occurs, the membrane potential maintains at a constant level which is called resting membrane potential (phase 4). At this phase, the membrane potential results from the balance of the influx of ions (e.g. sodium and calcium) and the efflux of ions (e.g. potassium). Following a stimulus of the membrane, the fast sodium channels open, causing an increase in sodium influx, leading to the depolarization of the cell membrane (phase 0). As the sodium channels rapidly close, the potassium channels open and close rapidly, allowing a small flow of potassium ions out of the cell and leading to the membrane potential slightly more negative (phase 1). The abrupt depolarization triggers the opening of calcium and potassium channels, which allows the calcium influx and the potassium efflux. The opening of calcium channels and potassium channels results in a balance of the calcium influx and the potassium efflux. This results in a plateau

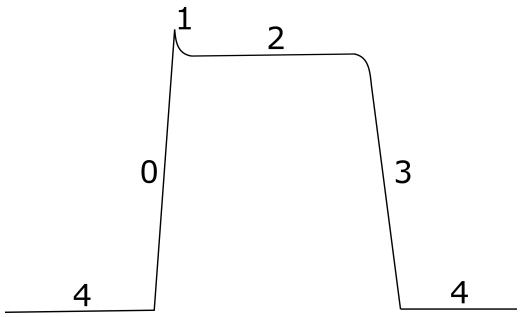

FIGURE 2.4: Schematic of an action potential from a cardiomyocyte. **0** Depolarisation. **1** First repolarization. **2** Plateau. **3** Second repolarization. **4** Resting membrane potential.

of the action potential (phase 2). As the calcium channels close, the potassium channels still open causing the potassium efflux, which leads to a full repolarization of the cell (phase 3). Finally, the potasium channels close and the membrane potential reaches the resting state of membrane potential (phase 4).

PACEMAKER CELLS Some cells can generate action potentials without any stimulus, and these are called pacemaker cells. In cardiac cells, these cells reside in the sinoatrial node of the heart, regulating the beating rate. At the resting state of an action potential, the pacemaker cells generate a gradual increase of the membrane potential by allowing an influx of sodium ions. When the membrane potential reaches the threshold $-40\,\mathrm{mV}$, it activates an opening of the calcium channels. The influx of calcium ions initiates depolarization of the cell. Subsequently, potassium channels open, allowing an efflux of potassium ions and establishing the repolarization state of the cell. Once the cell is repolarized, leak channels (e.g sodium channels) cause an instability of the resting potential and result in a firing of the next action potential [27]. The unstable resting potentials of pacemaker cells enable spontaneous depolarizations which are relatively fast and repeat themselves regularly. The fast depolarizations of pacemaker cells control contractile cardiomyocytes by means of a mechanism called overdrive suppression, which states that the cells with the most rapid frequency of depolarization control the overall beating of

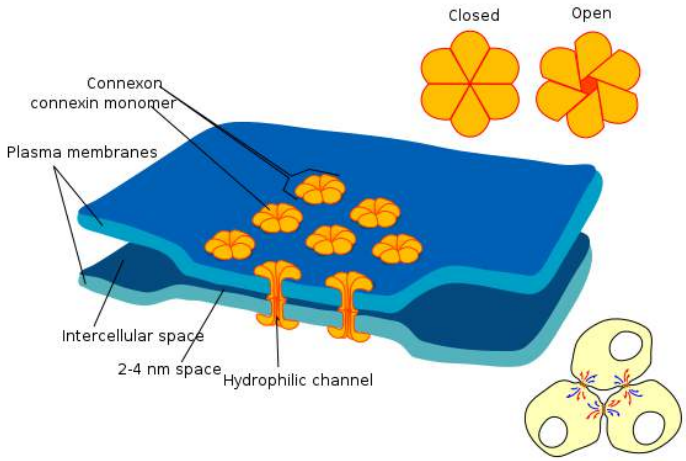

FIGURE 2.5: Schematic of a gap junction. Adapted from [31].

cardiac cells [27]. The pacemaker cells are connected to neighboring cells via gap junctions (see below), which allow them to locally depolarize adjacent cells. This function allows pacemaker cells to control contractions in cardiomyocytes [28].

2.1.4 SIGNAL PROPAGATION IN CARDIAC CELLS

GAP JUNCTIONS Gap junctions are channels shared with the plasma membrane of neighboring cells (see Figure 2.5). They are formed by proteins called connexons; each connexon consists of six proteins called connexins. Molecules, ions, and electrical impulses can pass through these channels, allowing cells to communicate with each other. In this way, when the cells are depolarized above a certain threshold, this depolarization triggers the propagation of action potentials in the next cells through the gap junctions. The propagation of these signals is very fast. The propagation speed of cardiomyocyte-like cells (HL-1 cells) is in the range of $7-30\,\mathrm{mm\,s^{-1}}$ [29, 30].

EXCITATION-CONTRACTION COUPLING OF CARDIAC CELLS In cardiac cells, the excitation-contraction coupling is a key process of turning electrical excitations into mechanical contractions. This process is initiated by

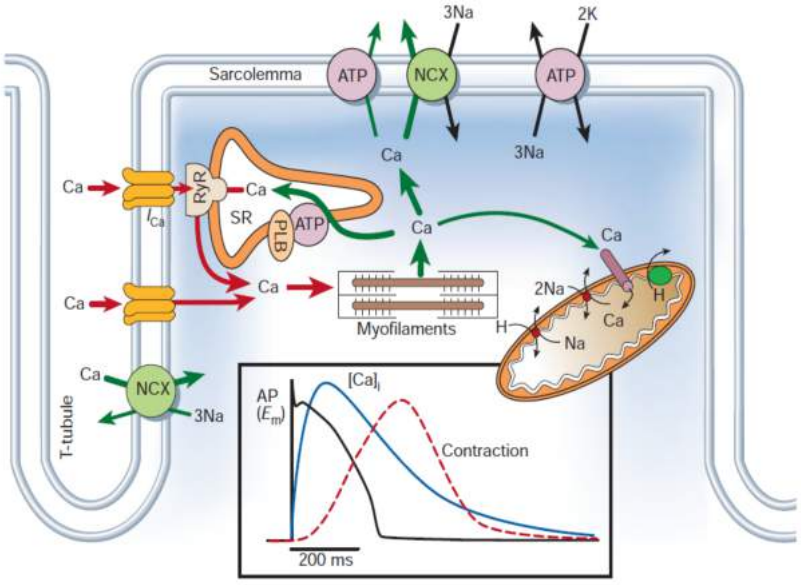

FIGURE 2.6: Schematic of excitation-contraction coupling of cardiac cells. Image reprinted with permission from [32].

local membrane depolarization, causing calcium-induced calcium release from the sarcoplasmic reticulum (SR). The released calcium activates myofilaments that eventually initiate the contraction as explained below.

Membrane depolarization during the action potential leads to an opening of voltage-gated L-type calcium channels (Figure 2.6). The opening of L-type calcium channels, located in the T-tubule membrane, causes an influx of calcium, which results in the increase of calcium concentration. The inward flow of calcium ions binds to ryanodine receptors (RyR) located on the SR, triggering intracellular calcium release from the sarcoplasmic reticulum (SR). The increase in the free intracellular calcium allows calcium ions to bind to troponin C, a protein of the thin filament. This binding causes tropomyosin to shift, exposing the myosin binding site on the actin. Once the myosin binds to the actin, a force is generated. At the end of the cycle, to relax the contraction, calcium is released from troponin-C and then either pumped out of the cell by the sodium-calcium exchanger or pumped into the SR by the sarcoplasmic reticulum calcium ATPase (SERCA) pump [33].

This is the explanation of the process of contraction in an individual cardiomyocyte. In the standard experiment of this thesis, these cells are grown as a confluent layer to form gap junctions. Therefore, signals can propagate across the cell layer via gap junctions (see above).

2.1.5 TRPV CHANNELS AS TEMPERATURE SENSORS

Temperature sensing allows organisms to adapt to changes of environmental conditions. Over the past years, it is known that the temperature is sensed by means of ion channels located in cellular membrane [34, 35]. The ion channels are sensitive to heat called thermal-transient receptor potential (TRPV) channels. The temperature dependence of these TRPV channels is estimated based on Q_{10} value. Q_{10} is a change in the rate of reaction when the temperature rises by 10 °C. The Q_{10} value is calculated as follows:

$$Q_{10} = \left(\frac{R_2}{R_1}\right)^{\frac{10}{T_2 - T_1}}, \tag{2.3}$$

where R_1 and R_2 are the rate of the reaction at temperature T_1 and T_2, respectively.

The thermal TRPV channels are characterized for having greater thermal sensitivity with Q_{10} values much higher than 2 ($6 < Q_{10} < 30$) [36, 37]. There are four different types of thermal-sensing ion channels in the TRPV family called TRPV1, TRPV2, TRPV3, and TRPV4. The structure of these TRPV channels is similar to the TRP (Transient Receptor Potential) ion channels superfamily, which consists of proteins with six transmembrane domains. These groups of proteins are assembled to form cation-permeable ion channels. The rise of temperature causes these ion channels to open, leading to the influx of ions through open channels. TRPV1 ion channels are calcium-permeable receptors activated by capsaicin with temperature threshold of 43 °C. The activation of TRPV1 is relatively fast with the time response in a range of a few milliseconds. If the temperature is kept constant for a while, the sensitivity of the channels is decreased. The TRPV2 ion channels are activated by noxious tem-

perature up to 53 °C. The temperature for activating TRPV3 channels is in a range from 23–39 °C, which is lower than the temperature threshold of TRPV1 and TRPV2 channels. The final member in the TRPV family is the TRPV4. The TRPV4 channels are open when they are activated with the temperature from 22 °C. However, these channels desensitize with the temperature over the range of 24–36 °C [38].

2.2 CELL MODELS

2.2.1 HL-1 CELLS: A CARDIOMYOCYTE CELL LINE

HL-1 cells were derived from the AT-1 mouse atrial cardiomyocyte tumor by Dr. William Claycomb [39]. The cells can be passaged several times and are able to maintain the contraction activity of cardiac cells during continuous passage in culture. In addition, the cells can be stored in liquid nitrogen and recovered from frozen stocks. HL-1 cells show spontaneous contraction when they form a confluent monolayer. The beating frequency is driven by pacemaker cells. There are about 30 % of these cells detected in HL-1 cells [40]. HL-1 cells have been used in a variety of model systems to study functions of cardiac biology at the cellular level [28]. Therefore, in order to study the influence of temperature on cardiomyocytes, HL-1 cells were chosen as a model system for this work.

2.2.2 PC12 CELLS AS A MODEL FOR NEURONS

PC12 is a cell line derived from a pheochromocytoma of the rat adrenal medulla, which is part of the adrenal gland. This cell line was first established by Green and Tischler in 1976 [41]. Since then, PC12 cells have been widely used in neuronal studies because they are able to be passaged several times in culture. Furthermore, they are much easier to culture compared to their neuronal counterparts. PC12 cells tend to form small clumps in the culture medium. An important feature of PC12 cells is their ability to form neurites in response to nerve growth factor (NGF). The treatment of NGF causes an increase of the microtubule assembly,

which plays a crucial role in the neuronal extension [42]. NGF-treated PC12 cells change their phenotype and exhibit a number of properties characteristic of sympathetic neurons [43]. The neurites growing from NGF-treated PC12 cells elongate their length during their development and connect to other neurites to form neuronal networks. The growing neurites of PC12 cells are terminated at their distal end by growth cones, which are motile expansions containing filopodia and lamelipodia [44]. They are able to explore the environment and orientate neurites [45]. Because of these properties, PC12 cells treated with NGF have been commonly used as a model for studies of neurite outgrowth [46, 47].

2.3 DEVICES AND FABRICATION TECHNIQUES

In this work, microwire array chips are used to induce microscopic thermal stimulation for studying the influence of temperature gradients on cellular behaviors such as cardiac cells and neurons. In order to study the impact of temperature gradients on neurite outgrowth, it is necessary to fabricate channel systems for neuronal guidance. These microchannels are integrated with microwire arrays to employ local heat activation of neurites growing inside microchannels. For this purpose, microfluidic channels are fabricated perpendicularly on the surface of microwire array chips. The following section will introduce fabrication techniques used for producing microwire array chips and microchannels.

2.3.1 MICROWIRE ARRAY

FABRICATION TECHNIQUE: PHOTO-LITHOGRAPHY The photolithographic method, also called optical lithography, is a process used in micro-fabrication for patterning specific structures on a substrate. The geometric structures are directly transferred from a photomask to the substrate using an ultraviolet light (UV) exposure system and photosensitive materials (photoresist). The photoresist consists of three components, which include a base resin, a photoactive compound, and a solvent. The photoresist can be classified into positive and negative resists depending

on changes in its properties in response to the light exposure (see Figure 2.7). Positive photoresists become soluble in the developer and are easily removed from particular regions exposed by UV light. Conversely, negative photoresists become less soluble and form cross-linking after being exposed. Thus, the unexposed areas can be removed in the developer. The negative photoresist used in this work is AZ nLOF2020 for patterning of microwire arrays. For simplicity, the procedure of photolithography as used in the fabrication of microwires can be described as follows:

Firstly, a thin layer of oxide is grown on the Si wafer by heating it to between 900 −1150 °C in steam or in a humidified oxygen stream. The silicon oxide serves as an insulator layer. Subsequently, a layer of photoresist is deposited on the substrate by spin coating. The thickness of the photoresist layer is determined empirically depending on spin-coating speed and the viscosity of the photoresist.

After spin coating, the wafer is soft-baked at a certain temperature depending on the thickness of the photoresist. In this work, the AZ nLOF2020 photoresist is soft-baked at 115 °C. The soft-bake time depends on the resist thickness. For a thin layer of AZ nLOF2020 photoresist, the soft-bake time is 90 s. After soft baking, the resist-coated wafer is transferred to the exposure system for illumination, where structures from a mask are transferred onto the resist. The chemical reaction of the resist is induced by the radiation, causing a change of the solubility property in the exposed area. After that, post-exposure baking is required to complete the chemical reaction of the resist. The post-exposure baking procedure reduces the amount of resist left behind after development. The final step is to develop the resist within the solvent and form the desired structure. Figure 2.8 shows the chip after development (a and b) and metal deposition and lift-off (c and d).

2.3.2 MICROFLUIDIC CHANNELS FOR CELL CULTURE

NEURONAL GUIDANCE AND ORIENTATION USING MICROFLUIDIC CHANNELS Microfluidic devices have been shown to be a useful tool for studying cellular behavior. Microfluidic platforms allow biologists deep in-

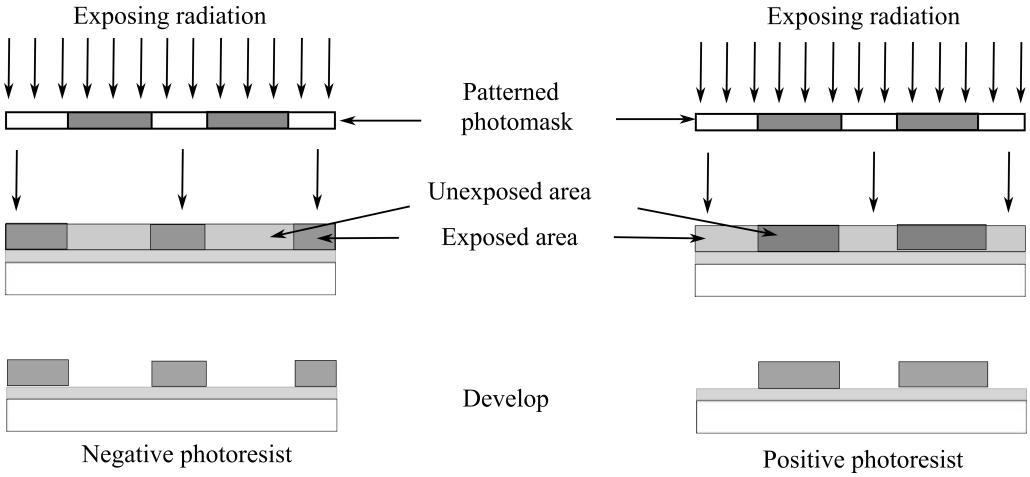

FIGURE 2.7: The schematic shows changes in characteristics of the negative and the positive photoresist after being exposed.

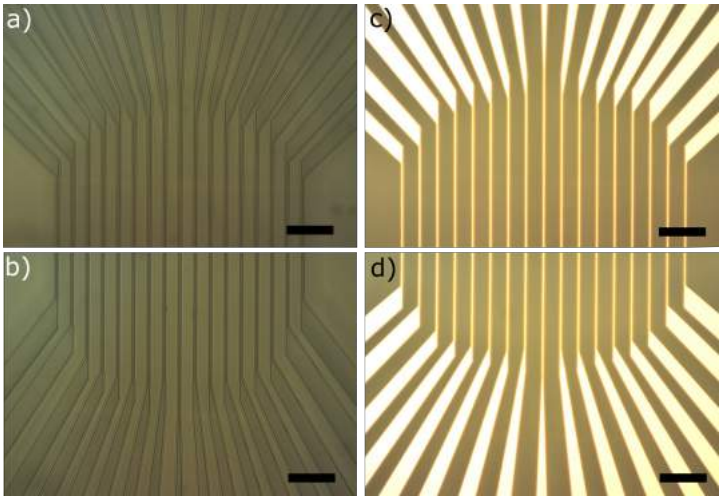

FIGURE 2.8: Structure of microwire array chips. a) and b) are the chip's surface after development. c) and d) are the chip's surface after metal deposition and lift-off. Scale bars correspond to 100 µm.

sights into cellular functionality due to their ability to precisely control the micro-environment inside living cells [16, 48–50]. There are many different microfluidic structures, which have been used depending on the purpose of the research. In this section, microfluidic structures focusing on neurite guidance and polarization are introduced to help give readers an overview of the characteristics of these devices. These microfluidic devices allow the localization of physical and chemical stimulation on neurites selected for studying neuronal regeneration and degeneration. A microchannel structure for separating neurite outgrowth from neurons was first introduced by Taylor *et al.* [51, 52]. This microfluidic structure was designed by using a physical barrier in which micron-size grooves were embedded to allow neurites to extend into these microchannels. This device included two separate cell culture chambers, a somata compartment, and an axonal compartment. Two compartments were connected by microchannels (Figure 2.9). The dimensions of the microchannels were 10 µm wide and 3 µm high. The small structure prevented neuronal cell bodies (somata) from entering microchannels. Furthermore, this structure allows quantifying the properties of neuron outgrowth such as growth length, growth rate, and retraction rate due to straight growth along the microchannels of neurites [53].

Another microfluidic structure for neurites orientation was introduced by Peyrin *et al.* [54]. This is an asymmetrical structure with wide inlets and narrow outlets. This structure allows a selective filter in a single direction for neurites and orientation of axons. These microchannels thereby act as a "diode" for axonal projection. Using this funnel structure, with 15 µm inlet and 3 µm outlet as shown in Figure 2.10, the number of neurites seen reaching the opposite chamber from the chamber outlet is drastically reduced. This microfluidic platform performs as a directional model for neural networks which could not be obtained before [54].

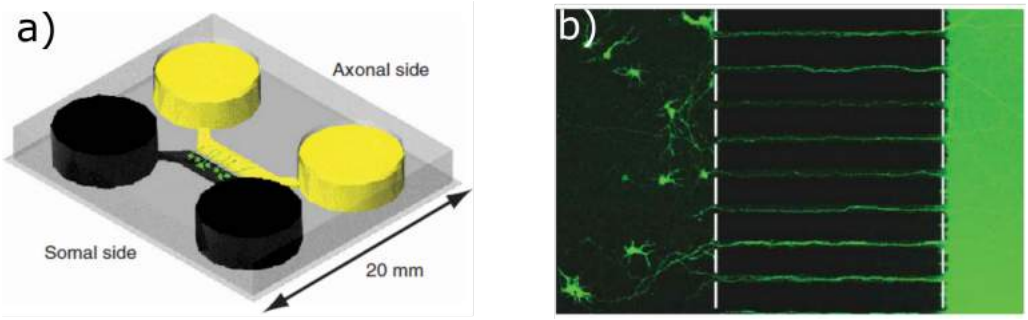

FIGURE 2.9: The microfluidic platform for neuron culture, images reprinted with permission from [52]. a) The culture chambers contain two compartments, somal side (black) and axonal side (yellow), connected by microchannels in between. b) The neurites extended from the somal side into the axonal side through the microchannels.

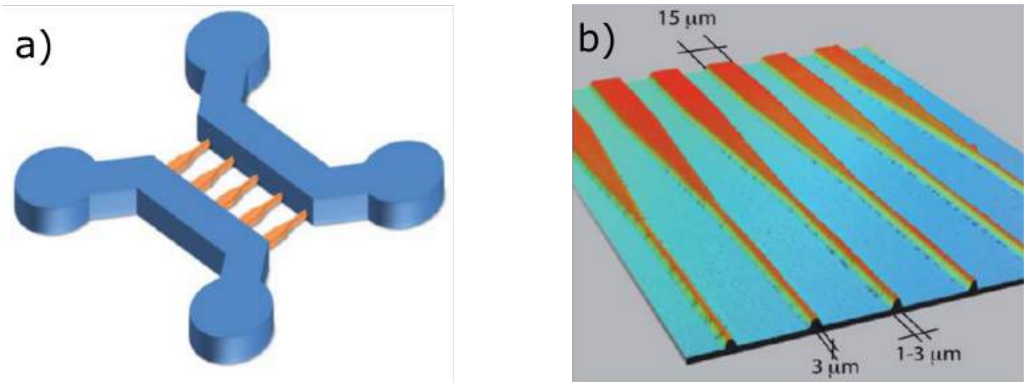

FIGURE 2.10: The microfluidic platform for neurite polarization and orientation, images reprinted with permission from [54]. a) The culture chambers contain two compartments connected by the asymmetrical microchannels in between. b) The dimension of the microchannels' outlet and inlet.

2.3.3 FABRICATION TECHNOLOGIES FOR MICROFLUIDIC CHANNELS

SOFT LITHOGRAPHY The soft lithographic method is a fabrication technique which uses elastomeric materials such as polymers and gels. The most common polymer used in this technique is polydimethylsiloxane (PDMS) due to its useful properties, including low cost, biocompatibillity and optical transparency. The PDMS prepolymer consists of two components, a polymer base and a curing agent. A typical PDMS mixture ratio between polymer and curing agent is 10:1. For simplicity, a process of soft lithography is shown in Figure 2.12. Firstly, a master mold is fabricated by photo-patterning SU-8 microchannel structures on a silicon wafer. SU-8 is a negative photoresist and commonly used to fabricate high-aspect ratio three dimensional patterns. In order to form a PDMS microchannel, the PDMS prepolymer is poured onto the master mold and then cured by heat. After curing, the PDMS microchannel is removed from the master mold. Then, a biopsy puncher is used to punch holes through the PDMS to create chambers for cell culture. To bond the PDMS onto a glass substrate or a chip's surface, oxygen plasma is used to treat the PDMS and the substrate's surface. The treatment of oxygen plasma on PDMS forms polar functional groups which are mainly silanol groups (SiOH) [55] (see Figure 2.11a). This changes the surface of PDMS from hydrophobic to hydrophilic. By this way, the covalent bonds are formed between the treated PDMS and the glass substrate when they are brought together. Another method for bonding PDMS onto the polyimide chip's surface is silanization. This method aims to form a covalent -Si-O-Si- bond between the PDMS and the polyimide chip's surface (see Figure 2.11b).

Although the PDMS has been commonly used for microfluidic devices, its sponge-like structure tends to absorb molecules from solution [56]. The high porousness of PDMS causes the undesirable drying of the sample, leading to changing osmolarity. Because of these problems, the microfluidic channel made from PDMS needs to be improved by using another material. The fabrication of SU-8 microfluidic channels using sac-

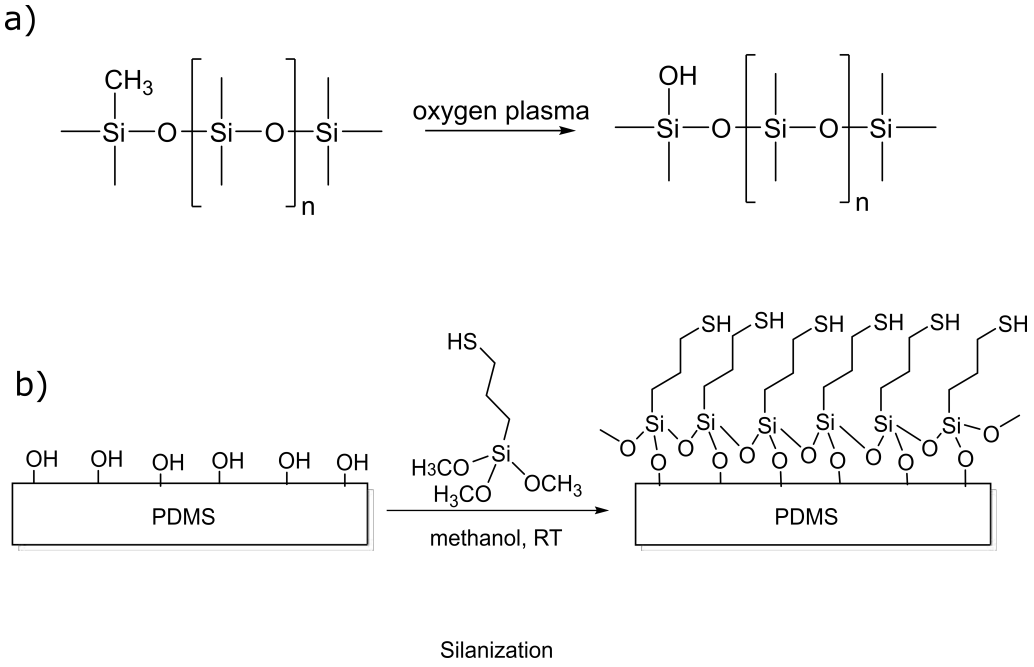

FIGURE 2.11: a) The chemical reaction of oxygen plasma and b) silanization.

rificial layer process is probably a promising substitute method. This method will be described below.

MICROCHANNEL FABRICATION TECHNIQUE This technique concerns deposition, photolithographic patterning, and selective etching of thin films to form microchannel structures. A process of microchannel fabrication is described in Figure 2.13. A sacrificial layer is deposited and patterned using photolithographic methods. The shape and size of microchannels are defined by the structure of the sacrificial layer. Then a mechanical layer is deposited and patterned onto the sacrificial layer. The final step is sacrificial etching, in which the first layer is dissolved by the etchant. Many materials such as metal, polymer, and silicon dioxide have been used to produce the sacrificial layer. The sacrificial thin-film materials are fabricated using different processing methods such as physical vapor (PVD) and chemical vapor (CVD) deposition techniques. PVD is a process employed to deposit thin films on a substrate in low pressure environments (usually in a vacuum chamber). The most common PVD processes are

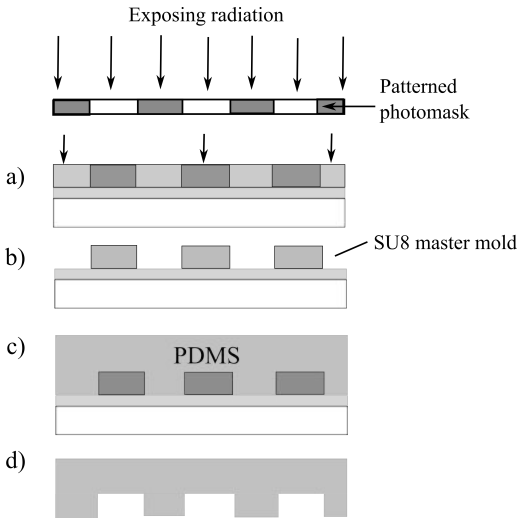

FIGURE 2.12: The soft lithography process. a) and b) are the lithophotography processes used to produce a SU-8 master mold, c) Pouring PDMS onto the master mold d) Releasing PDMS after curing.

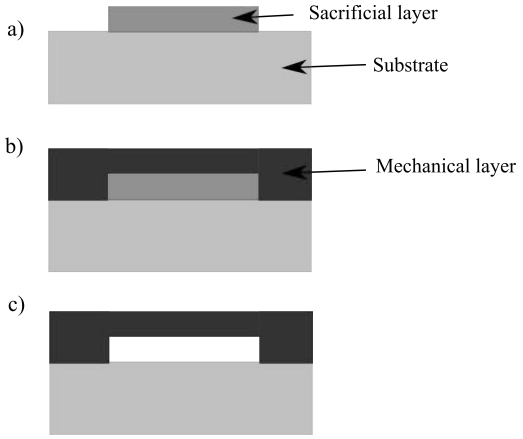

FIGURE 2.13: The microchannel fabrication process using a sacrificial layer. a) The sacrificial layer is deposited and patterned onto the substrate, b) The mechanical layer is deposited and patterned onto the sacrificial layer c) The sacrificial layer is etched.

evaporation and sputtering. Evaporation consists of two basic processes, the vaporization of source materials and their condensation onto the surface of the substrate [57]. Sputtering is a process of ejecting atoms from a target material by means of energetic particles [57]. The PVD technique is mostly used to deposit metals [57]. CVD is a process using diffusive-convective mass transfer to deposit material [57]. The advantage of this technique is that it is possible to deposit a wide variety of materials. However, many gases used in the CVD process are toxic and this technique is relatively expensive.

A different sacrificial layer material used for fabrication of microchannel is a photoresist. It is an alternative choice which can reduce number of steps necessary for patterning [58]. Photoresist is deposited on the substrate using the photolithography process. This process can be used to fabricate a high aspect ratio structure by patterning a thick layer of photoresist.

2.4 HEAT STIMULATION

The previous sections discussed fundamental aspects of cell biology and fabrication techniques for producing microwire array chips and microchannels. The microwire array chips are used to stimulate cellular networks via resistive heating. Therefore, the following section gives the reader fundamental theories about resistive heating and heat transfer.

2.4.1 RESISTIVE HEATING

Resistive heating is also known as Joule heating, which is a process whereby electrical energy is converted into heat by passing an electric current through a conductor. In particular, when an electric field is applied to a conductor, it causes a force on the individual charge carriers. This force accelerates free electrons in the conductor moving in a direction opposite to that of the electric field. The acceleration caused by the electric field will be lost quickly due to collisions between the charge carriers and atoms, as well as between charge carriers. These collisions cause

the kinetic energy of the charge carriers to convert to vibrational energy of the atoms in the lattice. This results in an increase in the temperature of the conductor [59]. Figure 2.14 shows a simple circuit consisting of a

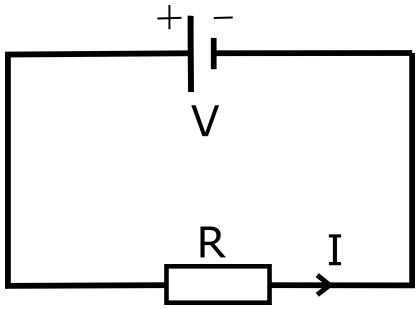

FIGURE 2.14: A circuit consisting of a resistor of resistance R and a battery having a potential difference V. The movement of charges is measured as a current I.

battery and a resistor. We assume that a quantity of positive charge is moving counterclockwise around the circuit through the battery and the resistor. When the charge passes through the resistor, it loses a part of its energy as it collides with atoms in the resistor, thereby producing an internal energy. The rate at which the charge loses energy is equal to the power P delivered to the resistor:

$$P = IV, \tag{2.4}$$

where I is the current in the circuit, V is the potential difference of the battery. According to Ohm's law, we have the potential difference $V = IR$, in which R is the electrical resistance of the wire. The resistance of the wire is defined following the equation:

$$R = \rho \frac{l}{A}, \tag{2.5}$$

Where ρ is the electrical resistivity of material, l is the length of the wire, and A is the cross-sectional area of the wire.

If we substitute the potential difference $V = IR$ into the equation 2.4, we can express the power delivered to the resistor in other forms:

$$P = I^2R = \frac{V^2}{R}. \tag{2.6}$$

2.4.2 HEAT TRANSFER

In this work, resistive heating of microwires is used as a microscopic heat source for localized heat stimulation of cellular networks. In order to evaluate the dissipation of thermal energy depending on the power supplied, finite element simulations and the experimental method of fluorescence lifetime imaging (FLIM) are used to identify the local temperature. The following section will introduce fundamental theories of heat transfer across the system.

In general, there are three different types of heat transfer: conduction, convection and radiation, as shown in Figure 2.15. Conduction is the transfer of heat across the medium when a temperature gradient exists. Convection is a process of heat transfer which occurs between a surface and a moving fluid when they are at different temperatures. Radiation describes heat transfer in the form of electromagnetic waves [60].

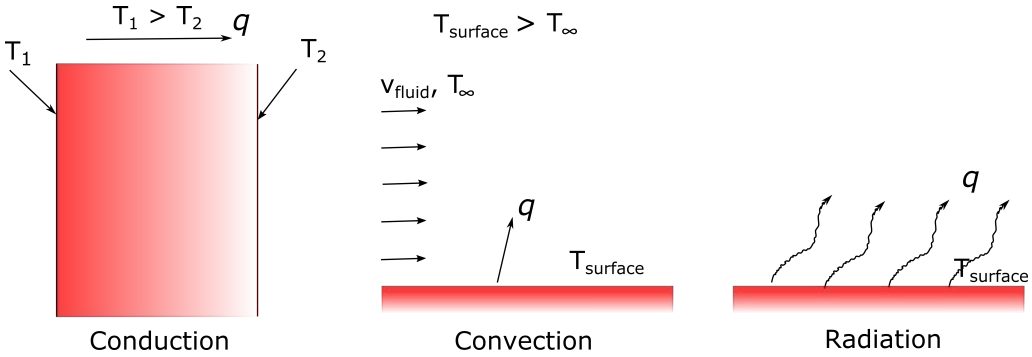

FIGURE 2.15: Three types of heat transfer: heat conduction, convection and radiation.

In this section, the three main heat transfer mechanisms will be reviewed and a heat transfer equation will be presented.

CONDUCTION Conduction is the microscopic transport of energy from higher energy particles to less energetic particles, due to particles moving inside the substance and colliding with each other. Considering a metal substance for which a temperature gradient exists, particles close to the higher temperature area vibrate with higher energy. These particles collide with their neighboring particles and transfer some of their energy into these collisions, which in turn means that the energy of particles far from the heated area increases. As a result, the process of heat transfer by conduction in the presence of a temperature gradient occurs in the direction of decreasing temperature [60].

The rate of heat conduction depends on the properties of the substance being heated [59]. Metals are good thermal conductors because there are a large number of electrons that can move freely through the solid structure. In contrast, glass and polymer are poor thermal conductors. In order to evaluate the ability of substances to conduct heat, thermal conductivity is introduced. Substances that have high thermal conductivity are good thermal conductors, whereas substances that have low thermal conductivity are used as thermal insulation.

For a material to conduct heat, the heat flux goes from a higher temperature to a lower temperature. In order to compute the amount of heat being transferred per unit time, Fourier's law of heat conduction was proposed. For the heat transfer in a one-dimensional system, having temperature distribution $T(x)$, Fourier's equation is expressed as follows:

$$q_x = -k\frac{dT}{dx}, \tag{2.7}$$

where q_x is the heat flux ($\mathrm{W/m^2}$), which is the heat transfer rate in the x-direction, k is the thermal conductivity of a substance ($\mathrm{W\,m^{-1}\,K^{-1}}$), and $\frac{dT}{dx}$ is the temperature gradient in x-direction. The minus sign is used because the heat is transferred in the direction of decreasing temperature.

The one dimensional formula of Fourier's law (equation 2.7) can be extended to a three dimensional equation in space:

$$\vec{q} = -k\nabla T, \tag{2.8}$$

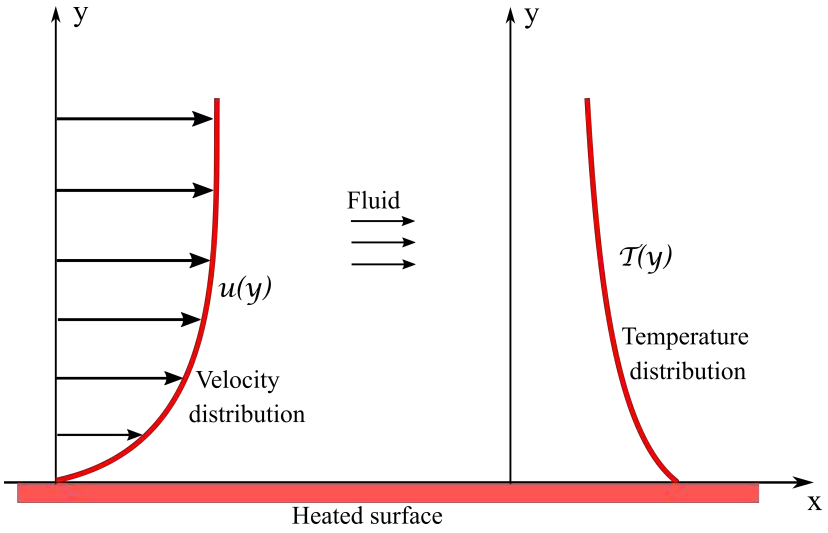

FIGURE 2.16: A convection mode of heat transfer with fluid moving over a heated surface.

From the equation 2.8, the heat flux is written as a quantity that has a specified direction and a specified magnitude. Once the set of boundary conditions, the temperature gradients, materials and heat conductivity are known, the heat flux can be evaluated from this equation.

CONVECTION The convection heat transfer is comprised of two mechanisms: heat is transferred by random molecular movement (diffusion) and the fluid movement. The motion of the fluid is associated with the moving of a large number of molecules, which contributes to heat transfer [60]. In this part, we present the heat transfer in the presence of a temperature gradient between a heated surface and a moving fluid. Consider a flow of fluid over the heated surface as shown in Figure 2.16. The velocity of the fluid varies from u_s at the fluid-surface interface to a finite value at the surface of fluid. If the temperature on a surface is $T_s > T_\infty$, T_∞ is the temperature at the surface of the fluid, and the convection heat transfer will occur from the heated surface to the surface of the flow.

According to the nature of flow, convective heat transfer is classified as forced convection or natural convection. Forced convection occurs when the flow is generated by external objects such as a pump or atmospheric

TABLE 2.2: Typical values of the convective heat transfer coefficient (adapted from [60]).

Process	h (W/m^2 K)
Free convection	
Gas	2-25
Liquids	50-1000
Forced convection	
Gas	25-250
Liquids	100-20000

winds. Natural convection is induced by differences in density because of temperature variations in the fluid.

The rate of convective heat transfer between a surface and a fluid can be calculated from Newton's law of cooling as follows:

$$q = h(T_s - T_\infty), \tag{2.9}$$

where q is the convective heat flux (W/m^2), T_s and T_∞ are the temperatures of the heated surface and the surface of the fluid respectively. h is the convective heat transfer coefficient (W/m^2 K). This coefficient depends on conditions in the boundary layer, which are influenced by surface geometry, the nature of the fluid motion, and an assortment of fluid thermodynamic and transport properties. The typical values of the convective heat transfer coefficient are given in Table 2.2 [60].

In this work, the fluid on the chip's surface is stilled. Therefore, the contribution of convective heat transfer is the natural convection.

RADIATION Radiation is the energy emitted by the thermal vibration of molecules. The energy of radiation is transferred in the form of electromagnetic waves. Thermal radiation is emitted by the surface area, and depends on the thermal energy of matter bounded by the surface.

However, in biological systems, thermal conduction and convection are the two dominant factors, which are caused by mass transport in the capillary system.

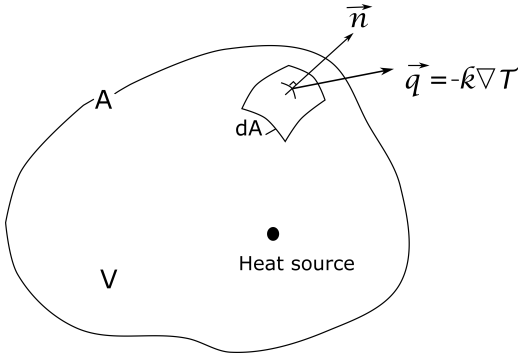

FIGURE 2.17: A schematic describes heat transfer in a control volume.

HEAT TRANSFER EQUATION Heat dissipation in the system is calculated based on relevant heat transfer equations. These equations define the relation of the heat generated by the electrical current in a microwire, the temperature distribution within the wire, and the wire's surroundings. The analysis of heat transfer is governed by the first law of thermodynamics. For a closed system, this conservation law can be written as follows:

$$E_{\text{int}} = E_{\text{ch}} + E_{\text{out}}, \tag{2.10}$$

where E_{int} represents the heat generated internally by Joule heating, E_{ch} represents the rate of change of internal heat energy, and E_{out} represents the heat energy coming out of the microwire by conduction.

A volumetric heat release distributed through the volume is q_{v} (W/m^3). This is the result of resistive heating. Thus the heat generated within the volume V is:

$$E_{\text{int}} = \int_V q_{\text{v}} \text{d}V. \tag{2.11}$$

The rate of change of internal heat energy is defined by

$$E_{\text{ch}} = \int_V \rho c \frac{\partial T}{\partial t} \text{d}V, \tag{2.12}$$

where ρ is density (kg/m^3), and c is specific heat capacity ($\text{J}\,\text{kg}^{-1}\,\text{K}^{-1}$). The outflow of heat energy E_{out} is proportional to the surface area. The surface and an element of the surface are defined as A and dA, respectively (as shown in Figure 2.17). There are two vectors shown on dA: one

is the unit normal vector $\vec{n}$, and another one is the heat flux vector, $\vec{q}$, at the point on the surface. The heat energy conducted out of area $\mathrm{d}A$ can be written as following:

$$E_{\text{out}} = \int_A (\vec{q})(\vec{n}\mathrm{d}A), \tag{2.13}$$

substitute the heat flux $\vec{q}$ from equation 2.8 to the equation 2.13, the heat energy transferred out of area $\mathrm{d}A$ can be written as follows:

$$E_{\text{out}} = \int_A (-k\nabla T)(\vec{n}\mathrm{d}A). \tag{2.14}$$

Applying Gauss's theorem, E_{out} can be written as follows:

$$E_{\text{out}} = \int_A (-k\nabla T)(\vec{n}\mathrm{d}A) = \int_V \nabla(-k\nabla T)\mathrm{d}V, \tag{2.15}$$

substitute E_{int}, E_{out}, and E_{ch} to equation 2.10, the equation 2.10 can be written as follows:

$$\int_V q_{\text{v}}\mathrm{d}V = \int_V \rho c\frac{\partial T}{\partial t}\mathrm{d}V + \int_V \nabla(-k\nabla T)\mathrm{d}V. \tag{2.16}$$

Because the volume V is arbitrary, the integrand can be taken out, so the equation 2.16 can be written:

$$q_{\text{v}} = \rho c\frac{\partial T}{\partial t} + \nabla(-k\nabla T). \tag{2.17}$$

Finally, a general form of the heat transfer equation is obtained as follows:

$$\nabla(k\nabla T) + q_{\text{v}} = \rho c\frac{\partial T}{\partial t}. \tag{2.18}$$

Using the equation 2.18 with the known parameters of the microwires, such as the dimensions of the wire, the materials of the wire, and the boundary conditions, the temperature distribution of the wire can be solved. However, the solution is only feasible for simple geometries and symmetric boundary conditions. In our work, the numerical method us-

ing COMSOL Multiphysics has been applied to investigate the heat transfer on microwire arrays.

2.5 OPTICAL DETECTION

2.5.1 CALCIUM IMAGING

As described in the section 2.1.3, the intracellular calcium concentration plays an important role in regulating the function of cardiomyocytes. Therefore, the observation of changes in intracellular calcium allows us to draw conclusions about the functional state of the cells. In order to visualize the calcium signal, calcium imaging, a remote fluorescence-based calcium detection technique, was used in this work.

This approach is performed by staining living cells with a fluorescent dye. In order to record the intensity changes of the fluorescent dye, a fast and sensitive camera is coupled with a microscope setup and a standard fluorescent filter set. The basic principles of the calcium imaging technique are described in the following, referring to Takahashi *et al.* [61]. When the fluorescent dye is loaded into the cell, it binds to the intracellular calcium. The binding to the Ca^{2+} causes the dye to change its fluorescent properties (i.e. intensity or wavelength).

Most fluorescent dyes are impermeable to the cell membrane. In order to load the dyes into the cells, there are a number of techniques that can be used such as microinjection, macroinjection, and ester loading [61]. In the microinjection technique, the calcium indicators can be diluted in a cytosol-like solution; then, a glass micropipette is used to inject the indicator into the cells. However, this method is difficult to perform with a large number of cells (the best microinjectors can only load approximately 100 cells/h). Conversely, macroinjection methods enable us to load indicators into many cells at once. The disadvantage of the micro and macroinjection method is that it is invasive and requires specialized equipments and practice.

In this thesis, the Fluo-4, a fluorescent calcium sensing dye, has been used to probe the changing concentration of intracellular calcium. For loading the Fluo-4 dye into the cells, the carboxylic acids group is modified by acetoxymethyl (AM) ester groups, resulting in an uncharged molecule which can cross the cell membrane. After permeating into the cell, esterases inside the cell cleave off the AM ester groups. This ensures a high concentration of the dye inside the cell.

Another important characteristic influencing the considerations in choosing an indicator is the dissociation constant (K_d), which is the calcium binding affinity of the indicator. The calcium sensitivity is achieved, most reliably, in below and near K_d [61]. For the high-affinity calcium indicators, they can yield high fluorescence intensity, but they saturate at relatively low calcium concentration and they likely buffer intracellular calcium. The low-affinity dyes are used to measure the high level of calcium concentration in subcellular organelles. The rapid measurement of changes in the calcium concentration is an advantage of the low-affinity dyes because their reaction kinetics are fast enough to analyze the high temporal resolution of events.

In order to qualitatively measure the change in intracellular calcium concentration, a relative change of fluorescence signal R_f can be calculated as follows:

$$R_\mathrm{f} = \frac{F - F_\mathrm{base}}{F_\mathrm{base}} \tag{2.19}$$

where F is the measured fluorescent intensity of the calcium indicator, F_base is the intensity of the calcium indicator before stimulation. Although the precise concentration of calcium cannot be measured, this ratio can be used to approximate the intracellular calcium concentration.

The Ca^{2+} measurements in this thesis were recorded using an imaging software. The imaging was performed using a rolling average filter with a width of 4 frames and a sequential subtraction of 4 frames to achieve an increased grey-scale resolution. Because of the live processing, the Ca^{2+} imaging in this work was analyzed based on the temporal averaging of the fluorescent intensity as following:

$$F_{\text{norm}} = \frac{F - F_{\text{av}}}{F_{\text{av}}}, \tag{2.20}$$

where F_{norm} is the normalized fluorescent intensity, F_{av} is the temporal average of the fluorescence intensity, and F is the measured fluorescent intensity of the indicator.

2.5.2 FLUORESCENCE LIFETIME IMAGING (FLIM)

In order to practically measure the temperature dissipation on the microwire array, fluorescence lifetime imaging microscopy was used in this work. The following is intended to give the reader a brief overview about the fundamental theorem of this measurement technique.

FLIM measurement is the method used to evaluate temperature based on the lifetime of the fluorescent indicator when it is excited by short laser pulses (i.e. much shorter than the lifetime of the fluorophore). When a molecule absorbs a photon, it gains energy to jump to an excited state. Subsequently, the molecule stays in this state for a while and then returns to its ground state by emitting a photon. By using fast detectors, the arrival times or decay times of photons are recorded with respect to the laser pulses and the position of the laser beam [62]. The recorded data has the information about the spatial distribution, x, y and the fluorescent decay time. The result is presenting in an array in which each measured point contains the fluorescent decay time. The fluorescent decay function [63] is an exponential function given as:

$$I(t) = I_0 \exp(-\frac{t}{\tau}), \tag{2.21}$$

where $I(t)$ is the fluorescent intensity at time t, I_0 is the fluorescent intensity immediately after the pulse, and τ is the fluorescent lifetime. From equation 2.21 the lifetime can be determined. The dependence of temperature on the lifetime of fluorescent dye is calibrated based on a known set of calibration values. The values are calculated using a curve fitting algorithm [64]. The temperature can be thereby deduced from the lifetime measurement. The FLIM measurement has been used commonly as the

noninvasive method to assess the temperature since it does not depend on the concentration and absorption of the fluorescent indicator. However, the limit of the FLIM method is that the properties of fluorescent indicators could be modified responding to change in the environment such as pH changes. Furthermore, the quenching effects (decrease in the fluorescent intensity) could also be observed when imaging at a few micrometer distance from the sample.

In this work, the temperature measured from FLIM method is compared with the numerical method to have a reliable temperature distribution on the microwire.

CHAPTER 3

HEAT STIMULATION FOR MODULATING SIGNAL PROPAGATION IN HL-1 CELL NETWORKS

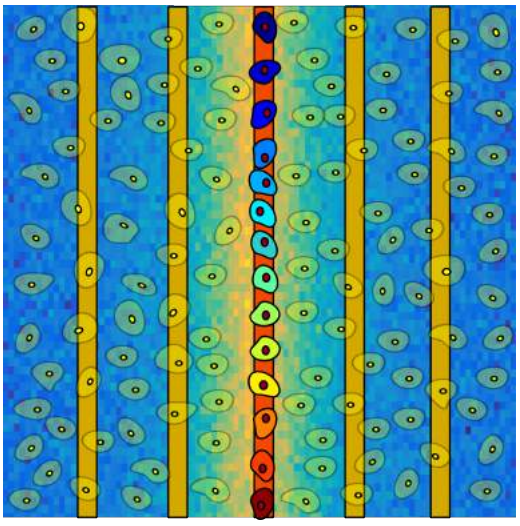

This chapter was reproduced from the unpublished work "K.M. Dang, P. Rinklin, D. Afanasenkau, G. Westmeyer, T. Schürholze, S. Wiegand and B. Wolfrum, Chip-based heat stimulation for modulating signal propagation in HL-1 cell networks." *in submission*.

3.1 PREAMBLE

The present work aims to study the influence of localized temperature gradients on signal propagation in cardiac cell networks. Localized temperature gradients are generated by resistive heating via microwire arrays on a chip surface, which serves as a substrate for growing a confluent cell network. In this work, the velocity of the propagating Ca^{2+} wave in the network is locally increased upon heat stimulation. Furthermore, a relocation of the pacemaker cell and a deformation of the Ca^{2+} wavefront caused by an increase of the local temperature will be investigated in this chapter.

3.2 INTRODUCTION

The healthy body temperature of endotherms falls within a rather narrow window. Lowering or increasing the temperature may cause metabolic and functional problems in cardiac activity [65]. Cardiac muscle contraction depends on intracellular Ca^{2+} dynamics [66]. The Ca^{2+} release from the sarcoplasmic reticulum increases the cytosolic Ca^{2+} concentration and triggers a propagating Ca^{2+} transient. When the Ca^{2+} concentration is high enough, contraction of the cardiac muscle cell occurs. Once the intracellular Ca^{2+} concentration decreases again, the cardiac muscle cell relaxes [67, 68]. Cardiac Ca^{2+} signaling relies on a few critical molecular players like ryanodine receptors, voltage-gated Ca^{2+} channels, and Ca^{2+} pumps [69], which are affected by temperature changes [70–72]. However, assessing the effects of local temperature inhomogeneities at the cellular level is still difficult [73, 74]. So far, most investigations on the effect of temperature on Ca^{2+} transients in cardiac myocytes employ ambient temperature control [75–77]. This way, a global response is observed potentially masking a possible influence of local temperature effects. Heating cells in only a localized area can be achieved using a focused infrared laser [78–80]. This approach has been demonstrated for the excitation of action potentials in muscle and nerve cells [81, 82]. How-

ever, it requires the alignment of microscope setups that are difficult to parallelize and cannot be easily applied in long-term or high-throughput studies [83]. Alternatively, localized heating using electromagnetically excited nanoparticles has been applied in several reports [84–86]. However, heat dissipation for a large number of nanoparticles dispersed in a macroscopic region of tissue produces a global rise in temperature [87]. Moreover, the toxicity of nanoparticles usually imposes a high risk of cell damage [88].

Recently, microsystems have created new opportunities for applying spatially and temporally controlled stimuli and recording cellular activity [19, 89, 90]. Examples demonstrate the application of microchip devices for electrical stimulation [67, 91–93], parallelized single-vesicle release measurement [94], or studies of signal propagation in cardiac myocyte networks [95, 96]. The microwire array chips has been introduced to inflict thermal lesions in cell cultures for separating network connectivity [97]. In this work, the microwire arrays are used to induce localized hyperthermia to modulate signal propagation in cardiomyocyte networks. The heating of individual microwires allows to generate highly localized temperature gradients. We apply this method to study dynamic changes in intracellular Ca^{2+} signals in response to local heat stimuli in cardiomyocyte-like HL-1 cells. The HL-1 cell line used in this experiment was derived from mouse cardiomyocyte tumor [39]. The HL-1 cardiac muscle cells show spontaneous action potentials and subsequent contraction after the cells reach confluency. We demonstrate that heating can lead to localized effects on Ca^{2+} signal propagation influencing the propagation speed, direction and the position of the pacemaker cell.

3.3 MATERIALS AND METHODS

3.3.1 FABRICATION OF MICROWIRE ARRAY CHIPS

I fabricated microwire array chips in the clean room of the Helmholtz Nanoelectronic Facility. The arrays consist of 17 microwires that were

structured and isolated using state-of-the-art microfabrication technology. The microwire array chip was used for applying resistive heating to induce thermal stress on cellular networks. The fabrication process is presented as follows. A thermally oxidized silicon wafer of 4 inches diameter and 500 µm thickness was used as a substrate. First, a double layer resist (LOR3B; Microchem, Newton, MA and AZ nLOF 2020; MicroChemicals, Ulm, Germany) was spin-coated onto the wafer and the microwire array structure (comprised of 17 wires with a width of 2.5 µm and the pitch of two adjacent microwires 30 µm) was patterned using standard photolithographic procedures. After exposure and development (MIF326, microresist technology, Berlin, Germany), a metal stack (10 nm Ti/300 nm Au/10 nm Ti) was deposited by electron-beam vapor deposition. The titanium layers served to facilitate adhesion of gold structures to the substrate and the following passivation layer. After structuring the microwire array, a polyimide layer (PI2545, HD Microsystems GmbH, Germany) was spin-coated (6000 rpm, 30 s) to passivate the chip for cell-culture conditions. For electrical connection of the chip to the power supply system, a second photolithography was performed to locally remove the passivation layer on the outer contact pads.

3.3.2 CULTURE OF HL-1 CELLS ON THE MICROWIRE ARRAY CHIP

HL-1 cells were cultured in T25 flasks at 37 °C and 5 % CO_2 in Claycomb Medium (51800C, Sigma) supplemented with FBS (10 %, ThermoFischer Scientific), penicillin-streptomycin (100 µg mL^{-1}, ThermoFischer Scientific), norepinephrine (0.1 mmol, Sigma) and L-glutamine (2 mmol, ThermoFischer Scientific) in a humidified incubator. After the cells reached confluency and started beating, they were cultured on the microwire chips. Before plating the cells, the microwire chips were sterilized with UV light for 1 h. The chips' surface was then incubated in a mixture of fibronectin (5 µg mL^{-1}, Sigma) and gelatin (0.2 mg mL^{-1}, Sigma) for approximately 60 min. Then 500 µL of cell suspension was seeded on the chips and incubated under normal conditions (37 °C, 5 % CO_2).

3.3.3 THERMAL STIMULATION AND CA^{2+} IMAGING

The power supply was operated by a custom LabView software [98]. Thermal stimulation was applied to the cells in normal growth medium. The electrical power was applied to one middle microwire for 30 s (P = 0.7 W). The resting time between each stimulation pulse was 1 min for recovery of the cells. In order to observe the dependence of cell activity on local heating, HL-1 cells were stained with a Ca^{2+} sensitive dye (4 µmol Fluo-4 AM, Thermofisher) for 15-30 min. The medium was then exchanged and the sample was transferred to the measurement setup. While performing thermal stimulation, the Ca^{2+} fluorescence signal was recorded via a high speed and low light emCCD camera (Hamamatsu C9100-13). To assess a possible influence of localize heating on the Ca^{2+} signal, the analysis of the signal propagation was based on fluorescence indicator dye (Fluo-4). It is known that the dissociation constant of Fluo-4 decreases within increasing temperature [99]. This effect may change the intensity and the waveform of the fluorescence signal. To minimize these effects, we evaluated the Ca^{2+} signal relative to the basal fluorescence. In addition, the signal propagation was measured based on the temporal correlation of the signals. Thus, the changing properties of the indicator with increasing temperature should be negligible in these experiments.

3.3.4 CROSS-CORRELATION ANALYSIS

In order to determine the activity in the Ca^{2+} imaging, the cross-correlation analysis was performed as follows: the images were down-scaled to a size of 32 x 32 pixels for the purpose of processing speed. The intensity of the resulting pixels was normalized by calculating the normalized fluorescent intensity (see the equation 2.20). The active pixels were discriminated from inactive pixels by their root-mean-square (RMS) intensity changes. To this end, the RMS of each pixel was calculated and the minimum RMS value plus half of the standard deviation of all RMS values were used as a threshold. For the cross-correlation analysis, the intensity traces of all pixels were smoothed using a Gaussian filter with

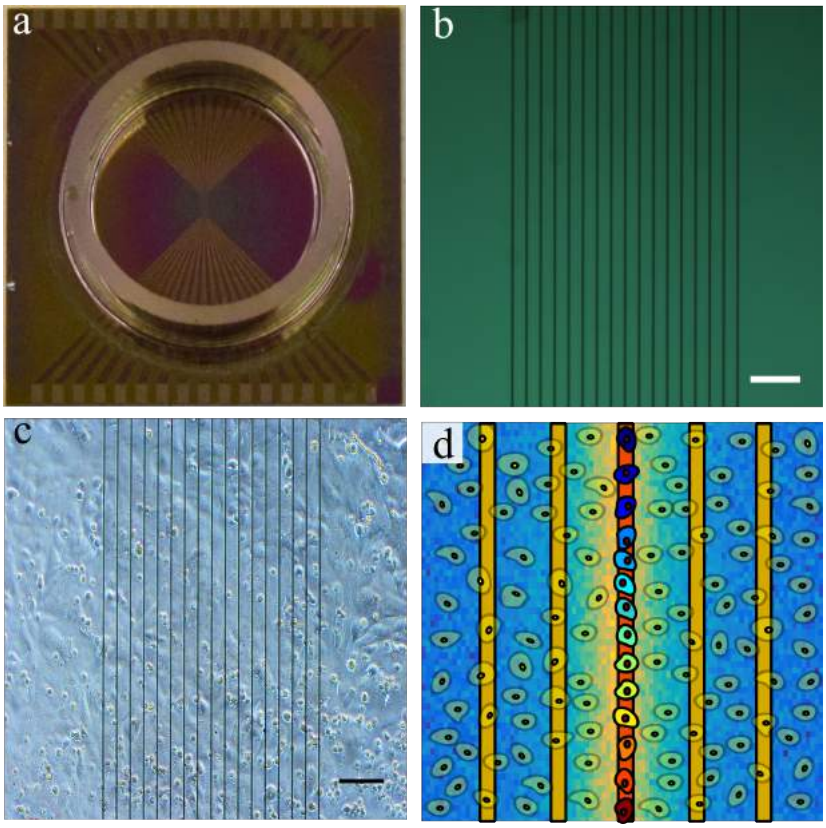

FIGURE 3.1: Microwire arrays for inducing localized thermal stimulation. a) A photograph of an encapsulated microwire array chip (chip dimension: 24 mm x 24 mm. b) A photomicrograph of the actual microwire array consisting of 17 parallel microwires. c) An optical image of HL-1 cells cultured on the chips surface. d) A schematic of a localized thermal stimulation experiment. Passing a current through a wire results in increasing the Ca^{2+} signal's speed in the heated area. Scale bars in b and c correspond to 100 µm.

a window width of 300 ms. To determine the signals propagation, the average intensity trace of all pixels was calculated and each pixel was cross-correlated with this reference trace yielding the relative signal delay of the individual pixels. The result was plotted as a color map of delay values, which presents the temporal propagation of the calcium signals.

3.4 RESULTS AND DISCUSSIONS

HL-1 cardiomyocytes have proven to be useful for studying many aspects of cardiac biology *in vitro* [39]. In order to investigate the effect of localized heat stimulation on cardiomyocytes, a layer of HL-1 cells was grown on a microwire array and thermal stimulation was applied to induce confined heating on the cell network. Figure 3.1a and 3.1b show an exemplary microwire array chip that was used in the experiments. HL-1 cells that were plated on microwire chips formed confluent layers after 2-4 days. The cells began to spontaneously generate contractile activity (beating) approximately one day after reaching confluency. Figure 3.1c shows a confluent culture of cardiac cells growing on the microwire array. A schematic of a thermal stimulation experiment affecting a linear region in the cell network is illustrated in Figure 3.1d. To evaluate the effects of local heating on spatiotemporal Ca^{2+} dynamics, Ca^{2+} imaging and Ca^{2+} propagation analyses were performed.

3.4.1 EFFECT OF LOCALIZED HEAT STIMULATION ON CA^{2+} SIGNAL PROPAGATION

In this study, we focused on the influence of localized heat stimulation on the propagation of Ca^{2+} signals in HL-1 cell cultures using microwire arrays. Heat was generated by electrical power applied through a wire. Figure 3.2 shows the time-dependent temperature profile on top of the stimulating wire. The temperature quickly reaches steady state within approximately 100 ms after applying a power of 0.7 W (Figure 3.2a). Figure 3.2b shows the temperature profile on the surface of the chip. As expected, the temperature exhibits a sharp gradient in the vicinity of the microwire.

We evaluated the dependence of the cardiac cells activity on temperature by performing optical recordings during heat stimulation. To visualize the Ca^{2+} signal propagation in the cardiac cell network, cells were stained with a sensitive fluorescence dye (Fluo-4, AM). Ca^{2+} imaging videos of spontaneous as well as thermally stimulated activity were

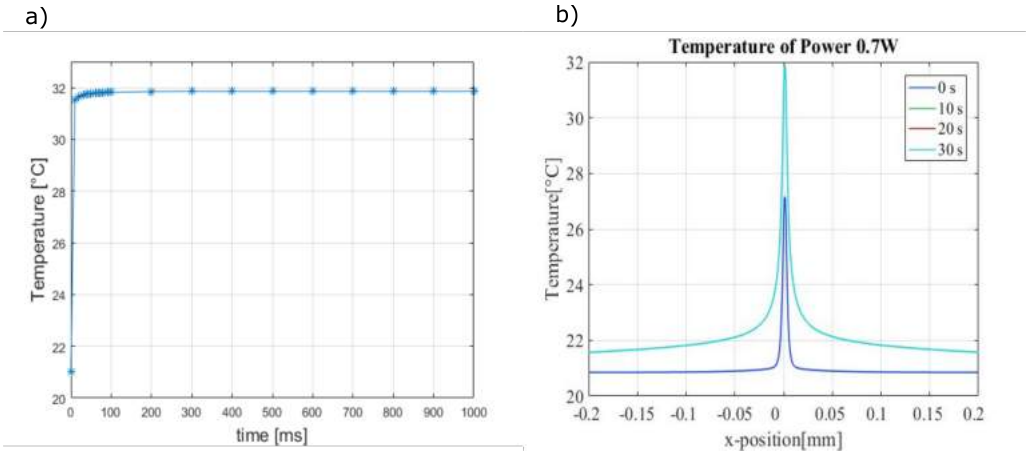

FIGURE 3.2: Comsol simulation of the temperature distribution on the surface of the chip induced by the microwire array with the power 0.7 W. a) Time-dependence of the temperature on top of the stimulating wire. The temperature quickly reaches a steady state at 32 °C within 100 ms. b) Temperature profile at the surface of the chip. An x-position of 0 mm indicates the center position of the stimulating microwire. Due to the rapid equilibration visible in a, the temperature profiles at 10, 20, and 30 s are identical.

recorded. Figure 3.3 shows representative frames of the fluorescent signal captured with and without thermal stimulation.

In order to evaluate the influence of heat on the Ca^{2+} signal propagation, the Ca^{2+} imaging video was analyzed by performing a cross-correlation of the local fluorescence intensity as can be seen for three exemplary cell culture experiments in Figure 3.4a. The colors in the images indicate the time delay between the occurrences of the Ca^{2+} signal at particular positions within the network. The signal propagates in the direction from blue to red. In these experiments, the Ca^{2+} imaging videos were recorded for 1 min without stimulation (left column) and 30 s with thermal stimulation (right column). As evident from Figure 3.4a, the change of Ca^{2+} wave propagation upon heat stimulation is clearly visible.

We analyzed the velocity of signal propagation by dividing the spatial extension by the difference of maximum and minimum delay values within a circular region (Figure 3.4b). Using this approach, the difference in the propagation direction of the signal was intentionally neglected. Although the absolute velocities as well as the relative changes in velocity

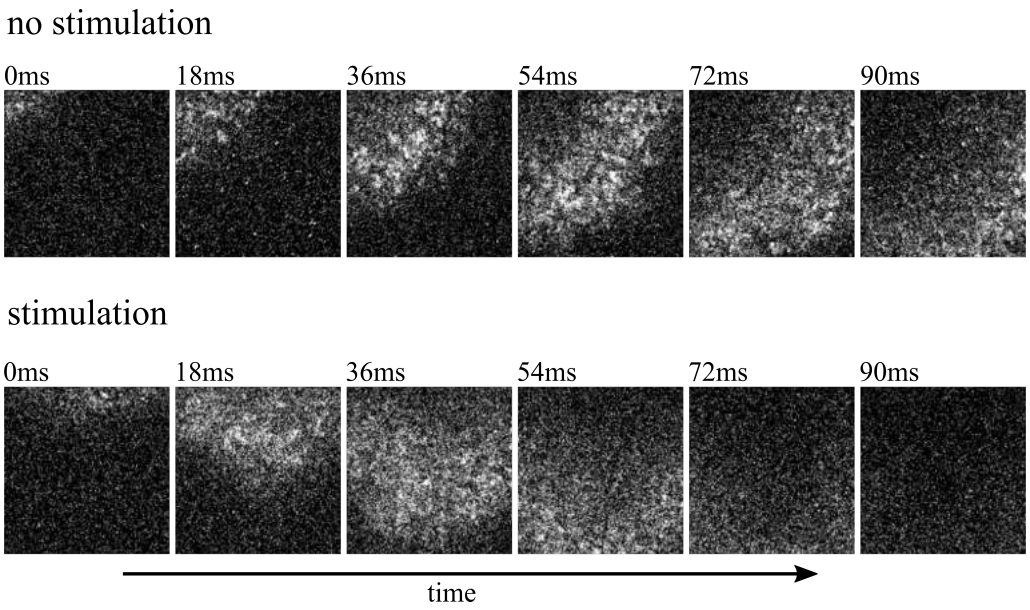

FIGURE 3.3: Exemplary frames from the Ca^{2+} imaging sequence of the sample without (top) and with (bottom) thermal stimulation. In the top row, the signal spontaneously propagates from the top left corner to the bottom right corner while, in the bottom row, the signal travels along the heated area and appears to be faster.

(Figure 3.4c) vary significantly between different cell culture experiments, we observe an increase of Ca^{2+} wave propagation velocity upon heating in approximately 87 % of all the samples investigated (n = 15).

While these results give a qualitative indication on the effect of heat stimulation on HL-1 cells, they do not provide a quantitative measure of the local propagation velocity within heated zones compared to non-heated zones. To investigate the influence of the stimulus on the local propagation velocity of the Ca^{2+} signals, we therefore analyzed correlation plots of multiple stimulation experiments shown in Figure 3.5.

In these experiments, Ca^{2+} imaging videos from the same cells were recorded during repetitive stimulation and subsequent recovery phases. The change in the Ca^{2+} propagation pattern was reversible upon successive application of thermal stimuli as can be seen by comparing the patterns in the recovery phase (Figure 3.5, left column) with the patterns during stimulation conditions (Figure 3.5, right column). The time delay of the signals in the different experiments clearly indicates that the Ca^{2+} sig-

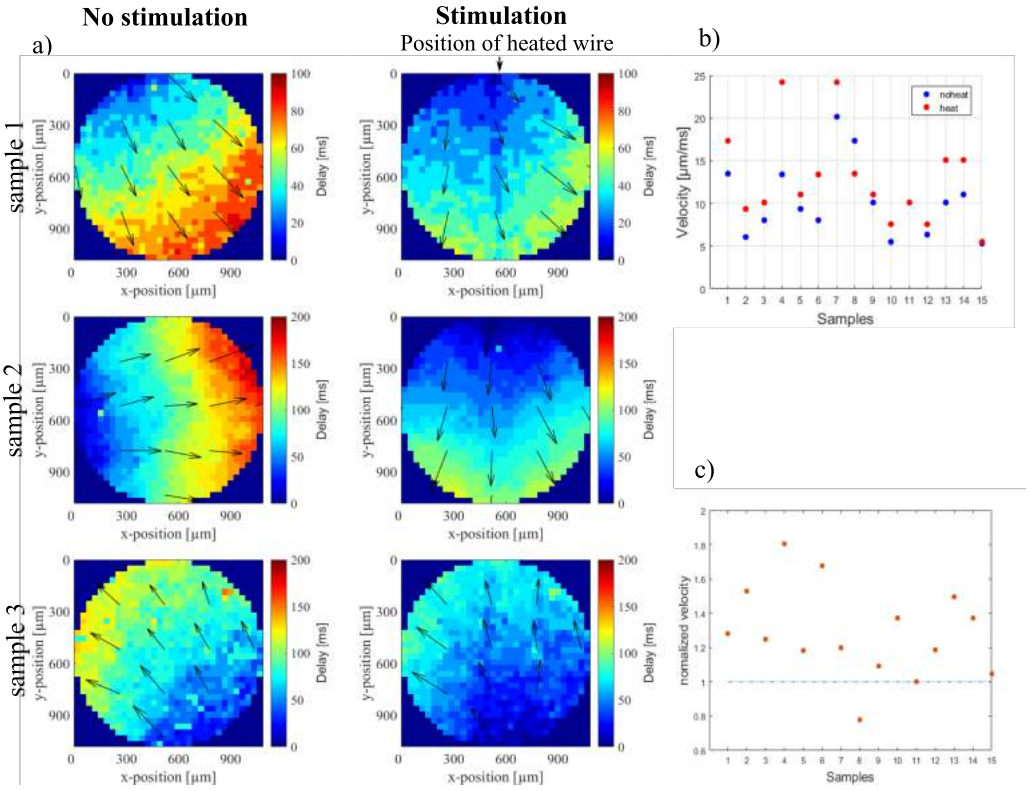

FIGURE 3.4: Signal propagation direction and velocity with and without heat stimulation. a) A comparison of signal propagation with and without heat stimulation for three independent cell culture experiments. b) Global signal velocity with and without heat stimulation of all experiments. c) The normalized velocity is calculated by the ratio of the velocity with and without heat stimulation comparing signals of the same sample. The dashed blue line indicates the threshold for equal signal velocities with and without heat stimulation.

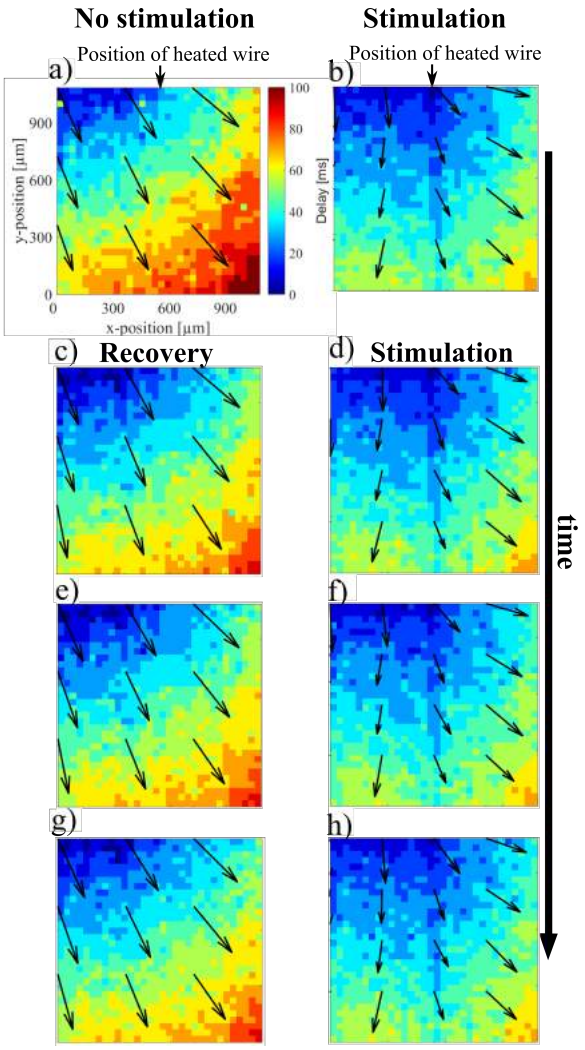

FIGURE 3.5: Reversible effect of localized heating in cardiac myocytes presented by cross-correlation analysis of Ca^{2+} imaging videos. The time delay of the propagating action potential is color-coded, referring to the color scale in (a). x- and y-axes give the dimensions of the observed sample section. A thermal stimulation was applied (b, d, f, h) on a center wire for 30 s and a recovery time of 1 min in between (c, e, g) to locally change the Ca^{2+} signal behavior of the cardiac myocyte cells. Every image represents the same position on the same sample.

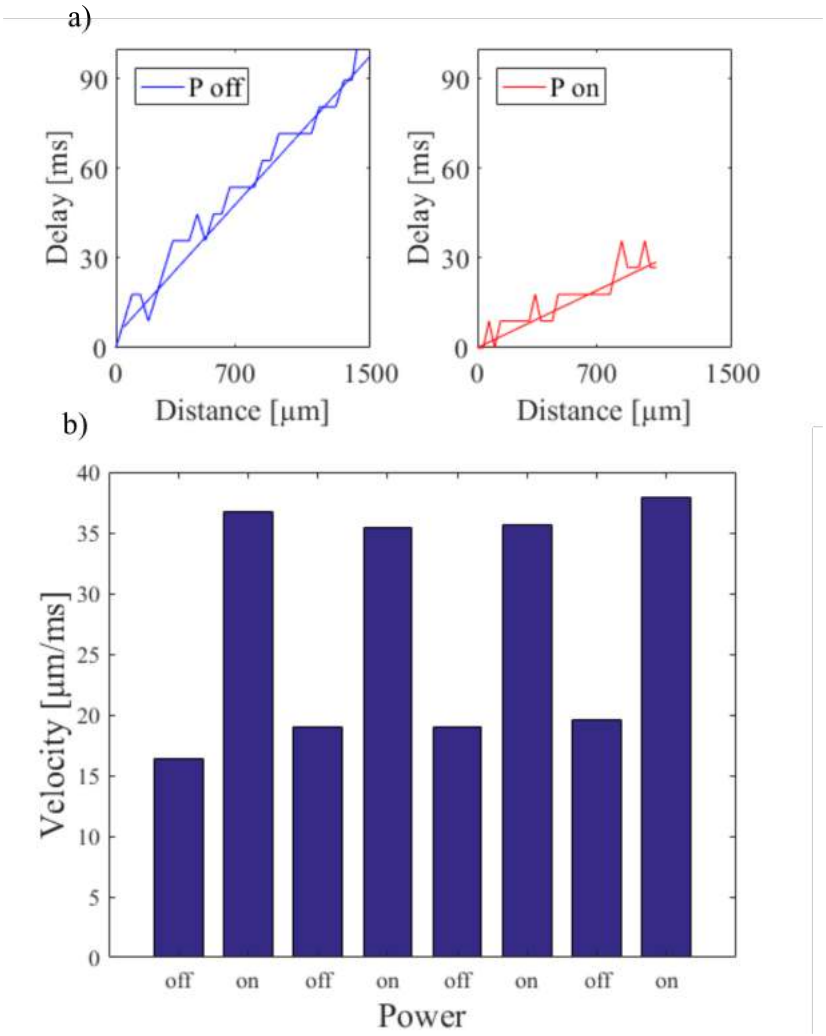

FIGURE 3.6: Plots show the speed of Ca^{2+} signal propagation with and without heat stimulation. a) Delay time versus signal progression in the corresponding frames. The red and blue traces describe signal propagation with and without heat stimulation, respectively. b) A plot of the signal velocity of the HL-1 cells shows the correlation between the power and velocity of Ca^{2+} signal when the power supplies switched on and off.

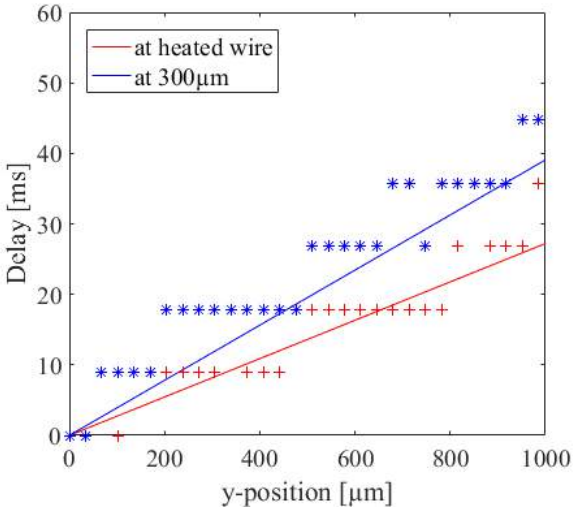

FIGURE 3.7: A plot of the signal delay (along y-axis) recorded at the heated wire (red) and at a position 300 µm away from the heated wire (blue). The data was fitted using linear function.

nal propagates faster during thermal stimulation as described above. As we were interested in the propagation velocity within high-temperature zones, we now evaluated the delay time along the propagation direction of the Ca^{2+} signal with and without heating. Figure 3.6a shows the delay time versus the distance of signal propagation, evaluated along the diagonal of the frame without thermal stimulation (blue trace) and along the y-axis in the frame with thermal activation (red trace).

The data was fitted using a linear function assuming a constant speed along the propagation direction. The inverse slope of this fit yields the propagation speed of the Ca^{2+} signal. As can be seen, the slope without thermal stimulation is steeper than the one with stimulation. Quantitative values of the propagation velocity for repetitive experiments with and without stimulation are shown in Figure 3.6b. During heat activation, the propagation speeds are higher than 35 µm ms^{-1}, whereas without heating, the propagation speeds range between 16–20 µm ms^{-1}. We attribute the slight increase of signal velocity in the recovery phase to a minor global rise in temperature due to repeated heat stimulation. Interestingly, as the propagation appears to be affected in the vicinity of the

heated region, this results in a deformation of the signal wavefront. In order to investigate the effect of local velocity changes in the heated area, we compared the propagation speed within the network along regions of different temperatures. The result is shown in Figure 3.7. The red trace indicates the Ca^{2+} signal propagation directly on the heated wire and the blue trace indicates the Ca^{2+} signal propagation at a distance of 300 µm from the heated wire. Both traces were evaluated along the vertical axis. The observed difference in propagation speed of the Ca^{2+} signals is in the range of 10 µm ms^{-1}. This demonstrates that microscopic heating can induce local variations of Ca^{2+} signal propagation speed within a connected network.

3.4.2 EFFECT OF LOCALIZED HEAT STIMULATION ON THE PACEMAKER POSITION

The observed alterations in the propagation direction of the Ca^{2+} wave upon thermal stimulations might be caused by two effects: First, the local change in propagation velocity can cause an effective shift of the propagation direction along the wire. Second, the position of the pacemaker of the cell layer can be directly affected by the thermal stimulation leading to an alteration of the propagation direction. Such a scenario is shown in Figure 3.8. In Figure 3.8a we see the propagation pattern without thermal stimulation. Here the origin of the intrinsic Ca^{2+} signal starts in the top left corner and propagates to the bottom right corner. When applying thermal stimulation, the signal origin in the field of view relocates to a position on the microwire and the propagation direction shifts along the y-direction (Fig 3.8b). A shift in signal origin towards regions of the heated area was detected in about 27 % (n = 15) of the experiments. Possibly, the mechanism of changing the pacemaker location can be explained by a local modulation of the kinetics of cellular processes affecting the beating pattern. Similar to effects observed during electrical stimulation [95, 100] a cell beating faster than the intrinsic pacemaker, can "hijack" the network and become the new pacemaker cell.

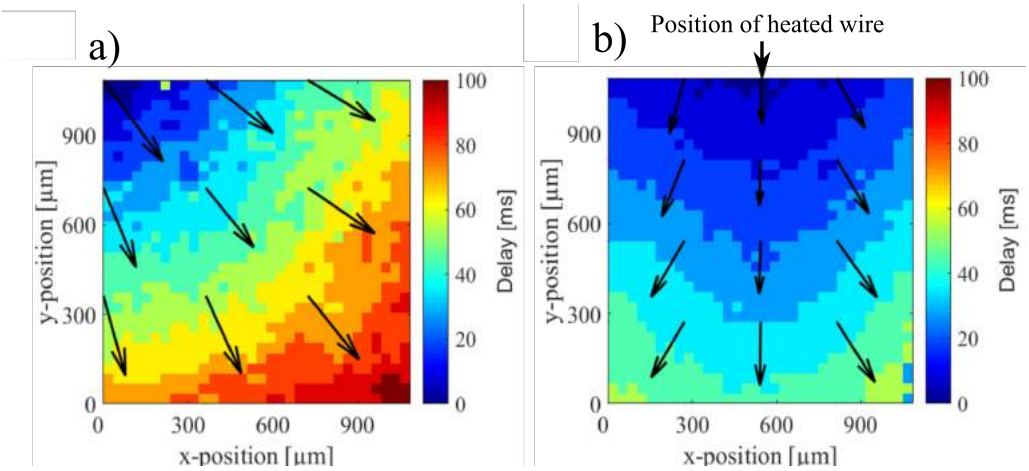

FIGURE 3.8: The effect of heat on the origin of the Ca^{2+} signals. a) The intrinsic Ca^{2+} signal propagate from the top left corner down to the bottom right corner. b) Localized thermal activation changes the propagation of the Ca^{2+} signal from the top to the bottom along the heated wire.

An increase of the beating frequency has been previously observed for global temperature stimulation [101]. To assess if, correspondingly, the Ca^{2+} signal direction is influenced by local heat activation, we compared the average angle distribution of spontaneous signal propagation directions with those during local heat stimulation. As can be seen in Figure 3.9, the Ca^{2+} signal directions tend to be shifted by the local heat stimulation clustering along the direction of the heated wire (90°). Yet, further experiments on geometrically defined cell-network structures should be conducted to assess the required conditions for pacemaker relocation during heat stimulation. Such an approach might make it possible to elucidate the underlying mechanisms for heat-controlled pacemaker activation.

3.5 CONCLUSIONS AND OUTLOOK

Microwire arrays are effective tools for applying localized thermal stimulation to cells in culture. Overall, Figure 3.10 shows a schematic illustration of two possible phenomena arising during localized heat stimulation via an individual microwire. In the example shown in the schematic, the

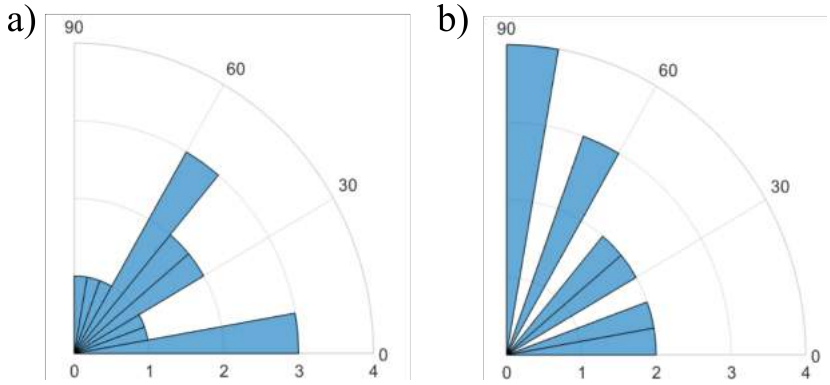

FIGURE 3.9: Distribution of propagation angles of the spontaneous signals (a, $n = 15$) and of the heat-stimulated signals (b, $n = 15$). The percentage of signals distributed along the direction of the heated wire with an angle $60° < \alpha < 90°$ changes from 20 % to 47 % after stimulation.

Ca^{2+} wave originally propagates from the upper left corner down to the bottom right. We conclude that a locally increased temperature can yield two possible effects in the cell network. Effect A is the disturbance of the Ca^{2+} wave pattern in the heated area due to localized changes in the propagation speed. Effect B is the thermal activation of another pacemaker in the heated area. The combination of these two effects can be seen in the center of the schematic, which is the disturbance of the signal wavefront together with the relocation of the pacemaker in the heated region.

We believe that heat stimulation in structured networks or tissues will allow more specific studies on pacemaker selection and local Ca^{2+} effects. This can be achieved by employing nanofabrication technologies to modify the geometry of the structured heating zones and confining cell growth to specific regions e.g. within a microfluidic compartment [102].

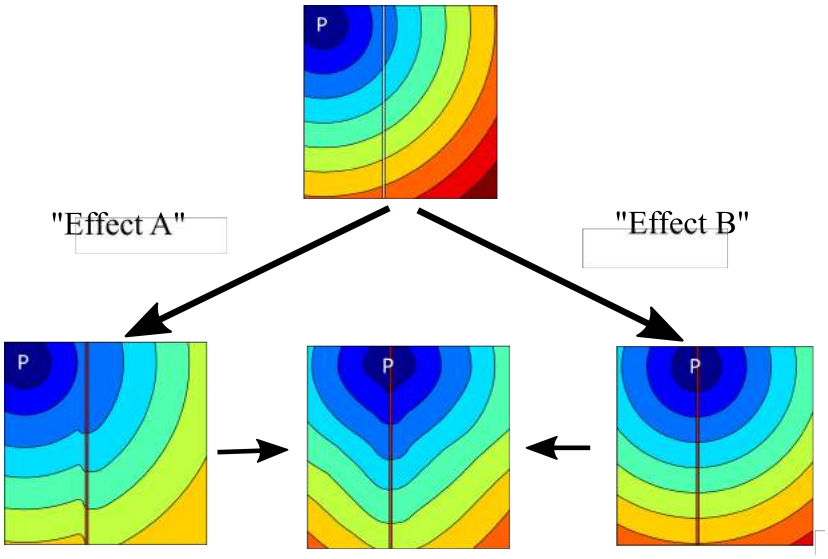

FIGURE 3.10: Schematic illustrating two possible effects of local heating to the Ca^{2+} dynamics of cardiac cells. Effect A: the Ca^{2+} wave is perturbed in the heated area by a local change in signal velocity. Effect B: a different pacemaker is activated in the heated area. Both effects may occur simultaneously.

CHAPTER 4

HEAT ACTIVATION AND GUIDANCE OF NEURITE OUTGROWTH

4.1 PREAMBLE

The present work aims to study the influence of temperature gradients on neurite outgrowth. This influence is studied using microwire array chips to generate local heat stimuli of PC12 neuron-like cells cultured on the chip. This chapter presents an experimental setup for neuronal heat activation. Additionally, the effects of localized temperature on the speed and direction of neurite outgrowth are investigated using an image processing method.

4.2 INTRODUCTION

Neurite outgrowth is a process of neuronal development in which neurites, either axons or dendrites, project from neuronal cell bodies to form neuronal networks. The leading edges of neurites, called growth cones, are motile structures that play a crucial role in neurite outgrowth and neurite guidance [103]. Research of Tischler *et al*. [41] has shown that PC12 cells have the capacity to grow neurite-like processes in response to nerve growth factor (NGF). In particular, it has been shown that the growth cones of PC12 cells contain microtubules and actin filaments, which play an important role in the process of neurite outgrowth [44]. In fact, the turning of neuronal outgrowth is thought to be driven by microtubules, and the protrusion of neurites is regulated by the polymerization of actin filaments [103, 104].

The response of growth cones to different external stimuli (guidance factors) causes the retraction or protrusion of neurites. In addition, the direction of neurite development is manipulated by the detection of guidance cues found in the surrounding environment [105]. Therefore, in order to improve neurite outgrowth and accurately orientate neurites towards a target indicated by guidance cues after injury, it is necessary to develop optimal cues that can induce neuronal regeneration. Over a few decades, it has become known that neurites can be guided by using several chemical cues [105, 106]. Other than that, physical cues such

as optical stimulation have been proposed as effective factors in regulating neurite outgrowth and neurite guidance [107–113]. Recently, it has been shown that spatial temperature gradients caused by near-infrared laser beams are capable of guiding neuronal growth [114]. The noticeable result of this study is that laser powers can drive neurite outgrowth towards the close vicinity of the infrared heat source. However, it is still unclear whether neurites react to the temperature gradient or the optical light generated from the near-infrared laser [115].

In this study, the influence of purely thermal stimulation on the neuron-like cellular growth will be inspected. In particular, temperature gradients produced by the microwire array chip will be presented here as a microscopic heating method to study the effects of temperature on the growth of neuron-like cells. Specifically, this study will investigate the speed and orientation of the neuronal growth depending on localized heat application.

4.3 MATERIALS AND METHODS

4.3.1 PC12 CELL CULTURE ON CHIPS

PC12 cells were cultured in RPMI-1640 (Sigma-Aldrich) supplemented with FBS (5 %, ThermoFisher Scientific), horse serum (10 %, Sigma-Aldrich), L-glutamine (1 %, ThermoFisher Scientific), and penicillin/streptomycin (0.5 %, ThermoFisher Scientific) in a humidified incubator at 37 °C and 5 % CO_2. The cells were passaged every 3-4 days.

Before cell plating, the chip was sterilized with UV light for 1 h and coated with Collagen IV (30 µg mL^{-1}, C5533-5mg, Sigma-Aldrich) overnight to enhance cell adhesion.

Cells were then detached from the Petri dish with trypsin-EDTA (Sigma-Aldrich) and collected in a 15 mL Falcon tube. After centrifugation, the cell pellet was resuspended in 500 µL of cell culture medium. A volume of cell suspension was pipetted on the chip's surface for a final concentration of approximately 1.5×10^5 cells/mm^2. The cells were then

incubated at 37 °C and 5 % CO_2 in the culture medium and 50 ng mL^{-1} of NGF-beta (SRP4304-20ug, Sigma-Aldrich) was pipetted into the reservoir to induce neurite outgrowth.

4.3.2 HEAT STIMULATION SETUP

The power supply on the chip was operated by software that had been developed in a previous project [98]. A voltage source capable of supplying an individual microwire with a computer controlled voltage was developed and built in Forschungszentrum Jülich. A detailed description of this system can be found in the dissertation of Philipp Rinklin [98]. Briefly, an overview of the main system shall be given here.

A schematic of the electronics setup is shown in Figure 4.1. A micro-controller is used to define the DC voltage for each channel. This system consists of a chip socket integrated into printed circuit boards (PCBs), which is then used to transfer input values from the micro-controller to the chip. In order to provide controlled powers for each channel on the chip, a software was used to enter power values. The program is able to measure the resistivity of the corresponding wire. Therefore, the voltages that correspond to the electrical power can be calculated using $V = \sqrt{PR}$, where V is the applied voltage, P is the power supply, and R is the resistance of the wire. The temperature across the microwire was measured using the FLIM method and then the outcome was compared to the simulation result using COMSOL Multiphysics.

4.3.3 THERMAL STIMULATION AND IMAGING

In order to investigate the effects of localized temperature on neuronal outgrowth, thermal stimulation was applied to a single microwire for 5 min (P = 1 W). The heat stimulation was applied three times. The resting time for the cells to recover between each stimulation was 10 min. The growth of the cells during heating was recorded using the Leica camera attached to the microscope. Images were taken with a 40x magnification objective. Before performing the experiment, the medium was replaced with fresh medium supplemented with NGF.

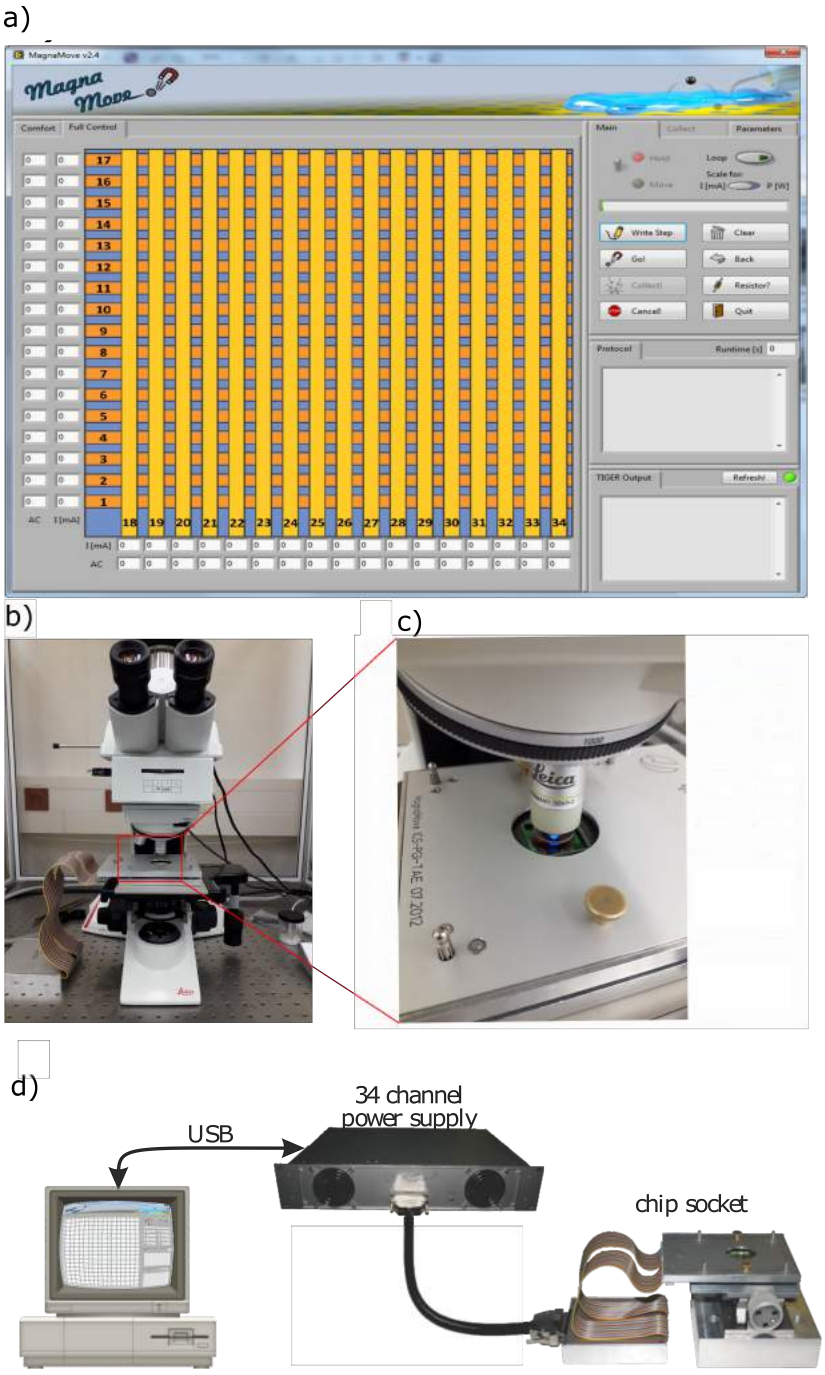

FIGURE 4.1: A schematic of the electronic setup. a) Screenshot of the software [98]. In this mode, the user is enabled to give a desired electrical power to each microwire. b) and c) The chip socket is fixed in the microscope. d) Schematic of the individual connections. The power supply is controlled via a custom LabView ® program connected via USB. The output of the power supply is directed to the contact pads via cables and custom PCBs [98].

4.3.4 IMAGE PROCESSING USING THE OPTICAL FLOW METHOD

To assess the growth of cells during the heat stimulation, the optical flow method was used to approximate the motion of image objects between two frames. Firstly, the frames were scaled down to 512 x 512 pixels to improve the speed of analysis. The frames were then filtered to subtract the background of microwire arrays. In order to eliminate the displacement of the frames during the experiment, the two frames were aligned before analysis using the cross-correlation method. Then the optical flow method was applied to plot a vector field, in which magnitudes of vectors indicate the velocity of moving objects between two frames. The assumption of this method is that the brightness of each pixel is constant in two analyzed frames. Therefore, the location of individual pixels is tracked based on the constant intensity using a spatial and temporal correlation analysis. The corresponding frames are correlated for determining the average spatial displacement of each pixel. The ratio of the displacement and the time scale between two frames gives the average velocity in each pixel. The details of this method can be found in the paper of Sun *et al.* [116].

4.4 RESULTS AND DISCUSSION

4.4.1 EFFECT OF TEMPERATURE GRADIENTS ON CELLULAR GROWTH

To investigate the influence of temperature gradients on neurite outgrowth, the microwire was supplied with 1 W of power for 5 min. The localized heat in a small region generates a temperature gradient, which can activate cells located in the vicinity of the heated wire. The neurite outgrowth during heating was observed and recorded by a Leica camera (DFC9000 GT). As can be seen from Figure 4.2b and 4.2c, a slight increase in the neurites' length can be observed in comparison to Figure 4.2a. Fur-

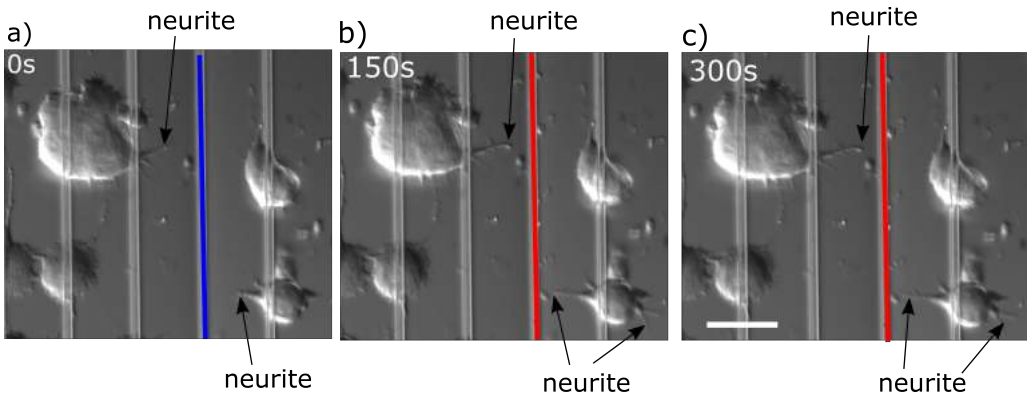

FIGURE 4.2: Neurite outgrowth in the presence of temperature gradients. a) before heating, b) at 150 s, c) at 300 s. The red and blue lines are the positions of the microwire with and without heat applied, respectively. The scale bar corresponds to 30 µm.

thermore, a localized temperature gradient across the microwire resulted in the protrusion of new neurites from PC12 cells within the first several minutes, as can be seen in the Figure 4.2b and Figure 4.2c.

In order to evaluate the rate of cellular growth or neurite outgrowth during stimulation, two frames, one at 0 s and one at 300 s, as shown in Figure 4.3a and 4.3b, were analyzed using the optical flow method. Before applying this method, the images were filtered to subtract the background as shown in Figure 4.3c. After that, a vector field was plotted using the optical method. Then, a descriptive vector plot was created, in which the number of pixels was scaled down 10 times for visual purposes, as shown in Figure 4.3d. From this figure, the vectors can be clearly seen at the edges of the cells after 300 s of heating. This indicates the extension of the cells, with the noticeable changes on their edges. As evidenced from Figure 4.3d, most of the changes occur in the edges of cells, which are the location of neurites. To quantify the speed of neurite extension, firstly a binary image using a threshold following Otsu's method [117] (Figure 4.4b) was calculated based on the magnitude of the original vector field to identify changing areas. Figure 4.4a shows the original vector field in which the vectors are indicated the rate of change at each pixel. The vectors are too small that the magnitude is practically invisible in the plot. The changing areas are blue and yellow colors, as can be seen in Fig-

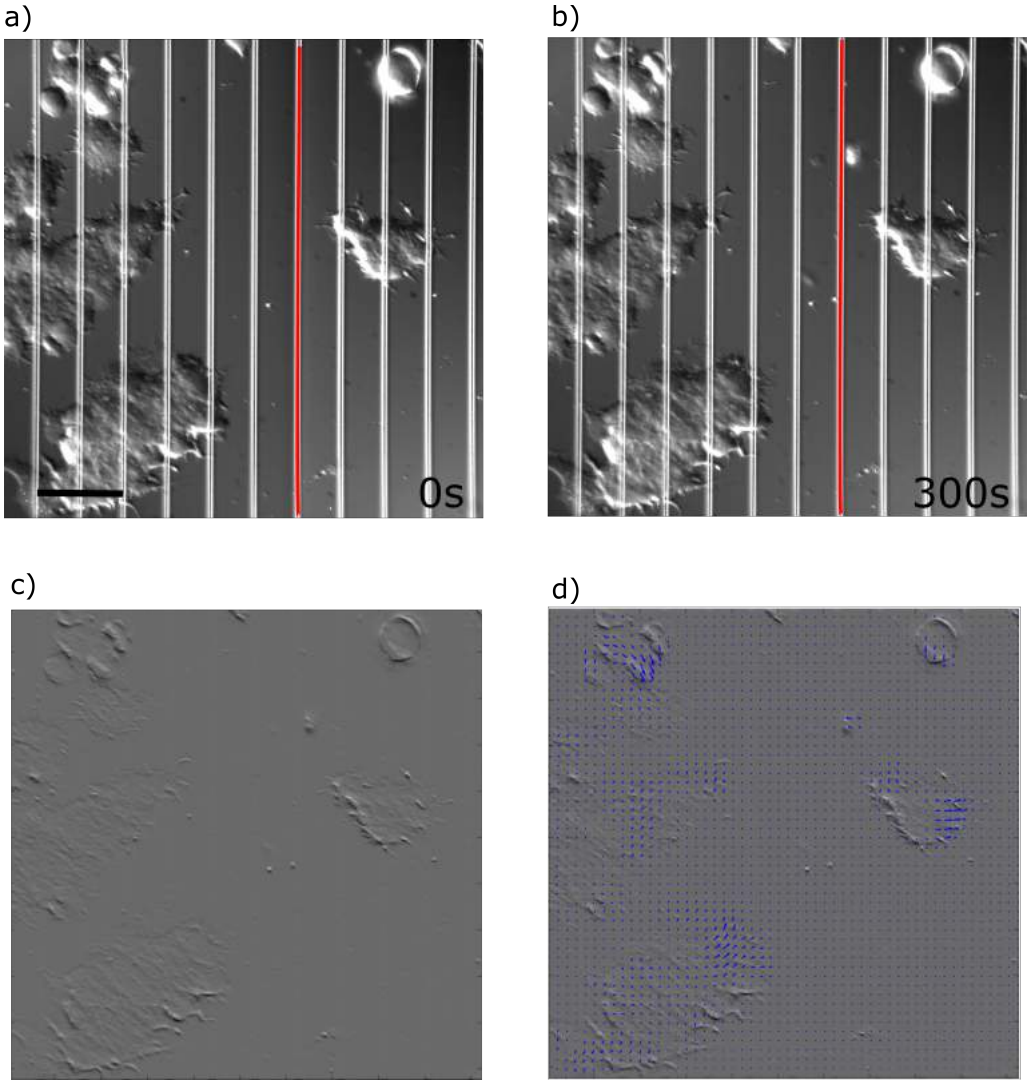

FIGURE 4.3: An analysis of the speed of cell extension via image processing. a) An image of the PC12 cells on the microwire chip at 0 s. b) An image of PC12 cells on the microwire chip after 300 s heat stimulation. c) A filtered image after subtracting the background of microwire array. d) A descriptive vector field plot depicts the cells extension analyzed by the optical flow method. The scale bar corresponds to 60 µm.

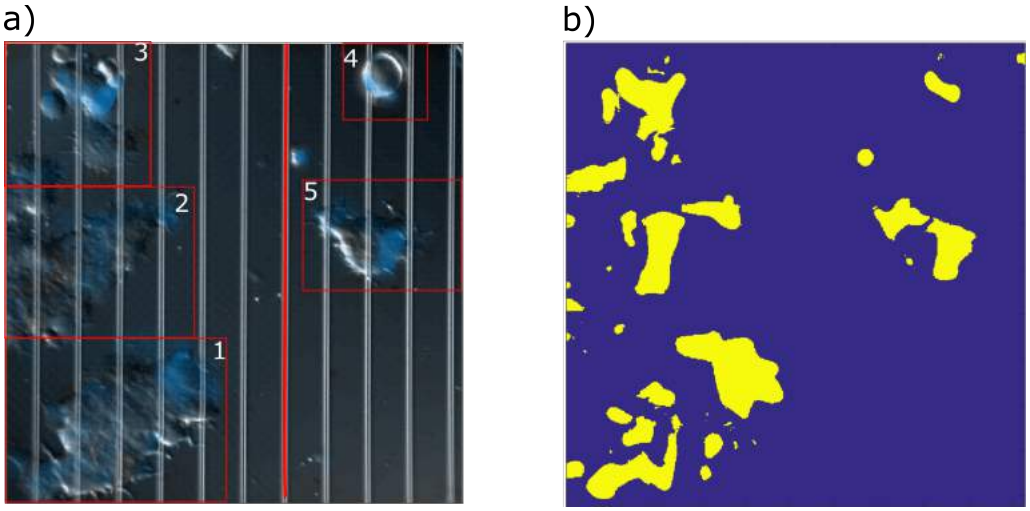

FIGURE 4.4: Two images describe changing areas during heat stimulation. a) The blue areas describe a group of vectors resulting from the optical flow method. These areas exhibit changing parts of the cells. The red line is the position of the heated wire. b) A binary image describes the non-changing (blue) and changing (yellow) parts of the cells.

ure 4.4a and Figure 4.4b, respectively. Subsequently, the changing areas were localized and marked with numbers as shown in Figure 4.4a. After that, the velocity of each changing cell area was calculated for cases without and with heat stimulation. Finally, the average velocity of the cell extension or neurite outgrowth without and with heat stimulation was evaluated as shown in Figure 4.5. As can be seen from the figure, the average velocity of cell extension is increased during heating. The average speed of the first heat stimulation is $(0.06 \pm 0.03)\,\mu m\,min^{-1}$, which is higher than the average speed of spontaneous growth $(0.03 \pm 0.01)\,\mu m\,min^{-1}$ at room temperature.

This result is consistent with a previous report of neurite outgrowth under the influence of an infrared laser, which claims that the growth rate of neurites from PC12 cells with heat stimulation is higher than $0.03\,\mu m\,min^{-1}$ [110]. A decrease of the growth rate during the second heat stimulation is visible (Figure 4.5). However, the growth rate of cells seems to recover in the third heat stimulation ($(0.04 \pm 0.01)\,\mu m\,min^{-1}$). Furthermore, the increase in the growth rate of the cells with the first

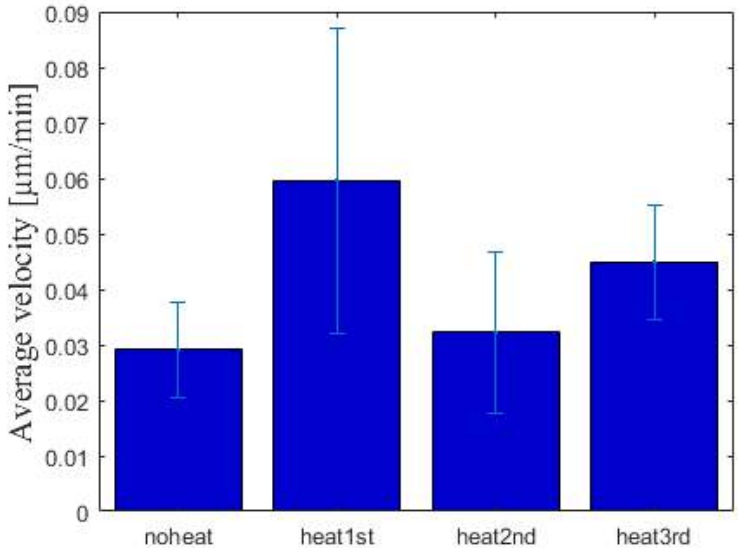

FIGURE 4.5: The average speed of the cellular growth without and with heat stimulation. The error bars present the standard deviation.

heat stimulation was observed in 80 % of samples (n = 10) (Figure 4.6). This result indicates that the temperature gradient created by a sudden rise of temperature affects the increase of the cellular growth. The abrupt increase of temperature is the key factor for triggering the high speed of neurite growth, which is in agreement with the conclusion of Oyama *et al.* [78]. Though, the kinetic effect of enzymatic activity has not been investigated in this experiment, the rapid increase in temperature could result in an unbalanced equilibrium of tubulin polymerization and enhance the polymerization of microtubules. This process mediates the sliding of neurite outgrowth during heating [118]. Moreover, temperature gradients generated by microscopic heating activate actin polymerization, which could contribute to the elongation of neurites [119]. Further experiments on the influence of heat on cytoskeletal components, either actin filaments or microtubules, and molecular motors should be conducted to assess proteins involved in the growth of cells as well as how the interaction between these proteins affects the stabilization of actin filaments

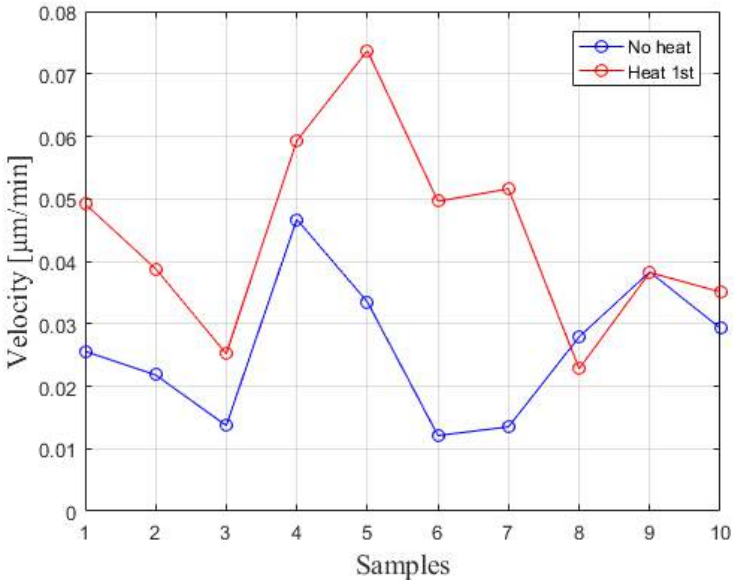

FIGURE 4.6: The average growth speed of the cellular growth without and with the first heat stimulation of the samples.

and microtubules. This approach may make it possible to elucidate the underlying mechanism of heat-induced neurite outgrowth.

4.4.2 INFLUENCE OF TEMPERATURE GRADIENTS ON THE DIRECTION OF CELLULAR GROWTH

In order to examine the effect of temperature gradients on the guidance of cellular growth, various directions of cell development were evaluated based on the vector plot (Figure 4.4a). The location of cell areas was marked by numbers as shown in the Figure 4.4a. The mean angle of the direction of cellular growth was evaluated for each cell area. Figure 4.7 shows the directions and the rates of cell development in each area.

In Figure 4.7, the cells located in areas two, three, and four show visible growth towards the heated wire. However, the growth direction of cells located in areas one and five varied each time heat was applied. This effect might be caused by the heated wire's close proximity to the leading edges of these cells. The distance of these areas from the heated wire was approximately 10–30 µm.

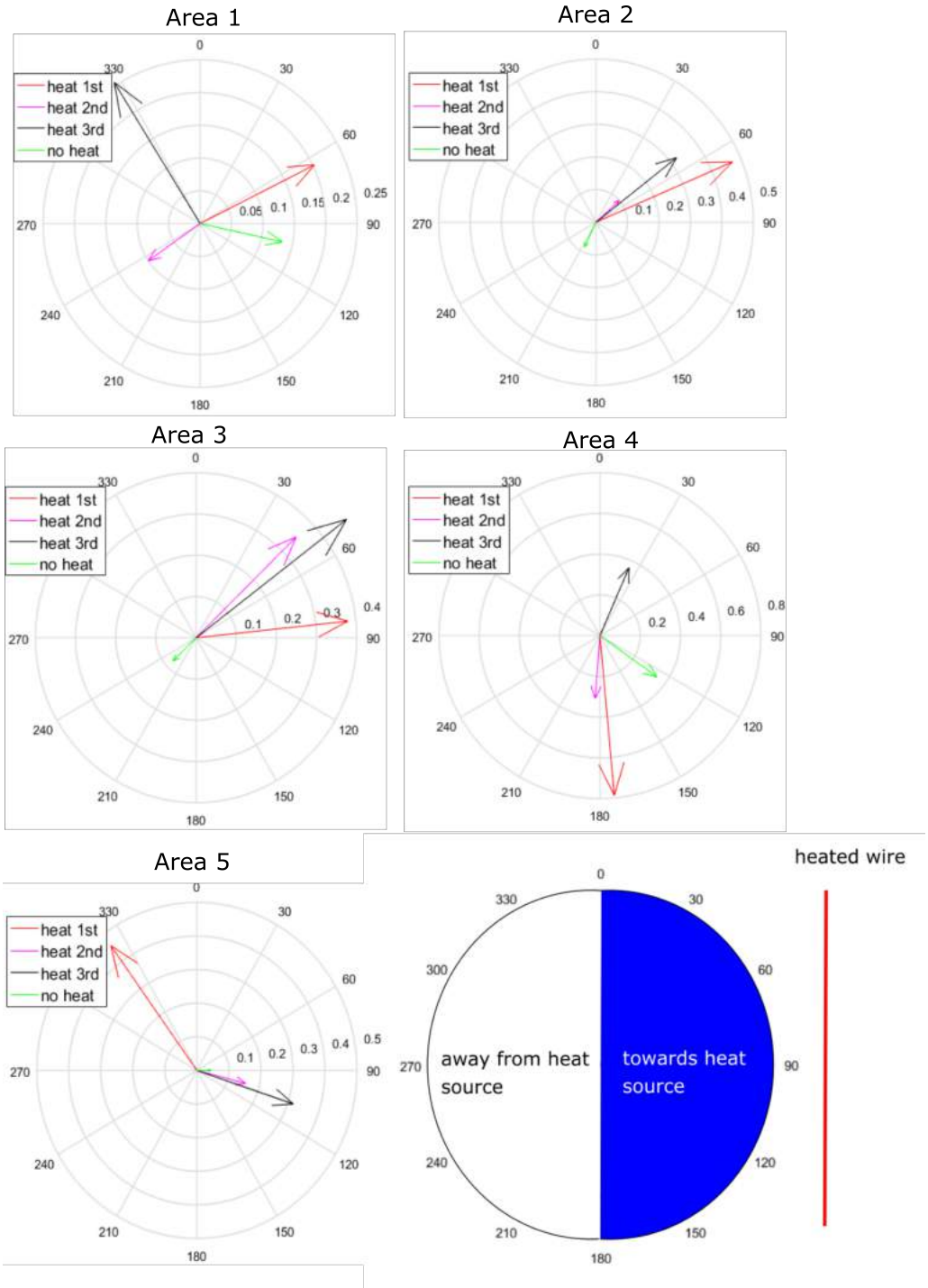

FIGURE 4.7: Average angle distribution describing the direction of neurite outgrowth in area one, two, three, four, and five. The cell areas are marked on the vector field from the Figure 4.4a.

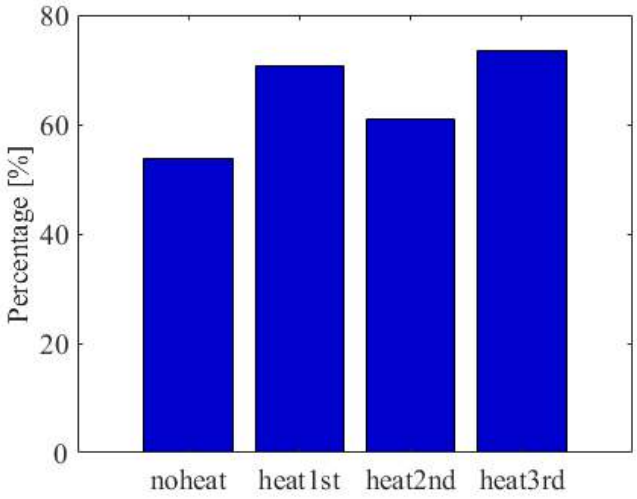

FIGURE 4.8: Percentage of cellular growth towards the heated wire in cases of no heat, first-heat, second-heat and third-heat stimulation ($0° < \alpha < 180°$), $n = 41$.

To further investigate the role of microscopic heating on cellular development, the percentage of cellular growth towards the heated wire was calculated as shown in Figure 4.8. The cells developed towards the heat source with a defined angle α ($0° < \alpha < 180°$ see Figure 4.7). It can be seen that the percentage of cell areas which developed towards the heat source increased with the heat stimulation (70 %, 62 %, and 72 % at the first-heat, second-heat, and third-heat stimulation, respectively), whereas the spontaneous growth was 54 % ($n = 41$). This result indicates that the temperature gradient was a guidance cue affecting the development of neuron-like cells. This effect is in line with studies on the neurite attraction of a laser-based micro-heater or optical guidance [110, 120].

In order to investigate the development of PC12 cells in the long term after heat stimulation, the cells were observed 24 h after the heat experiment. The effect of localized heating on neurite guidance can be clearly visualized in Figure 4.9, which shows that the neurites elongated towards the heated wire 24 h after heating. It can also be seen that some new cells migrated towards the heated wire. Furthermore, the growth of the cells located in close proximity to the heat source (area five) degraded, while

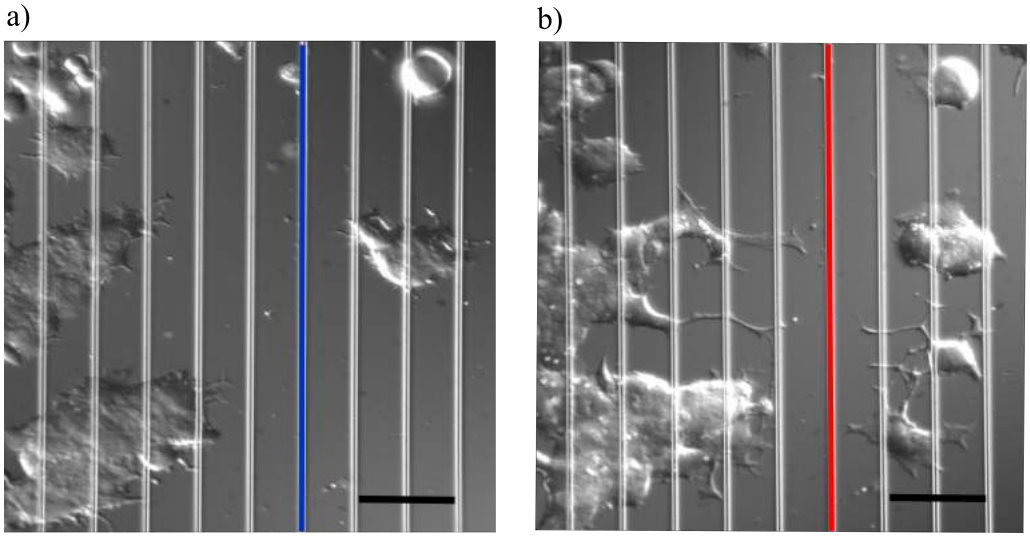

FIGURE 4.9: a) Exemplary image of neurite outgrowth before heating compared to b) neurite outgrowth towards the heat source after 24 h heating. The scales bar correspond to 60 µm.

the growth of the cells located far from the heat source continued to elongate after heating. This observation indicates that the growth of neurites is guided by the temperature gradient on the microwire array chip.

Overall, microscopic heating based on microwire array chips showed an ability to guide neurites by means of localized thermal stimulation. The underlying mechanisms of the turning direction behind growing neurites has not been further studied in this work. However, the research of Henley *et al.* showed that the growing neurites' directions were influenced by the concentration of intracellular calcium [106]. On the other hand, Furukawa *et al.* demonstrated that the thermal fluctuation near the cells induced rapid changes in the intracellular calcium gradients of cell membrane [121]. This resulted in the influx of calcium through plasma membrane, which contributes to the increase of calcium concentration on the tips of neurites. The local increase of calcium concentration may activate calcium sensitive kinases, phosphatases (e.g. calcineurin) and other effectors (e.g. Rho-GTPases), which in turn modulate the dynamics of actin and microtubule elements to steer the growth cone [106, 122].

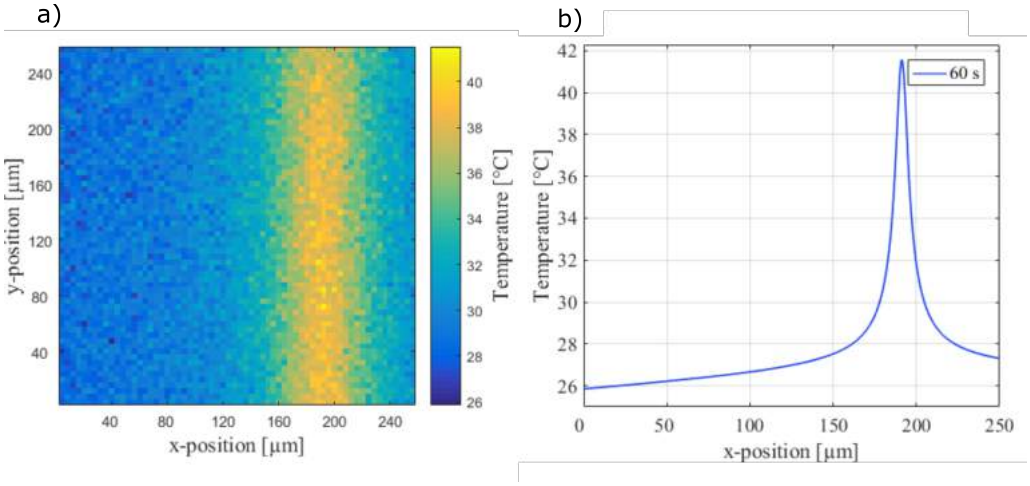

FIGURE 4.10: a) Temperature profile on the top of the microwire is determined experimentally (FLIM) and b) via FEM simulation. The ambient temperature is $T_0 = 26\,°C$.

4.4.3 TEMPERATURE DISTRIBUTION ON MICROWIRE

In order to identify the temperature distribution on the microwire, the temperature was first measured using the FLIM method. The microwire was supplied with 1 W of electrical power for 1 min. The ambient temperature was 26 °C. For this measurement, a rhodamine B was encapsulated on the chip and then placed under a confocal laser scanning microscope. The microscope was focused on the heated wire and then moved up to a plane 5 µm from this point. Figure 4.10a shows the temperature profile of the heat distribution measured by the experimental method. Figure 4.10b shows the temperature on the top of the microwire as determined by COMSOL simulations. In both cases, the plots show a clearly localized high temperature region over the heated wire. Comparison of the experimental data with the simulation result shows that the temperature in this region is close to 42 °C. However, the width of the high-temperature region in the experimental data is slightly broader than in the simulation method. This result may cause from the temperature at the chip's surface being captured at a plane 5 µm away from the wire when using a microscope in the FLIM method.

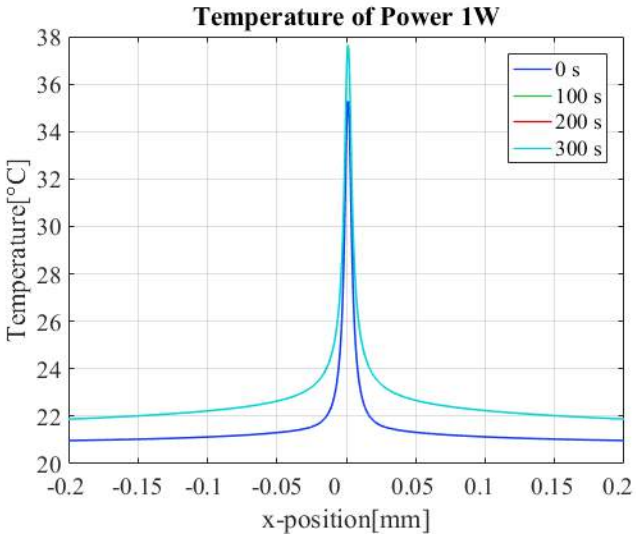

FIGURE 4.11: Temperature profile on the surface of the chip at 300 s simulated by COMSOL Multiphysics. The temperature rapidly increases and reaches the constant value at 37.9 °C. The temperature at 200 s and 300 s is identical, therefore, the temperature at 200 s is invisible on the plot. The ambient temperature is T_0 = 21 °C.

To determine the temperature profile in the real experimental conditions with neuron-like cells, the COMSOL simulation was used. The ambient temperature was at 21 °C. The power supply was 1 W for 5 min. The result is shown in Figure 4.11. As can be seen from the graph, the temperature of the microwire rapidly reaches its peak of 37.9 °C. It then remains constant for 5 min.

4.5 CONCLUSIONS AND OUTLOOK

In conclusion, the study confirmed that the neuron-like cells (PC12 cells) can sense and respond to the temperature gradients. These results indicate that the increase of temperature in the vicinity of the cells can be considered as a physical guidance cue for neurite outgrowth. These findings support previous reports regarding laser-based studies, which also use temperature gradients for the stimulation of neurons [78, 114]. Additionally, the results provide a promising approach for neurite regen-

eration studies, in which temperature gradients can be used as a factor to promote high speed neurite outgrowth.

CHAPTER 5

FABRICATION OF MICROCHANNEL STRUCTURES FOR NEURONAL GUIDANCE TOWARDS HEAT ACTIVATION

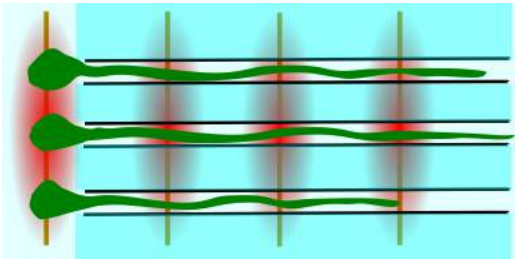

This chapter was reproduced in part with permission from "Ka My Dang, Philipp Rinklin, Jan Schnitker, Bastian Haberkorn, Kathrin Zobel, Simona Gribaudo, Anselme L.Perrier, Jorne Carolus, Michaël Daenen, Stefan Weigel, Harald Luksch, Andreas Offenhäusser and Bernhard Wolfrum, Fabrication of precisely aligned microwire and microchannel structures: Toward heat stimulation of guided neurites in neuronal culture. *Phys. Status Solidi A*. 2017, 1600729. DOI: 10.1002/pssa.201600729".

5.1 PREAMBLE

In this chapter, the author presents a new fabrication approach, based on standard clean room fabrication and sacrificial layer etching, for combining microwire arrays with a set of orthogonal axon-guiding microchannels on-chip. This approach allows the positioning of neurites, as well as control over their polarity. The system permits the application of strong temperature gradients, enabling localized thermal stimulation inside microchannels.

5.2 INTRODUCTION

Neurite outgrowth is a key process in the development of functional neuronal circuits and the regeneration of the nervous system following injury [123]. Understanding the regulation of neurite outgrowth is crucial for developing therapies to promote axon regeneration after injury or in neurodegenerative diseases [124, 125]. Chapter 4 shows that localized heat induces an increase in the speed of cell growth as well as influences the direction of the cell growth. In order to investigate the changing behaviour of isolated neurites under the influence of thermal stress, it is desirable to grow neurons into specific regions where functional components are located.

In recent years, microfluidics and micropatterning have become promising tools for neuroscience, as they allow the construction of guided neuronal networks [50, 54, 126–129]. Furthermore, these methods enable high-throughput screening of neurite outgrowth [18]. The main advantages of microfluidic cell culture techniques are a reduced sample volume and the opportunity to precisely manipulate the extracellular environment.

Two fabrication approaches for axon-guiding channels are presented in this chapter. These are a soft-lithography (for fabrication of PDMS microchannels) and a sacrificial layer (for fabrication of SU-8 microchannels) technique.

In order to assess the ability of neurites to grow into the fabricated microchannels, PC12 cells are cultured on the chip. The PC12 cell line is derived from a transplantable rat pheochromocytoma [41] and has been widely used as an *in vitro* model for Parkinson's disease (PD) [130]. A notable feature of PC12 cells is that they respond to the nerve growth factor (NGF). In response to NGF, PC12 cells develop neurites and form neuronal networks [42]. These cells are used for studies regarding neurite outgrowth. This chapter shows the ability of neurites to grow inside the microchannel in the direction induced by the axonal guiding channels.

5.3 MATERIALS AND METHODS

5.3.1 FABRICATION OF PDMS MICROCHANNELS

In order to fabricate PDMS microchannels, PDMS prepolymer mixture (10:1) was poured into a master mold produced by patterning SU-8 on the silicon wafer. The structure of the master mold is shown in Figure 5.1. The PDMS mixture was then cured at 64 °C for 24 h in an oven. Then, the PDMS structure was peeled off the master and the structure was cleaned with Isopropanol and Mili-Q water. Subsequently, a biopsy punch with a diameter of 6 mm was used to create reservoirs for placing cells. Two reservoirs were punched on the left and right, which serve as inlets and outlets for loading cells and the culture medium. Figure 5.1b shows an array of microchannels which offer bridges to connect the inlets and outlets of the device. As can be seen in Figure 5.1c, this microchannel structure is asymmetrical with an inlet width of 15 µm and an outlet width of 3 µm. The height and length of the microchannel are 3 µm and 500 µm, respectively. To bond the microchannel to the chip, the PDMS structure and the microwire array chip were treated with oxygen plasma (0.8 mbar, 20 min, 80 W). Then, the PDMS and the chip were immersed in (3-Mercaptopropyl)trimethoxysilane (MPTMS) and (3-Glycidyloxyropyl)trimethoxysilane (GPTMS), respectively, for 1h. Finally,

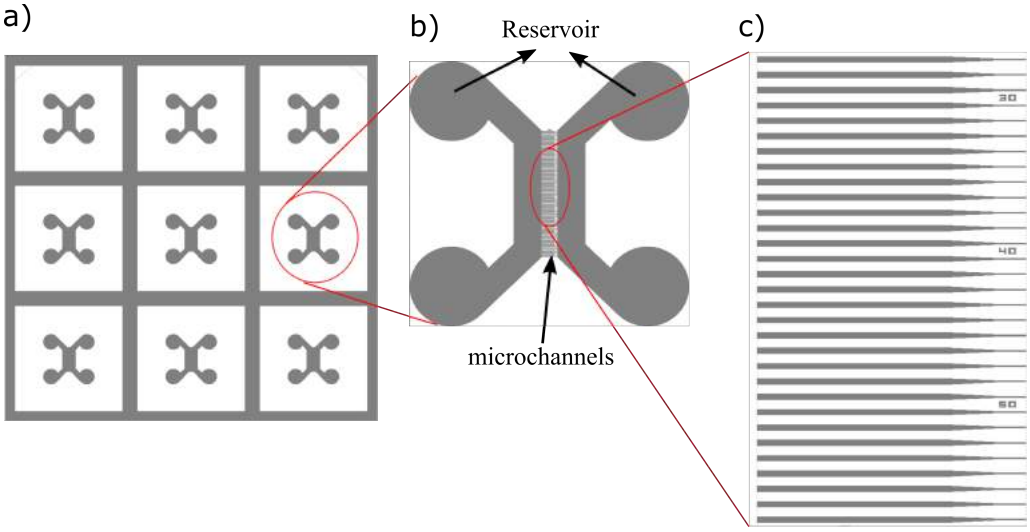

FIGURE 5.1: a) The structure of a master mold on a silicon wafer. b) The structure of a single device. c) An array of microfluidic channels structure.

the PDMS microchannel was aligned with and bonded to the microwire array chip under a pressure of 30 kPa overnight.

5.3.2 FABRICATION OF ALIGNED SU-8 MICROCHANNEL

Microfluidic axon guiding channels were fabricated perpendicular to the microwire array on the chip. A schematic of the microwire array and microchannel fabrication process is shown in Figure 5.2. The geometrical feature of the microchannels was determined by a sacrificial layer of resist (LOR30B, Microchem). In order to achieve a high thickness of 4 µm for the microchannels, the first layer of resist (LOR30B) was spin-coated at 2000 rpm for 30 s. The resist was then soft-baked at 150 °C for 5 min. A second layer of negative photoresist AZ nLOF 2020 (MicroChemicals, Ulm, Germany) was spin-coated at 3000 rpm for 30 s and soft-baked at 115 °C for 90 s. After exposure, the wafer was post-baked at 115 °C for 90 s. Then, MIF 326 (micro resist technology GmbH, Berlin, Germany) was used to develop the resist for 46 s. To form the LOR30B microchannel as a sacrificial layer, acetone was used to strip off AZ nLOF 2020 within 1h. A layer of SU-8 (GM 1075, Gersteltec Sarl, Switzerland), which is an epoxy-based resist for fabrication of thick layer structures (>100 µm), was

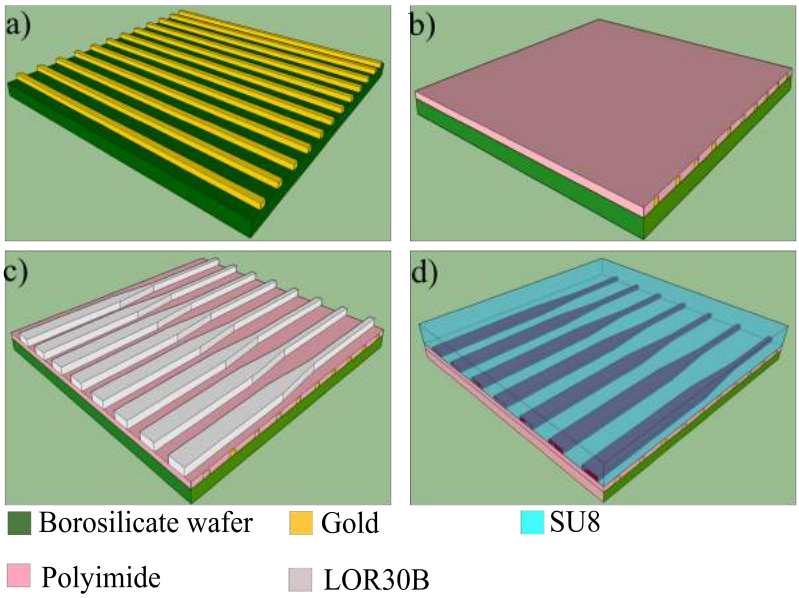

FIGURE 5.2: Schematic of the microwire array and microchannel fabrication process. a) Microwire arrays were patterned on a borosilicate wafer. b) Polyimide was spin-coated on top of microwires. c) The microchannel structure of LOR30B resist was patterned on top of polyimide. d) The SU-8 structure was deposited to make microchannels after etching LOR30B.

spin-coated at 950 rpm for 100 s, and then soft-baked at 40 °C for 1.5 h. Subsequently, the wafer was left overnight at room temperature to enhance the adhesion of SU-8 to the surface of the wafer. After this resting time, a soft-bake with a temperature ramp from 40 °C to 120 °C in 15 min followed by a plateau at 120 °C for 20 min was carried out. Finally, the wafer was cooled to room temperature. Subsequently, wall structures enclosing the sacrificial layer resist were patterned using photolithography. After exposure, the SU-8 was post-baked using a temperature ramp from 40 °C to 95 °C in 15 min and kept at 95 °C for 1h before cooling down to room temperature. Subsequently, mr-DeV 600 (micro resist technology GmbH, Berlin, Germany) developer was used to develop SU-8 for 4 min. Finally, to create the axon guiding channels, the developer (MIF326, micro resist technology GmbH, Berlin, Germany) was used to etch away the LOR30B sacrificial layer. A diagram describing the individual steps for microchannel fabrication is shown in Figure 5.3.

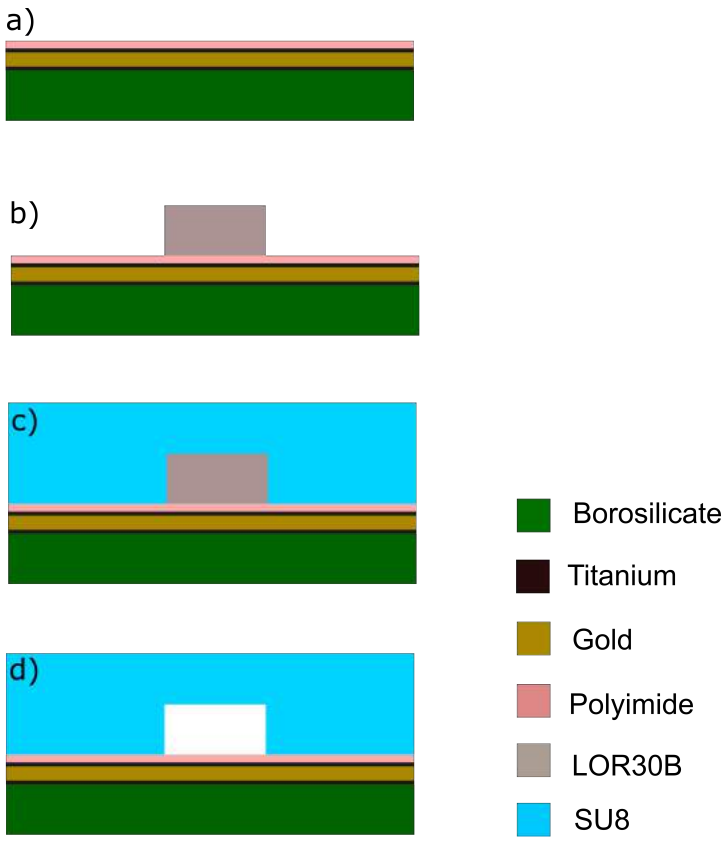

FIGURE 5.3: Schematic diagram describing the steps of the microchannel fabrication. The figures show the cross section of a single channel structure. a) Ti/Au/Ti and polyimide were deposited on a borosilicate wafer. b) LOR30B sacrificial layer (4 µm) was deposited and c) a thick layer of SU-8 was deposited on the top of LOR30B photoresist. d) The actual microchannel was fabricated by wet etching the LOR30B photoresist layer.

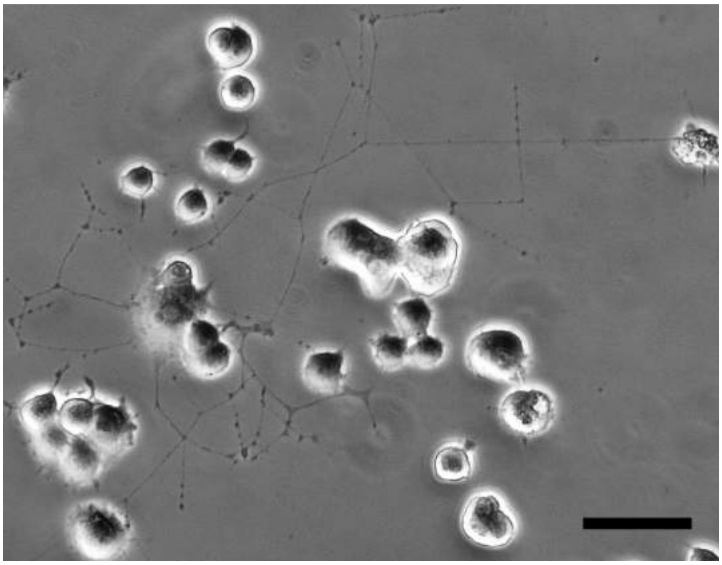

FIGURE 5.4: Neurite outgrowth from PC12 cells at DIV4. Scale bar corresponds to 50 µm.

5.3.3 CELL CULTURE

CULTURE OF PC12 CELLS ON THE SU-8 MICROCHANNEL CHIPS PC12 cells were cultured in RPMI-1640 (Sigma-Aldrich) supplemented with FBS (5 %, ThermoFisher Scientific), horse serum (10 %, Sigma-Aldrich), L-glutamine (1 %, ThermoFisher Scientific) and penicillin streptomycin (0.5 %, ThermoFisher Scientific) in a humidified incubator at 37 °C with 5 % CO_2. The cells were passaged every 3-4 days. Figure 5.4 shows the differentiated state of PC12 cells on DIV4.

Before cell plating, oxygen plasma treatment (0.8 mbar, 80 W, 2 min) was used to hydrophilize the chip surface. Immediately after plasma treatment, 300 µL of Milli-Q water were pipetted onto the chips. Subsequently, the chips were sterilized with UV light for 1 h and coated with Collagen IV (30 µg mL^{-1}, C5533, Sigma-Aldrich) to enhance cell adhesion.

The cells were then detached from the Petri dish using trypsin-EDTA (Sigma-Aldrich) and collected in a 15 mL Falcon tube. After centrifugation, the cell pellet was resuspended in 500 µL of cell culture medium. A volume of 10 µL of the cell suspension was pipetted onto the side of the

microchannel inlet for a final concentration of approximately 10^6 cells/mm^2. The cells were then incubated at 37 °C for 15 min. Subsequently, 10 µL of the cell suspension was pipetted onto the outlet side of the microchannel. After 15 min incubation at 37 °C with 5 % CO_2 to enhance the attachment between cells and the substrate, 500 µL of culture medium supplied with 50 ng mL^{-1} of NGF-β (SRP4304-20ug, Sigma-Aldrich) was pipetted into the reservoir to induce neurite outgrowth.

5.3.4 FLUORESCENCE IMAGING OF THE NEURITE LENGTH IN MICROCHANNELS

In order to clearly observe the cells inside the microchannels, a green fluorescent dye, calcein-AM (17783-1mg, Life Technology), was used to stain the cells. The cells cultured on the chip (DIV14) were incubated with calcein-AM at a concentration of 4 µM diluted in serum free RPMI for 10 min at 37 °C to allow the dye to penetrate the cell membrane. The cells were then incubated in fresh pre-warmed culture medium (see above) for 30 min at 37 °C. Images were taken with a 20x magnification objective. The length of the neurites was measured using the ImageJ software.

In order to maintain the viability of neurites and keep tracking the development of neurites inside the microchannels, CellTracker Green (CMFDA, C2925, ThermoFisher Scientific) was used to stain the cells. The cells were incubated at 37 °C with 10 µM CMFDA dissolved in serum-free RPMI for 30 min. Subsequently, the cells were washed with the medium and then incubated for 30 min in culture medium with NGF at 37 °C. After that, the cells were transferred to the microscope for imaging.

5.4 RESULTS AND DISCUSSION

5.4.1 PDMS MICROCHANNELS AND ITS DRAWBACKS

The PDMS microchannel structure and the microwire chip are shown in Figure 5.5. There are two reservoirs on both sides of the PDMS struc-

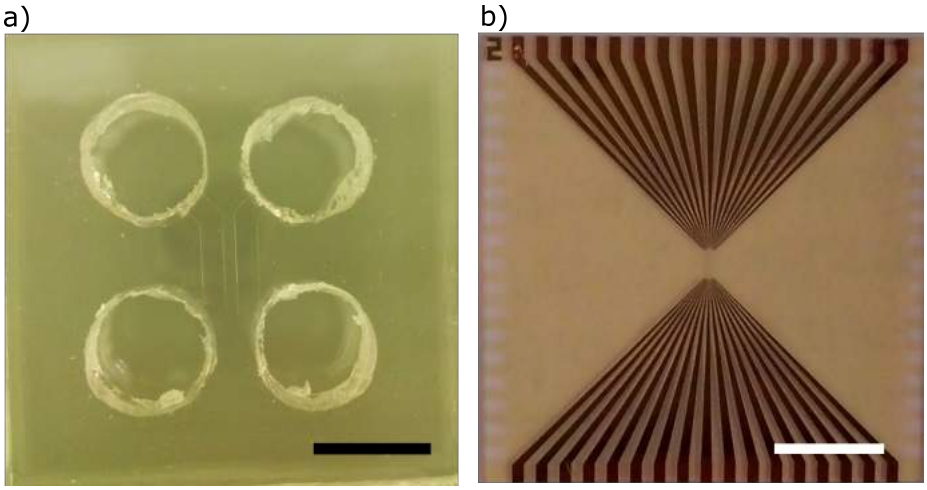

FIGURE 5.5: a) A PDMS microchannel structure and b) a microwire array chip. The scales bar correspond to 6 mm.

ture for cell loading. The diameter of each reservoir is 6 mm. Cells were first pipetted into the chamber. The cells form neurites in the chamber responding to NGF treatment. Subsequently, the neurites grow along the microchannels and reach the opposite chamber. Figure 5.6 shows the PDMS microchannel aligned on the microwire array chip's surface and PC12 cells cultured on the chip. From Figure 5.6, it is visual that some neurites protrude into microchannels. The Figure shows perfect alignment between the PDMS microchannels and microwire arrays. However, the PDMS microchannels have some limitations that should be considered while doing the experiment with the cells. Firstly, misalignment of the PDMS microchannel and the microwire structure of the chip could occur for practical reasons. Additionally, the delamination of PDMS microchannels from the chip's surface is a problem in the long-term cell culture experiment. Figure 5.7 shows neurites growing into the gap between microchannels and the surface at DIV4. Another problem of PDMS microchannels is that the PDMS microchannels are non-reusable. Once the PDMS microchannels are bonded to the chip, the bond is permanent. Therefore, this device can be only used for one batch of the cell culture because the cells may not be completely removed from the complex PDMS

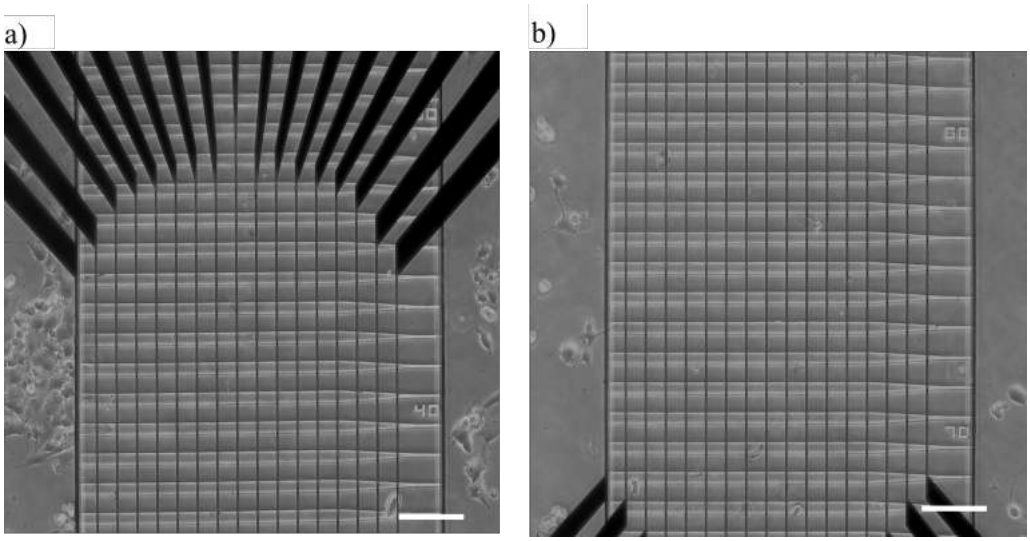

FIGURE 5.6: Aligned PDMS microchannel and PC12 cell culture on the chip. a) top side, b) bottom side. Scale bars correspond to 100 µm.

structure. For these reasons, the fabrication of microchannels using another method is desirable for cellular studies.

5.4.2 MICROWIRE ARRAY AND SU-8 MICROCHANNEL STRUCTURES

The fabrication of the microwire arrays was presented in section 3.3.1. Briefly, the microwire array structures include 17 microwires patterned in parallel. The width of each wire is approximately 2.5 µm. The thin designs of the microwires enable high temperature confined on a small area surrounding the microwire. This allows thermal stimulation of neurites growing inside microchannels without harming the cell somata, which are located outside the microchannel.

To fabricate the SU-8 microchannel structures, LOR30B resist was used as a sacrificial material in the microchannel fabrication process. While chromium sacrificial layers are routinely used for the fabrication of nanofluidic channels and nanocavity devices [131], chromium deposition and lift-off procedures are typically of limited value concerning the fabrication of structures several micro-meters in height. Here, LOR30B pro-

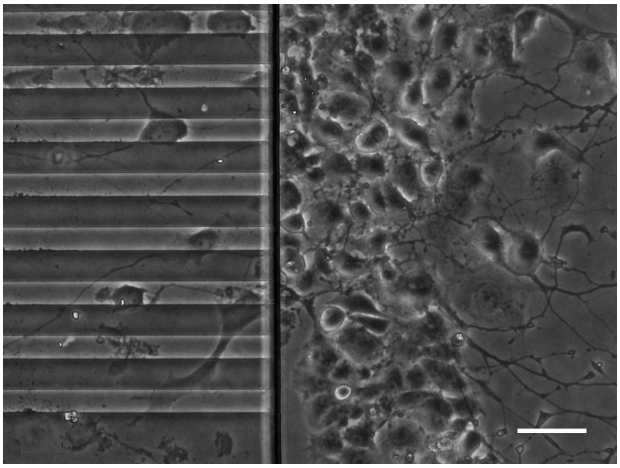

FIGURE 5.7: Neurites grow into the gap between microchannel and suface because of the delamination. Scale bar corresponds to 50 µm.

vides advantages, as it can readily be used for the fabrication of sacrificial layer structures in the micro-meter regime. Moreover, the LOR30B resist is based on poly-dimethylglutarimide (PMGI), a deep-UV positive resist used mainly for bilayer lift-off processes. PMGI is a good sacrificial layer candidate compatible with SU-8 [132, 133]. It complies with a variety of thicknesses and has a glass transition temperature of 190 °C, which is greater than the processing temperatures required for SU-8 [133]. Thus, the resist is compatible with the post-bake and development process of SU-8 due to its high thermal and chemical stability. The structure of the microchannels is shown in Figure 5.8a. The wall structure of SU-8 above the microchannels is shown in Figure 5.8b. The final structure of the microchannel is shown in Figure 5.8c. The tapered shape of the microfluidic structure was chosen to allow control over the neurites' polarity [134]. The final height of the microchannel is determined by the thickness of the LOR30B resist, which was spin-coated to a thickness of 4 µm. The height of the resist layer was chosen to prevent the cell bodies from entering the axon guiding channels. Figure 5.9 shows SEM images of the SU-8 wall structure and the microfluidic channel after sacrificial layer etching. As can be seen in Figure 5.9a, the height of the SU-8 wall is in the range of 120 µm. Figure 5.9b shows the outlet of an individual microchannel with a width of 8 µm and a height of 4 µm.

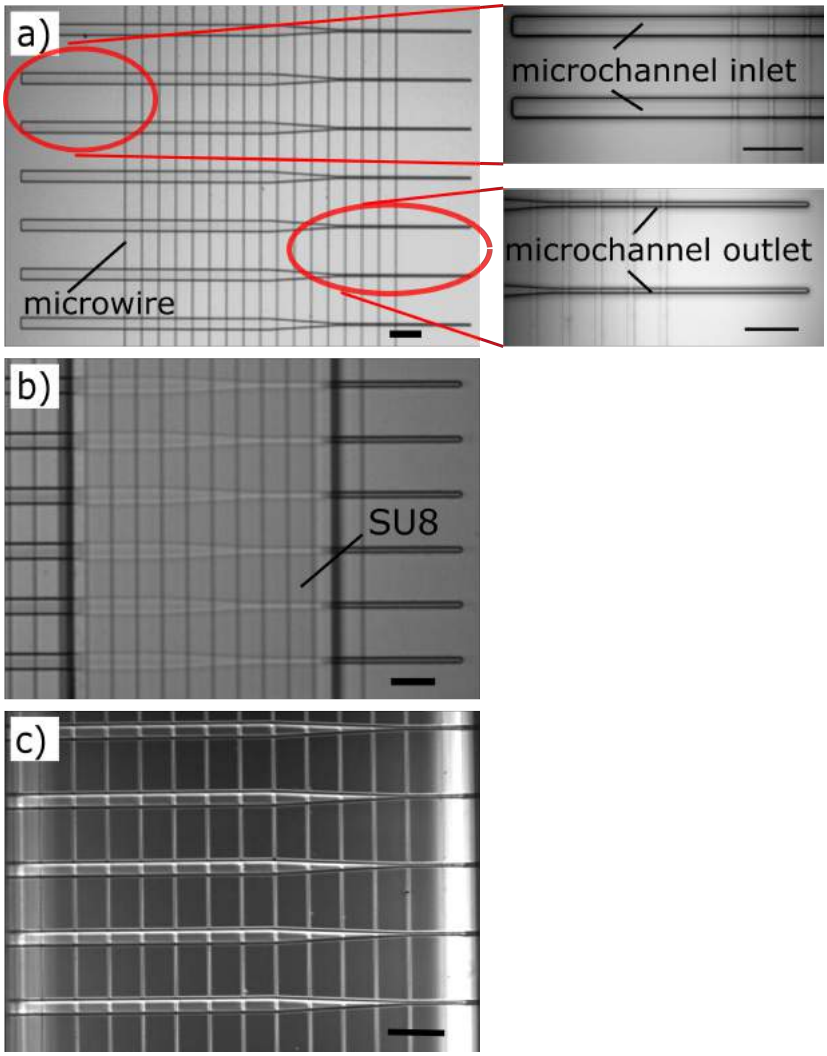

FIGURE 5.8: a) Structure of the LOR30B resist microchannels patterned on the top of microwire arrays, b) as well as the wall structure of SU-8, and c) the microchannel structure and microwire array. Scale bars correspond to 50 µm.

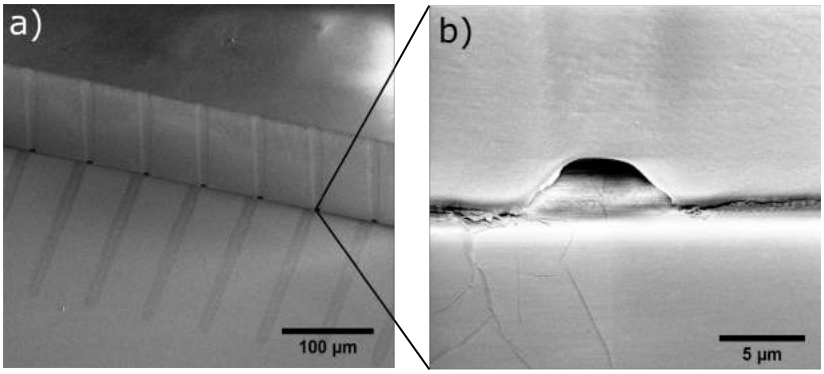

FIGURE 5.9: a) SEM images of the SU-8 wall structure and b) an enlarged view of an individual microchannel outlet.

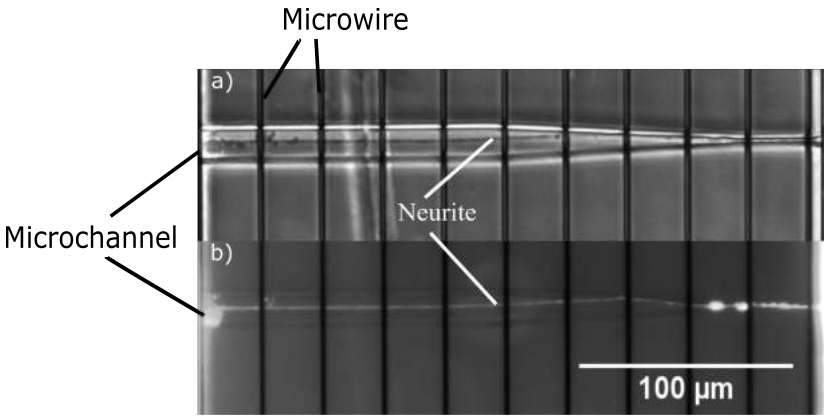

FIGURE 5.10: Neurite outgrowth inside microchannel. a) Phase contrast and b) fluorescent image of neurite growth directed into a microchannel. The arrows indicate the position of the neurite.

5.4.3 NEURITE OUTGROWTH INTO SU-8 MICROCHANNELS

Proof-of-principle experiments were performed to investigate the neurite extension of PC12 cells into the microchannels. Figure 5.10 shows neurite extension into the microchannels over the course of several days in culture, using a combination of microscopy techniques including phase contrast and fluorescence microscopy. In Figure 5.10a, the outline of the channel perpendicular to the microwire array can be seen. A neurite is growing from left to right. The fluorescent image confirms the penetration of the neurite to the end of the microchannel (Figure 5.10b).

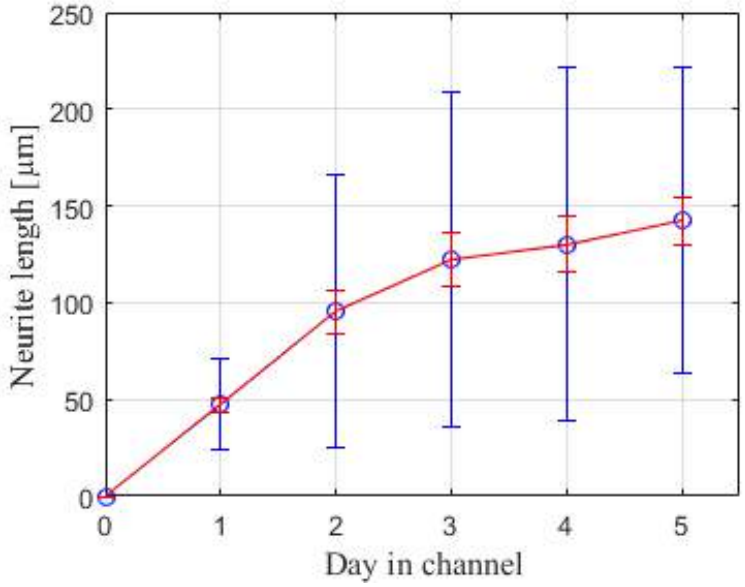

FIGURE 5.11: Neurite length within the microchannels over the course of 5 days. The blue error bars are the standard deviation and the red error bars are the standard error of mean (n = 40).

Figure 5.11 shows the neurite length inside of the microchannels over the course of 5 days. Standard deviation and standard error of the mean are indicated by blue and red error bars, respectively. It can be seen that the average neurite progression slows down over time. This could be partially explained by deflection or a restricted supply of nutrients near the narrow region of the microchannels.

The data in Figure 5.11 exhibit a large variance which is caused by the heterogeneous progression and retraction of individual neurons, leading to a broad distribution of neurite lengths in the microchannels. This behavior is reflected in Figure 5.12, which shows a histogram of the daily extension and retraction of the individual neurites. A rather broad distribution with a maximum neurite extension in the range of 200 µm per day was observed.

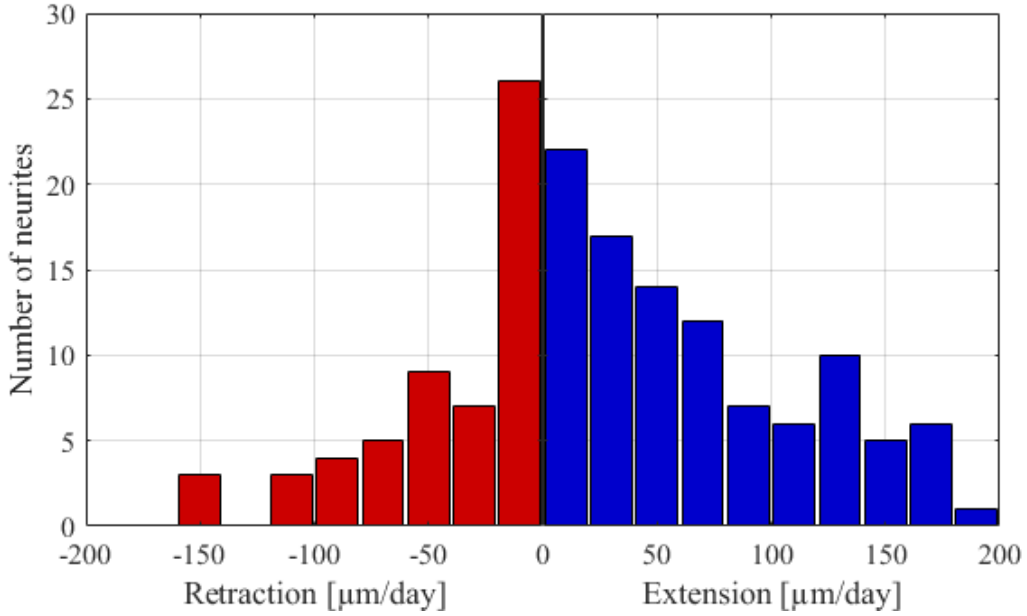

FIGURE 5.12: Distribution of neurite extension and retraction length per day. Forty neurites within the microfluidic guiding channels have been investigated over the time course of 5 days.

5.5 CONCLUSION AND OUTLOOK

In summary, a microfluidic platform with an asymmetric geometry for neurite outgrowth based on selective etching of LOR30B sacrificial layer structures has been developed. An array of individually addressable microwires for localized thermal stimulation are integrated into the microfluidic system. The new fabrication method combines microwire arrays and SU-8 microchannels on one chip in a straighforward fabrication approach. It therefore eliminates alignment issues of PDMS-bonded microfluidic structures on devices with functional structures. Additionally, problems of delaminating microfluidic structures from the chip surface can be avoided. The outgrowth of neurites from PC12 cells within the microchannel structures have been demonstrated.

This approach will be useful for future studies on functional neural networks, in particular, the investigations into the impact of temperature on neurite growth or thermal axotomy and regeneration studies.

CHAPTER 6

CONCLUSIONS AND OUTLOOK

6.1 SUMMARY OF THE THESIS

The main findings of this thesis are as follows: first, the signal propagation in cardiac cells can be controlled using localized heating. Second, the growth rate and direction of neurite outgrowth are determined by temperature gradients. Third, the combination of microwire arrays and microchannels for investigating the effects of temperature gradients on neuronal guidance is introduced in this work. The summary of the thesis is presented below.

The thesis descibes an approach using microwire arrays to study the effects of local heating on cellular behavior. The fabrication of thin microwires on a chip enabled highly localized temperature gradients to be generated, which was used efficiently for studies of thermal stimulation on cellular networks. In comparison to local heating induced from nanoparticles and lasers, the heating stimulation of microwire array chips has many advantages because the method is not only non-toxic but also a practical set-up for cellular experiments.

The microwire array chips have been demonstrated to be useful tools for applying microscopic heating to regulate calcium signal propagation in cardiomyocyte-like HL1 cells. In particular, the velocity of calcium signal propagation was locally increased as a result of heat stimulation. Furthermore, the localized heating resulted in the disturbance of the calcium wavefront over the heated region. The calcium signals shifted into the heated area is evidence for the activation of pacemaker cells using thermal stimulation.

Additionally, the microwire array chips have shown to be practical devices for investigating the effects of temperature gradients on neuronal development and growing directions. The temperature gradient has been considered as a guidance cue for neurite outgrowth. A rapid rise in temperature causes an increase in the growth rate of neuronal cells. This finding provides an alternative approach to the studies of neuronal formation using heat stimulation.

The combination of microheaters and an array of asymmetrical microchannels fabricated on the chip's surface has been introduced to investigate the effects of temperature gradients on neurite outgrowth inside microchannels. The fabrication of microchannels enables researchers to separate and control the polarity of neuronal networks. The experiment with neurites from PC12 cells has demonstrated that neurites can grow from the inlet to the outlet of these channels. In addition, the fabrication of SU-8 microchannels using the photoresist sacrificial layer has shown to be more beneficial than the conventional approach using chromium in terms of reducing the number of steps for photolithography and enhancing the thickness of channel structures up to a few micron. The fabrication of perpendicular microchannels integrated into microwire arrays serves as a novel approach for studying the impact of temperature gradients on certain parts of neurons, either cellular bodies or neurites.

Overall, this thesis has demonstrated that heat can be used to manipulate the calcium signal propagation in cardiac networks. The changes of calcium wave upon local heat stimulation provide possible applications including cells analysis (e.g. pacemaker interference or induced pacemaker switching) and medical applications such as defibrillator triggered by heat. Moreover, temperature gradients have been shown as signaling cues to accelerate the speed of neurite outgrowth and guiding neurites. This work provides preliminary indications for studies in neuronal regeneration. As such, the investigation of changes in the intracellular reaction kinetics can be conducted in the future.

6.2 OUTLOOK

Microwire array chips show great potential for on-chip localized heating stimulation. The microwire array chips could be applied as an efficient tool to generate a microscopic lesion on neuronal networks. This performance can be useful for the study of regeneration of axonal connections after injury. In order to assess the ability of microwire arrays to separate neuronal networks using localized heating, we performed

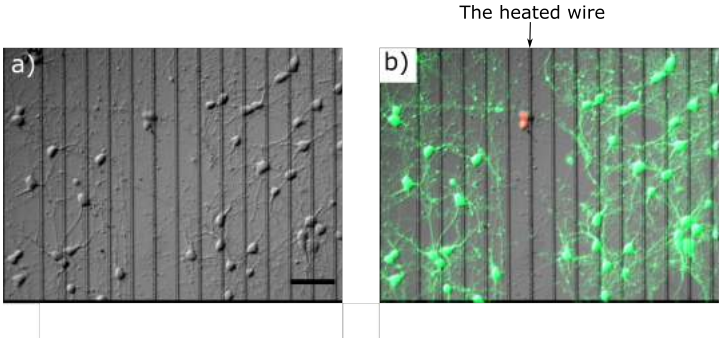

FIGURE 6.1: a) Rat cortical neurons growing on microwire array chips. b) Live/dead staining of a sample subjected to a lesion on an individual wire. The red fluorescence (indicating cell death) is restricted to the region directly on the heated wire. The green fluorescence indicating live cells exhibits throughout the remaining part of the image. The scale bar corresponds to 60 µm.

the experiment with rat cortical neurons cultured on the microwire array chip as shown in Figure 6.1a. A fluorescent staining of heat-activated neurons was employed to visualize live and dead cells (Figure 6.1b). The red fluorescent is limited to a vertical line of the heated wire, while the green fluorescence exhibits throughout the remaining image. This indicates that the cell death is restricted to a region directly on the heated wire while the cells in the vicinity of the heated wire remain alive. This preliminary result demonstrates that neuronal networks can be successfully dissected using microscopic heating induced on an individual wire. Further experiments could investigate underlying mechanisms of axonal connections, such as molecules involved in the regeneration process.

The second interesting research field of localized heating is the application of microwire arrays in studying the effects of heating on dopamine release. Dopamine is a catecholamine neurotransmitter which plays an important role in physiological functions. Any disorders in the neurotransmission of dopamine can cause neurological diseases such as Parkinsons disease. Many studies have been proposed to regulate dopamine release, either through chemical inhibition or electrical stimulation [135–137]. Recently, the research of Cheng *et al.* [138] indicated that dopaminergic release also depends on thermal stimulation. To record the dopamine release, microelectrodes can be integrated into microwire array chips. Fig-

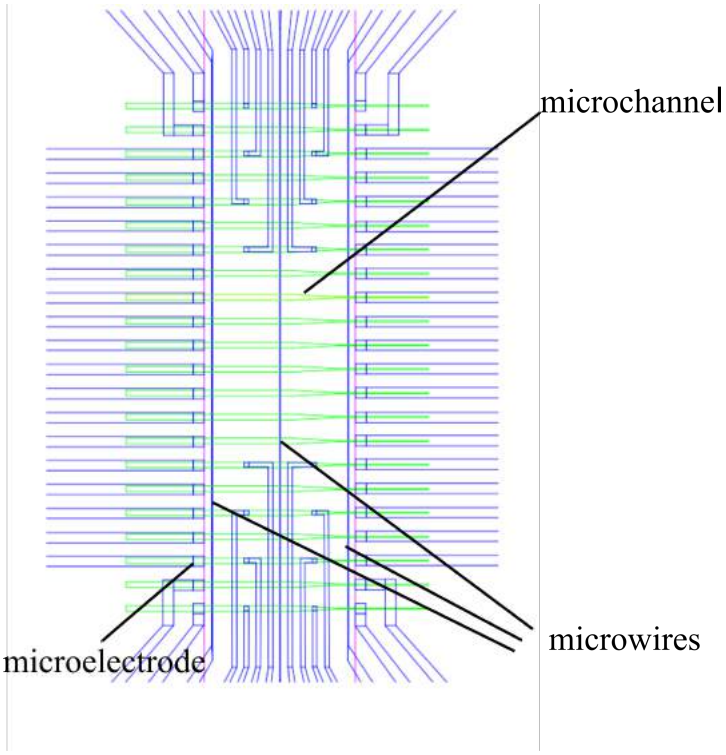

FIGURE 6.2: The outline of a chip integrated microwire arrays, microchannels and microelectrodes. Localized heating on the chip can be used to study the dopamine released from PC12 cells.

ure 6.2 shows a schematic of the microwire and microelectrode arrays combined with microchannels for neuronal guidance. Integrating microelectrode arrays into the chip could allow the recording of the dopamine release from neurons during the heat stimulation of neurons growing inside microchannels.

The study of the influence of temperature gradients on the directionality of cell migration is another promising application of microwire array chips. Directional cell migration is crucial to many physiological processes such as embryogenesis, tissue formation, immune response, and wound healing [139]. Recently, fibroblast cells have been shown to be a model for cell migration studies due to their ability to synthesize the extracellular matrix and collagen, which is essential in wound healing [140]. The locomotion of fibroblasts is driven by a variety of external stimuli either chemical signals or electrical stimulation [141–143]. Furthermore,

the study of Parkinson [144] demonstrates that the motility of fibroblast cells also responds to thermal stimulation. In this context, the microwire array chips can be utilized to generate temperature gradients to study the moving direction of fibroblast cells in response of heat stimulation. This study proposes an approach in manipulating tissue growth within the stimulation of temperature gradients.

APPENDIX A

GEOMETRY AND PARAMETERS FOR TEMPERATURE SIMULATION

Figure 3.2, Figure 4.10b, and Figure 4.11

The height of microwire = 300 nm
The width of microwire = 2.5 µm
The height of silicon dioxide = 1 µm
The width of silicon substrate = 6 mm
The height of substrate = 500 µm
The height of polyimide = 1 µm
The height of water = 2 mm
The height of aluminum holder = 2 mm
Heat source for the power of 0.7 W = 1.8436×10^4 W m^{-3}
Heat source for the power of 1 W = 2.6337×10^4 W m^{-3}

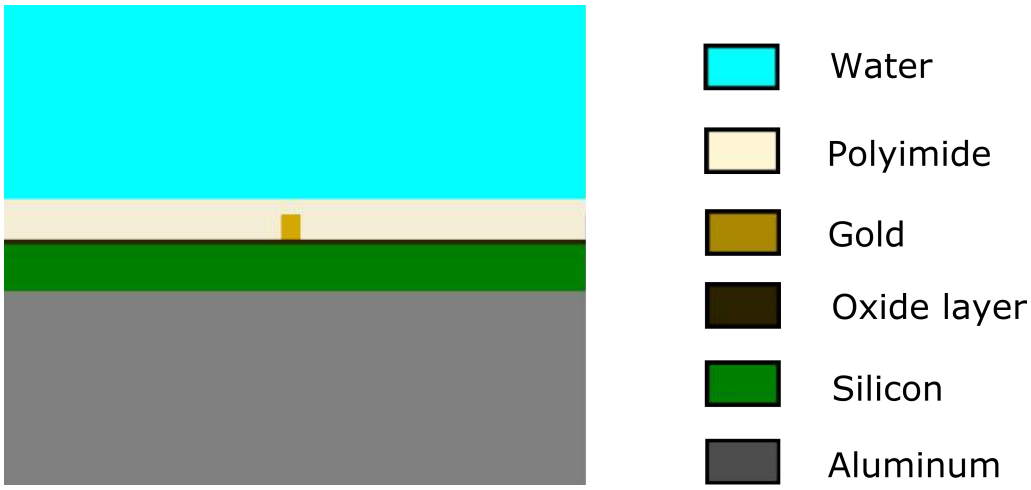

FIGURE A.1: The geometry for temperature simulation.

APPENDIX B

PROTOCOL FOR BONDING PDMS TO A POLYIMIDE SURFACE

MATERIALS

- PDMS (10:1)
- Polyimide chips
- MPTMS (3-mercaptopropyl trimethoxysilane) 1 % in methanol
- GPTMS (3-glycidyloxypropyl trimethoxysilane) 1 % in methanol
- oxygen plasma
- Mili-Q water (or distilled water)

PROCEDURE

1. Rinse PDMS structures using isopropanol and then clean in an ultrasound bath with mili-Q water for 15 min.

2. Rinse chips with isopropanol and subsequently with mili-Q water in an ultrasound bath for 15 min.

3. Put the chips and the PDMS in oxygen plasma chamber (80 mW, 0.8 mbar, 20 min).

4. Immerse the PDMS and the chips in MPTMS and GPTMS, respectively for 1 h under a fume hood.

5. Then, rinse the PDMS and chips with mili-Q water. After that, dry with pressure air.

6. Use a fineplacer device to align the PDMS structures on the microwire chips.

7. In order to form a permanent bonding between PDMS and chip, the PDMS and chips are left overnight at room temperature under pressure of 30 kPa. To remain a hydrophilic environment inside the PDMS microchannel, 50 µL of mili-Q water is pipetted into one reservoir of each side.

APPENDIX C

PROTOCOL FOR HL-1 CELL CULTURE

MEDIUM FOR HL-1 CELL

- Claycomb Medium 100 mL
- Fetal bovine serum (FBS) 11.2 mL
- Penicillin/Streptomycin 1.14 mL
- Norepinephrine 1.14 mL
- L-Glutamine (200 mM stock) 1.14 mL

THAWING AND PLATING HL-1 CELLS

1. HL-1 cells are stored in a frozen state in a cryotube containing a complete medium supplemented with 5 % DMSO in liquid nitrogen.

2. Prepare a sterile falcon tube with 10 mL of warm complete medium (37 °C) .

3. Thaw the cryotube containing HL-1 cells at 37 °C in a water bath. This step should be done quickly to diminish the toxicity of DMSO. If the cells are not completely thawed, add warm medium to cryotube and remove thawed solution immediately. Repeat until empty.

4. Add the thawed content of the cryotube to the 10 mL of complete medium (the prepared falcon).

5. Mix well and centrifuge the cells at 1700 rpm for 5 min at room temperature.

6. Remove the supernatant (containing DMSO) and add 1 mL of fresh complete medium to resuspend the cell pellet.

7. Mix well by trituration in a pipette and plate the contents in the flask. Then add 5 mL of medium into the flask.

8. When the cells reach a high confluency, passage the cell using the standard sub-culturing technique.

FEEDING

- Feed the cells every day. On Friday leave the cells until Monday with 10 mL of medium
- Warm up medium in water bath at 37 °C for 5–10 min before feeding the cells.
- Aspirate a whole medium inside the flask gently using serological pipette (5 mL).
- Add 5 mL of fresh medium to the flask.

PASSAGING

- When the cells are confluent, they are ready to passage.
- Warm up the trypsin EDTA at 37 °C in a warm bath.
- Rinse the cell in the flask with 1 mL of trypsin EDTA, then aspirate the trypsin out.
- Add another 1 mL of trypsin EDTA and transfer into the incubator at 37 °C, 5 % CO_2 for approximately 4–5 min.
- Add 5 mL of cell culture medium into the dish and carefully washing the cells and transfer entirely the cells into falcon tube.
- Centrifuge at 1700 rpm for 5 min.
- Aspirate the supernatant in the falcon tube and add 1 mL of medium to resuspend

- Pipette the cell suspension into the T25 flask follow the formula:

$$\frac{1}{2^{n-1}}$$

  This is the resuspended percentage of the concentrated cell solution, n is the number of days after which the cells should reach a confluence level.
- Shake the flask gently for the cells spread on the surface of flask.
- Add 5 mL of cell culture medium into the flask and transfer to the incubator.

FREEZING

1. Prepare freezing medium: Growth medium supplemented with 5 % of DMSO. Use a 0.22 µm filter to sterile DMSO before adding to medium, prepare 9.5 mL + 500 µL of DMSO.
2. Prepare 9 flasks with 90 % of cell confluence for aliquot.
3. Rinse the cell with 1 mL of trypsin.
4. Pipette away and add another 1 mL of trypsin and put the cells in the incubator about 4–5 min.
5. Add 5 mL of the medium into the flask, carefully wash the cells, and transfer all the cells from 9 flasks into a falcon tube (50 mL).
6. Centrifuge at 1700 rpm for 5 min.
7. Aspirate the supernatant in the falcon tube and add 2 mL of freezing medium to resuspend.
8. Add the rest of prepared medium to the falcon tube and pipette 1 mL of cell suspension in each cryotube.
9. Put the cryotubes into a pre-cooled (4 °C) chamber and store at −80 °C for 24 h and then transfer all of them to the liquid nitrogen.

APPENDIX D

PROTOCOL FOR PC12 CELL CULTURE

PREPARE COLLAGEN IV

- Dilution collagen IV 5 mg in DPBS +/+ and split to different concentration for coating:
- 120 µg mL^{-1} collagen IV for culture dishes
- 60 µg mL^{-1} collagen IV for differentiation dishes
- 30 µg mL^{-1} collagen IV for chips
- In order to make collagen IV with a concentration of 120 µg mL^{-1}, 5 mg of collagen IV is diluted into 42 mL of DPBS +/+. To have an appropriate concentration of collagen for differentiation medium and chips, this solution is then diluted into DPBS +/+ again.
- Aliquot 1000 µL of collagen IV into each Eppendorf.
- Store them at $-20\,^{\circ}$C.

PREPARE NGF 50 µg mL^{-1} (1000X)

- Centrifuge the vial before opening. Avoid freeze-thaw cycles.
- Sterilize DPBS +/+ using 0.2 µm filter
- Dissolve 20 µg of NGF into 400 µL DPBS +/+
- Aliquot 3 µL into each Eppendorf
- Store at $-20\,^{\circ}$C

PROLIFERATION MEDIUM (INGREDIENT FOR 50 mL)

- RPMI 1640 41.75 mL
- L-Glutamine (Stock 200mM) 0.5 mL
- Horse serum 5 mL
- Fetal Bovine Serum (FBS) 2.5 mL
- Penicillin Streptomycin (Penstrep) 0.25 mL

INGREDIENTS FOR 50 mL DIFFERENTIATION MEDIUM

- RPMI 1640 49.25 mL
- Horse serum 0.5 mL
- Penstrep 0.25 mL
- Add NGF 50 ng/mL to the medium before each feeding

COATING DISHES WITH COLAGEN IV ($120\,\mu g\,mL^{-1}$)

- Coat 1000 µL collagen IV into a Petri-dish
- Keep the coated dishes overnight in the fridge at 4 °C
- Rinse the coated dished by washing first with DPBS +/+ and then with 1 mL of RPMI 1640 before seeding the cells

THAWING AND PLATING PC12 CELLS

1. PC12 cells are stored in a frozen state in a complete medium supplemented with 5% DMSO in liquid nitrogen.

2. Prepare a sterile Falcon tube with 10 mL of warm (37 °C) complete medium.

3. Thaw the cryotube at 37 °C in a water bath. This step should be done quickly to diminish the toxicity of DMSO. If the cells are not completely thawed, add warm medium into cryotube and remove thawed solution immediately.

4. Add the thawed content of the cryotube into the 10 mL of complete medium.

5. Mix well and centrifuge the cells at 1200 rpm for 4 min 30 second at room temperature.

6. Remove the supernatant (containing DMSO) and add 10 mL of fresh complete medium to resuspend the cell pellet.

7. Mix well by trituration and pipette the contents into a coated Petri-dish. This steps also help to break up cell clumps.

8. Shake the plate well, back and forth and left to right, to spread the cells uniformly. Avoid shaking circularly otherwise the cells will tend to concentrate at the center of the plate.

FEEDING

- Feed the cells every second day. On Friday leave the cells until Monday with 12 mL of medium
- Prepare differentiation medium with NGF (1 µL mL^{-1}) in medium and warm up medium in 37 °C right before feeding the cells.
- Replace about half of the proliferation medium (remove 5 mL).
- Replace about half of the differentiation medium (remove 5 mL).

SPLITTING

- Cells should be split above 90 % confluence. Should be kept at as high confluence percentage as possible all the time.
- Warm up the trypsin at 37 °C in the warm bath.
- Prepare differentiation medium with NGF stock solution in medium, the concentration of NGF is 1 µL mL^{-1} (5 µL NGF in 5 mL replaced medium)
- Add 3 mL of trypsin and put in the incubator for 1 min
- Pipette away and add another 3 mL of trypsin and put in the incubator about 6 min.
- Add 7 mL of proliferation medium in the dish and carefully washing cell, get all the cells, then pipette into falcon tube.
- Centrifuge at 1200 rpm for 4 min 30 s.
- Aspirate the supernatant in the falcon tube and add 1 mL of medium to resuspend.

- Pipette the cell suspension into the Petri-dish follow ratio: 1/4 (250 µL) in proliferation dish and 1/10 (100 µL) to 1/50 (20 µL) for differentiation. This step can be done by counting the number of cells in the disk and decide how many cells need to pipette.

FREEZING

- Prepare freezing medium: Growth medium supplemented with 5 % DMSO. Use 0.22 µm to sterile DMSO before adding to the medium, prepare 9.5 mL + 500 µL of DMSO.
- Prepare 9 dishes with 90 % cell confluence for aliquot.
- Add 2 mL of trypsin and put in the incubator for 1 min.
- Pipette away and add another 2 mL of trypsin and put in the incubator about 6 min.
- Add 3 mL of proliferation medium in the dish and carefully washing cell and get all the cells, then pipette all the cells from 9 dishes into falcon tube (50 mL).
- Centrifuge at 1200 rpm in 4 min 30 s.
- Aspirate the supernatant in the falcon tube and add 2 mL of freezing medium to resuspend.
- Add the rest of prepared medium to the falcon tube and pipette 1 mL of cell suspension in each cryotube.
- Put the cryotubes into a pre-cooled (4 °C) chamber and store at −80 °C for 24 h and then transfer all of them to the liquid nitrogen.

APPENDIX E

PROTOCOL FOR PREPARING DYES

E.1 FLUO-4

- Filter DMSO using 0.22 µm filter
- Dilute 45.6 µL of DMSO into 50 µg of Fluo-4 to get a concentration of 1 mM, then pipette 5 µL of Fluo-4 into each Eppendorf tube.

E.2 CALCEIN-AM/ETHIDIUM HOMODIMER(ETHD)

- Filter DMSO using 0.22 µm filter
- Dilute 251 µL of DMSO into 1 mg of Calcein-AM to get a concentration of 4 mM, then pipette 2 µL of Calcein-AM into each Eppendorf tube.
- Dilute EthD into 171 µL of DMSO and 467 µL of Mili-Q water in 1 mg of ethD, then pipette 2 µL of EthD into each Eppendorf tube.

E.3 CELLTRACKER GREEN

- Put the vial at room temperature 15 min before opening.
- Dissolve CellTracke Green into DMSO to get a final concentration of 10 mM (1 mg CellTracker Green in 215 µL DMSO).

- To stain PC12 cells, prepare 1000 µL of RPMI serum free, then add 1 µL of CellTracker Green into 1000 µL of RPMI serum free for staining the cells.

BIBLIOGRAPHY

[1] Azambuja, R. M., Kraemer, D. C. & Westhusin, M. E. Effect of low temperatures on in-vitro matured bovine oocytes. *Theriogenology* **49**, 1155–1164 (1998).

[2] Vergara, M. *et al.* Differential effect of culture temperature and specific growth rate on CHO cell behavior in chemostat culture. *PLoS ONE* **9**, 1–6 (2014).

[3] Burrows, E. D. M. U. N. D. H. & Ch, B. Department of Radiology , University of Rochester Medical Centre , Rochester , New York , U . S . A . 309–323 (1967).

[4] S.H. Kang, A. Carl, J.M.McHugh, H. G. & Kenyon, J. Roles of mitochondria and temperature in the control of intracellular calcium in adult rat sensory neurons. *Cell calcium* **43**, 388–404 (2009). NIHMS150003.

[5] Rashid, H. *et al.* Temperature during pregnancy influences the fetal growth and birth size. *Tropical Medicine and Health* **45**, 1–9 (2016).

[6] Keil, G., Cummings, E. & de Magalhães, J. P. Being cool: how body temperature influences ageing and longevity. *Biogerontology* **16**, 383–397 (2015).

[7] Robert N.Butler, C.-C. *et al.* Aging In Today ' s Environment (1987).

[8] Sengupta, P. & Garrity, P. Sensing temperature. *Current Biology* **23**, R304–R307 (2013). URL http://dx.doi.org/10.1016/j.cub.2013.03.009. NIHMS150003.

[9] Calaban, M. J. & Makarewicz, J. C. The effect of temperature and density on the amplitude of vertical migration of vertical Daphnia magna. *Limnololgy and Oceanography* **27**, 262–271 (1982).

[10] Demir, M. & Salman, H. Bacterial thermotaxis by speed modulation. *Biophysical Journal* **103**, 1683–1690 (2012). URL http://dx.doi.org/10.1016/j.bpj.2012.09.005.

[11] Paulick, A. *et al.* Mechanism of bidirectional thermotaxis in Escherichia coli. *eLife* **6** (2017).

[12] Ryu, W. S. & Samuel, A. D. T. Thermotaxis in Caenorhabditis elegans Analyzed by Measuring Responses to Defined Thermal Stimuli **22**, 5727–5733 (2002).

[13] Whitesides, G. M. The origins and the future of microfluidics. *Nature* **442**, 368–373 (2006). arXiv:1011.1669v3.

[14] Online, V. A. *et al.* Labs-on-a-Chip: origin, highlights and future perspectives : On the occasion of the 10th μTAS conference. *Lab Chip* **6**, 1266–1273 (2006). URL http://xlink.rsc.org/?DOI=B612120A.

[15] Dittrich, P. S. & Manz, A. Lab-on-a-chip: Microfluidics in drug discovery. *Nature Reviews Drug Discovery* **5**, 210–218 (2006).

[16] Croushore, C. A. & Sweedler, J. V. Microfluidic systems for studying neurotransmitters and neurotransmission. *Lab on a chip* **13**, 1666–76 (2013). URL http://pubs.rsc.org/en/content/articlehtml/2013/lc/c3lc41334a.

[17] Simmons, C. S., Petzold, B. C. & Pruitt, B. L. Microsystems for biomimetic stimulation of cardiac cells. *Lab on a Chip* **12**, 3235 (2012).

[18] Kothapalli, C. R. *et al.* A high-throughput microfluidic assay to study neurite response to growth factor gradients. *Lab on a Chip* **11**, 497–507 (2011).

[19] El-Ali, J., Sorger, P. K. & Jensen, K. F. Cells on chips. *Nature* **442**, 403–411 (2006).

[20] Jain, A., Ness, K. & Goodson, K. E. Theoretical and experimental investigation of spatial temperature gradient effects on cells using a microfabricated microheater platform. *Sensors and Actuators, B: Chemical* **143**, 286–294 (2009).

[21] Kramer, L. M. J. & Scott, J. K. *What are cells?*, 1–21 (Macmillan Education UK, London, 1979). URL https://doi.org/10.1007/978-1-349-03989-0_1.

[22] Walters, B. A. A. J. J. L. M. R. K. R. P. *Molecular Biology of the cell* (2008), garland sc edn.

[23] Schaefer, A. W. *et al.* Coordination of Actin Filament and Microtubule Dynamics during Neurite Outgrowth. *Developmental Cell* **15**, 146–162 (2008).

[24] Iain D. Campbell. *Biophysical Techniques* (Oxford University Press Inc., New York, 2012).

[25] Venetucci, L. & Garratt, C. J. Cardiac channelopathies. *Medicine (United Kingdom)* **42**, 591–594 (2014).

[26] Hudspeth, E. R. J. H. S. T. M. J. S. A. S. A. *Principles of Neural science* (2013).

[27] Paul A. Iaizzo. *Handbook of Cardiac Anatomy, Physiology, and Devices* (2005).

[28] White, S. M., Constantin, P. E. & Claycomb, W. C. Cardiac physiology at the cellular level: use of cultured HL-1 cardiomyocytes for studies of cardiac muscle cell structure and function. *American journal of physiology. Heart and circulatory physiology* **286**, H823–H829 (2004).

[29] F.Santoro. *3D nanoelectrodes for bioelectronics: design and characterization of the cell-electrode interface*. Ph.D. thesis (2014).

[30] Maybeck, V. *et al.* Boron-doped nanocrystalline diamond microelectrode arrays monitor cardiac action potentials. *Advanced Healthcare Materials* **3**, 283–289 (2014).

[31] Wikipedia. Gap junction — wikipedia, the free encyclopedia (2017). URL https://en.wikipedia.org/w/index.php?title=Gap_junction&oldid=776300120. [Online; accessed 19-August-2017].

[32] Bers, D. M. & Despa, S. Cardiac Excitation-Contraction Coupling. *Encyclopedia of Biological Chemistry: Second Edition* **415**, 379–383 (2013).

[33] Pfeiffer, E. R., Tangney, J. R., Omens, J. H. & McCulloch, A. D. Biomechanics of cardiac electromechanical coupling and mechanoelectric feedback. *Journal of biomechanical engineering* **136**, 021007 (2014). URL http://www.ncbi.nlm.nih.gov/pubmed/24337452. PMC4023651.

[34] Dhaka, A., Viswanath, V. & Patapoutian, A. Trp Ion Channels and Temperature Sensation. *Annual Review of Neuroscience* **29**, 135–161 (2006). URL http://www.annualreviews.org/doi/abs/10.1146/annurev.neuro.29.051605.112958.

[35] Feng, Q. *Temperature Sensing byThermal TRP Channels. Thermodynamic Basis andMolecular Insights.*, vol. 74 (Elsevier, 2014). URL http://dx.doi.org/10.1016/B978-0-12-800181-3.00002-6.

[36] Nilius, B. Sensing with TRP channels: how irritant! **1**, 85–93 (2005).

[37] Patapoutian, A., Peier, A. M., Story, G. M. & Viswanath, V. ThermoTRP channels and beyond: mechanisms of temperature sensation. *Nature reviews. Neuroscience* **4**, 529–539 (2003).

[38] Benham, C. D., Gunthorpe, M. J. & Davis, J. B. TRPV channels as temperature sensors. *Cell Calcium* **33**, 479–487 (2003).

[39] Claycomb, W. C. *et al.* HL-1 cells: a cardiac muscle cell line that contracts and retains phenotypic characteristics of the adult cardiomyocyte. *Proc Natl Acad Sci U S A* **95**, 2979–2984 (1998).

[40] Sartiani, L., Bochet, P., Cerbai, E., Mugelli, A. & Fischmeister, R. Functional expression of the hyperpolarization-activated, non-selective cation current I(f) in immortalized HL-1 cardiomyocytes. *The Journal of physiology* **545**, 81–92 (2002). URL http://www.ncbi.nlm.nih.gov/pubmed/12433951{%}5Cnhttp://www.pubmedcentral.nih.gov/articlerender.fcgi?artid=PMC2290645.

[41] Greene, L. a. & Tischler, a. S. Establishment of a noradrenergic clonal line of rat adrenal pheochromocytoma cells which respond to nerve growth factor. *Proceedings of the National Academy of Sciences of the United States of America* **73**, 2424–2428 (1976).

[42] Drubin, D. G., Feinstein, S. C., Shooter, E. M. & Kirschner, M. W. Nerve growth factor-induced neurite outgrowth in PC12 cells involves the coordinate induction of microtubule assembly and assembly-promoting factors. *Journal of Cell Biology* **101**, 1799–1807 (1985).

[43] Das, K. P., Freudenrich, T. M. & Mundy, W. R. Assessment of PC12 cell differentiation and neurite growth: A comparison of morphological and neurochemical measures. *Neurotoxicology and Teratology* **26**, 397–406 (2004).

[44] Mingorance-Le-Meur, A., Mohebiany, A. N. & O'Connor, T. P. Varicones and growth cones: Two neurite terminals in PC12 cells. *PLoS ONE* **4** (2009).

[45] Bentley, D. & O'Connor, T. P. Cytoskeletal events in growth cone steering (1994).

[46] Teng, K. K., Angelastro, J. M., Cunningham, M. E. & Greene, L. A. Cultured PC12 cells: A model for neuronal function, differentiation, and survival. *Cell Biology, Four-Volume Set* **1**, 171–176 (2006).

[47] Varnum-Finney, B. & Reichardt, L. F. Vinculin-deficient PC12 cell lines extend unstable lamellipodia and filopodia and have a reduced rate of neurite outgrowth. *Journal of Cell Biology* **127**, 1071–1084 (1994).

[48] Li, X. & Li, P. C. H. Microfluidic selection and retention of a single cardiac myocyte, on-chip dye loading, cell contraction by chemical stimulation, and quantitative fluorescent analysis of intracellular calcium. *Analytical Chemistry* **77**, 4315–4322 (2005).

[49] Dinh, N.-D. *et al.* Microfluidic construction of minimalistic neuronal co-cultures. *Lab on a Chip* **13**, 1402 (2013). URL http://xlink.rsc.org/?DOI=c3lc41224e.

[50] Renault, R., Durand, J.-B., Viovy, J.-L. & Villard, C. Asymmetric axonal edge guidance : a new paradigm for building oriented neuronal networks. *Lab Chip* **16**, 2188–2191 (2016). URL http://pubs.rsc.org/en/Content/ArticleLanding/2016/LC/C6LC00479B.

[51] Taylor, A. M., Rhee, S. W., Tu, C. H., Cribbs, D. H. & Cotman, C. W. Microfluidic Multicompartment Device for Neuroscience Research. *Langmuir* **19**, 1551–1556 (2003).

[52] Taylor, A. M. *et al.* A microfluidic culture platform for CNS axonal injury, regeneration and transport. *Nature methods* **2**, 599–605 (2005). URL http://www.ncbi.nlm.nih.gov/pubmed/16094385{%}5Cnhttp://www.pubmedcentral.nih.gov/articlerender.fcgi?artid=PMC1558906.

[53] Taylor, A. M. & Jeon, N. L. Micro-scale and microfluidic devices for neurobiology. *Current Opinion in Neurobiology* **20**, 640–647 (2010). URL http://dx.doi.org/10.1016/j.conb.2010.07.011.

[54] Peyrin, J.-M. *et al.* Axon diodes for the reconstruction of oriented neuronal networks in microfluidic chambers. *Lab on a chip* **11**, 3663–73 (2011). URL http://www.ncbi.nlm.nih.gov/pubmed/21922081.

[55] Tan, S. H., Nguyen, N. T., Chua, Y. C. & Kang, T. G. Oxygen plasma treatment for reducing hydrophobicity of a sealed polydimethylsiloxane microchannel. *Biomicrofluidics* **4**, 1–8 (2010).

[56] Toepke, M. W. & Beebe, D. J. PDMS absorption of small molecules and consequences in microfluidic applications. *Lab on a chip* **6**, 1484–1486 (2006).

[57] Marc J. Madou. *Fundamentals of microfabrication and nanotechnology* (CRC Press Taylor & Francis Group, 2011).

[58] Cui, Z. & Lawes, R. a. A new sacrificial layer process for the fabrication of micromechanical systems. *Journal of Micromechanics and Microengineering* **7**, 128–130 (1999).

[59] Cavaliere, F., Sciarra, M., Crea, M. a., Rossi, M. & Proietti, R. Fundamentals in Physics. *Recenti progressi in medicina* **76**, 563–566 (1985).

[60] Theodore L. Bergman, Adrienne S. Lavine, Frank P. Incropera, D. P. D. *Introduction to heat transfer* (John Wiley & Sons, 2011).

[61] Takahashi, A., Camacho, P., Lechleiter, J. D. & Herman, B. Measurement of intracellular calcium. *Physiological Reviews* **79**, 1089–1125 (1999). URL http://eutils.ncbi.nlm.nih.gov/entrez/eutils/elink.fcgi?dbfrom=pubmed{&}id=10508230{&}retmode=ref{&}cmd=prlinks{%}5Cnpapers3://publication/uuid/EBF04136-C892-4553-989F-6C2EC343612A.

[62] Becker, W. Fluorescence lifetime imaging - techniques and applications. *Journal of Microscopy* **247**, 119–136 (2012).

[63] van Munster, E. & Gadella, T. Fluorescence lifetime imaging microscopy (FLIM). *Adv Biochem Engin/Biotechnol* **95**,

143–175 (2005). URL http://www.springerlink.com/index/U91Y09TM3KVDVEVW.pdf.

[64] Paviolo, C., Clayton, A. H. A., Mcarthur, S. L. & Stoddart, P. R. Temperature measurement in the microscopic regime: A comparison between fluorescence lifetime- and intensity-based methods. *Journal of Microscopy* **250**, 179–188 (2013).

[65] Wilson, T. E. & Crandall, C. G. Effect of thermal stress on cardiac function. *Exercise and sport sciences reviews* **39**, 12–17 (2011).

[66] Bers, D. M. Calcium Fluxes Involved in Control of Cardiac Myocyte Contraction. *Journal of the American Heart Association* **87**, 275–281 (2000). URL http://circres.ahajournals.org/cgi/doi/10.1161/01.RES.87.4.275.

[67] Cheng, H., Lederer, M. R., Lederer, W. J. & Cannell, M. B. Calcium sparks and [Ca 2+] i waves in cardiac myocytes. *American Journal of Physiology - Cell Physiology* **270**, C148–C159 (1996). URL http://ajpcell.physiology.org/cgi/content/abstract/270/1/C148{%}5Cnhttp://ajpcell.physiology.org/cgi/reprint/270/1/C148.pdf.

[68] Cheng-han Lee, Damon Poburko, Kuo-Hsing Kuo, C. Y. S. Calcium oscillations, gradients, and homeostasis in vascular smooth muscle. *Am J Physiol Heart Circ Physiol 282* **282**, H1571 – H1583 (2002).

[69] Fearnley, C. J., Llewelyn Roderick, H. & Bootman, M. D. Calcium signaling in cardiac myocytes. *Cold Spring Harbor Perspectives in Biology* **3**, 1–20 (2011).

[70] Iftinca, M. *et al.* Temperature dependence of T-type calcium channel gating. *Neuroscience* **142**, 1031–1042 (2006).

[71] Lanner, J. T., Georgiou, D. K., Joshi, A. D. & Hamilton, S. L. Ryanodine receptors: structure, expression, molecular details, and function in calcium release. *Cold Spring Harbor perspectives in biology* **2**, 1–21 (2010). NIHMS150003.

[72] Vale, M. G. & Carvalho, A. P. Effect of temperature on the reversal of the calcium ion pump in sarcoplasmic reticulum. *The Biochemical journal* **186**, 461–7 (1980). URL http://www.pubmedcentral.nih.gov/articlerender.fcgi?artid=1161597{&}tool=pmcentrez{&}rendertype=abstract.

[73] Kiyonaka, S. *et al.* Genetically encoded fluorescent thermosensors visualize subcellular thermoregulation in living cells. *Nature Methods* **10**, 1232–1238 (2013).

[74] Yang, J. M., Yang, H. & Lin, L. Quantum dot nano thermometers reveal heterogeneous local thermogenesis in living cells. *ACS Nano* **5**, 5067–5071 (2011).

[75] Dickinson, G. D. & Parker, I. Temperature dependence of IP3-mediated local and global Ca2+ signals. *Biophysical journal* **104**, 386–395 (2013). URL http://www.pubmedcentral.nih.gov/articlerender.fcgi?artid=3552255{&}tool=pmcentrez{&}rendertype=abstract.

[76] Groban, L., Zapata-Sudo, G., Lin, M. & Nelson, T. E. Effects of moderate and deep hypothermia on Ca2+ signaling in rat ventricular myocytes. *Cell Physiol Biochem* **12**, 101–110 (2002). URL http://www.ncbi.nlm.nih.gov/pubmed/12077555.

[77] Han, Y.-S., Tveita, T., Prakash, Y. S. & Sieck, G. C. Mechanisms underlying hypothermia-induced cardiac contractile dysfunction. *System* **298**, 890–897 (2010).

[78] Oyama, K. *et al.* Triggering of high-speed neurite outgrowth using an optical microheater. *Scientific Reports* **5**, 16611 (2015). URL http://www.nature.com/articles/srep16611.

[79] Shanshan Liang, Fan Yang, Cheng Zhou, Yue Wang, Shao Li, C. Sun, Jose Luis Puglisi, Donald Bers, C. S. & Zheng, J. Temperature-dependent Activation of Neurons by continuos near-infrared

laser. *Cell Biochem Biophys* **53**, 33–42 (2009). URL 10.1007/s12013-008-9035-2. NIHMS150003.

[80] Shapiro, M. G., Homma, K., Villarreal, S., Richter, C.-P. & Bezanilla, F. Infrared light excites cells by changing their electrical capacitance. *Nature Communications* **3**, 736 (2012). URL http://www.pubmedcentral.nih.gov/articlerender.fcgi?artid=3316879{&}tool=pmcentrez{&}rendertype=abstract{%}5Cnhttp://www.nature.com/doifinder/10.1038/ncomms1742.

[81] E.J. Peterson and D.J. Tyler. Motor Neuron Activation in Peripheral Nerves Using Infrared Neural Stimulation. *Journal Of Neural Engineering* **11**, 016001 (2014). URL http://stacks.iop.org/1741-2552/11/i=1/a=016001. NIHMS150003.

[82] Smith, N. I. *et al.* A femtosecond laser pacemaker for heart muscle cells. *Optical Society of America, Biology and medicine* **16**, 8604–8616 (2008). URL https://doi.org/10.1364/OE.16.008604.

[83] Sweeney, S. T., Hidalgo, A., Steven de Belle, J. & Keshishian, H. Setup for functional cell ablation with lasers: Coupling of a laser to a microscope. *Cold Spring Harbor Protocols* **7**, 726–732 (2012).

[84] Ivkov, R. *et al.* Application of high amplitude alternating magnetic fields for heat induction of nanoparticles localized in cancer. *Clinical Cancer Research* **11**, 7093–7104 (2005).

[85] Pearce, J., Giustini, A., Stigliano, R. & Jack Hoopes, P. Magnetic Heating of Nanoparticles: The Importance of Particle Clustering to Achieve Therapeutic Temperatures. *Journal of nanotechnology in engineering and medicine* **4**, 11007–11–11007–14 (2013). URL http://nanoengineeringmedical.asmedigitalcollection.asme.org/article.aspx?articleid=1714583.

[86] Tseng, H.-Y., Lee, G.-B., Lee, C.-Y., Shih, Y.-H. & Lin, X.-Z. Localised heating of tumours utilising injectable magnetic nanoparticles for

hyperthermia cancer therapy. *IET nanobiotechnology / IET* **3**, 46–54 (2009).

[87] Keblinski, P., Cahill, D. G., Bodapati, A., Sullivan, C. R. & Taton, T. A. Limits of localized heating by electromagnetically excited nanoparticles. *Journal of Applied Physics* **100**, 054305 (2006).

[88] Braydich-Stolle, L., Hussain, S., Schlager, J. J. & Hofmann, M. C. In vitro cytotoxicity of nanoparticles in mammalian germline stem cells. *Toxicological Sciences* **88**, 412–419 (2005). NIHMS150003.

[89] Ballini, M. *et al.* A 1024-channel CMOS microelectrode array with 26,400 electrodes for recording and stimulation of electrogenic cells in vitro. *IEEE Journal of Solid-State Circuits* **49**, 2705–2719 (2014).

[90] Dragas, J. *et al.* In Vitro Multi-Functional Microelectrode Array Featuring 59 760 Electrodes, 2048 Electrophysiology Channels, Stimulation, Impedance Measurement, and Neurotransmitter Detection Channels. *IEEE Journal of Solid-State Circuits* **52**, 1576–1590 (2017).

[91] Heidi Au, H. T., Cui, B., Chu, Z. E., Veres, T. & Radisic, M. Cell culture chips for simultaneous application of topographical and electrical cues enhance phenotype of cardiomyocytes. *Lab on a chip* **9**, 564–575 (2009).

[92] Kujala, K. *et al.* Electrical field stimulation with a novel platform: Effect on cardiomyocyte gene expression but not on orientation. *International Journal of Biomedical Science* **8**, 109–120 (2012).

[93] Tandon, N. *et al.* Surface-patterned electrode bioreactor for electrical stimulation. *Lab on a chip* **10**, 692–700 (2010). NIHMS150003.

[94] Yakushenko, A., Kätelhön, E. & Wolfrum, B. Parallel on-chip analysis of single vesicle neurotransmitter release. *Analytical Chemistry* **85**, 5483–5490 (2013).

[95] Czeschik, A. *et al.* Nanostructured cavity devices for extracellular stimulation of HL-1 cells. *Nanoscale* **7**, 9275–81 (2015). URL http://pubs.rsc.org/en/Content/ArticleHTML/2015/NR/C5NR01690H.

[96] Reppel, M. *et al.* Microelectrode arrays: a new tool to measure embryonic heart activity. *J Electrocardiol* **37 Suppl**, 104–109 (2004).

[97] Rinklin, P., Afanasenkau, D., Wiegand, S., Offenhäusser, A. & Wolfrum, B. Inducing microscopic thermal lesions for the dissection of functional cell networks on a chip. *Lab Chip* **15**, 237–243 (2015). URL http://xlink.rsc.org/?DOI=C4LC00805G.

[98] Rinklin, P. *Microwire crossbar arrays for chemical, mechanical, and thermal stimulation of cells*, vol. 100 ISBN 9 (2014).

[99] Woodruff, M. L. *et al.* Measurement of cytoplasmic calcium concentration in the rods of wild-type and transducin knockout mice. *The Journal of physiology* **542**, 843–54 (2002). URL http://www.ncbi.nlm.nih.gov/pubmed/12154183{%}5Cnhttp://www.pubmedcentral.nih.gov/articlerender.fcgi?artid=PMC2290451.

[100] Dura, B., Kovacs, G. T. A. & Giovangrandi, L. Spatiotemporally controlled cardiac conduction block using high-frequency electrical stimulation. *PLoS ONE* **7** (2012).

[101] Giovangrandi, L., Gilchrist, K. H., Whittington, R. H. & Kovacs, G. T. A. Low-cost microelectrode array with integrated heater for extracellular recording of cardiomyocyte cultures using commercial flexible printed circuit technology. *Sensors and Actuators, B: Chemical* **113**, 545–554 (2006).

[102] Dang, K. M. *et al.* Fabrication of precisely aligned microwire and microchannel structures: Toward heat stimulation of guided neurites in neuronal cultures. *Physica Status Solidi (a)* **1600729**, 1600729 (2017). URL http://doi.wiley.com/10.1002/pssa.201600729.

[103] Dent, E. W. & Gertler, F. B. Cytoskeletal Dynamics and Review Transport in Growth Cone Motility and Axon Guidance. *Neuron* **40**, 209–227 (2003).

[104] Dent, E. W., Gupton, S. L. & Gertler, F. B. The Growth Cone Cytoskeleton in Axon Outgrowth and Guidance. *Cold Spring Harbor Perspectives in Biology* (2011).

[105] Chilton, J. K. Molecular mechanisms of axon guidance. *Dev Biol* **292**, 13–24 (2006).

[106] Henley, J. & Poo, M. M. Guiding neuronal growth cones using Ca2+ signals. *Trends in Cell Biology* **14**, 320–330 (2004).

[107] Ehrlicher, A. *et al.* Guiding neuronal growth with light. *Proceedings of the National Academy of Sciences* **99**, 16024–16028 (2002). URL http://www.pnas.org/cgi/doi/10.1073/pnas.252631899.

[108] Carnegie, D. J., Stevenson, D. J., Mazilu, M., Gunn-Moore, F. & Dholakia, K. Guided neuronal growth using optical line traps. *Opt. Express* **16**, 10507–10517 (2008). URL http://www.opticsexpress.org/abstract.cfm?URI=oe-16-14-10507.

[109] Carnegie, D. J., Cizmár, T., Baumgartl, J., Gunn-Moore, F. J. & Dholakia, K. Automated laser guidance of neuronal growth cones using a spatial light modulator. *Journal of Biophotonics* **2**, 682–692 (2009). URL http://www.ncbi.nlm.nih.gov/pubmed/19705368{%}5Cnhttp://doi.wiley.com/10.1002/jbio.200910043.

[110] Stevenson, D. J. *et al.* Optically guided neuronal growth at near infrared wavelengths. *Optics express* **14**, 9786–9793 (2006).

[111] Graves, C. E., McAllister, R. G., Rosoff, W. J. & Urbach, J. S. Optical neuronal guidance in three-dimensional matrices. *Journal of Neuroscience Methods* **179**, 278–283 (2009).

[112] Mathew, M. *et al.* Signalling effect of NIR pulsed lasers on axonal growth. *Journal of Neuroscience Methods* **186**, 196–201 (2010).

[113] Black, B. J., Gu, L. & Mohanty, S. K. Highly effective photonic cue for repulsive axonal guidance. *PLoS ONE* **9** (2014).

[114] Black, B. *et al.* Spatial temperature gradients guide axonal outgrowth. *Scientific Reports* **6**, 1–12 (2016). URL http://dx.doi.org/10.1038/srep29876.

[115] Ebbesen, C. L. & Bruus, H. Analysis of laser-induced heating in optical neuronal guidance. *Journal of Neuroscience Methods* **209**, 168–177 (2012). URL http://dx.doi.org/10.1016/j.jneumeth.2012.02.006.

[116] Sun, D., Roth, S. & Black, M. J. A quantitative analysis of current practices in optical flow estimation and the principles behind them. *International Journal of Computer Vision* **106**, 115–137 (2014).

[117] Otsu, N. A Threshold Selection Method from Gray-Level Histograms. *IEEE Transactions on Systems, Man, and Cybernetics* **9**, 62–66 (1979). URL http://ieeexplore.ieee.org/document/4310076/. arXiv:1011.1669v3.

[118] Kakugo, A., Tamura, Y., Shikinaka, K. & Yoshida, M. Formation of Well-Oriented Microtubules with Preferential 18089–18095 (2009).

[119] Niranjan, P. S. *et al.* Thermodynamic regulation of actin polymerization. *Journal of Chemical Physics* **114**, 10573–10576 (2001).

[120] Black, B. *et al.* Spatial temperature gradients guide axonal outgrowth. *Scientific Reports* **6**, 29876 (2016). URL http://www.nature.com/articles/srep29876.

[121] Furukawa, M., Enomoto, K. I., Kato, H., Ishida, T. & Maeno, T. Effects of hyperthermia on intracellular calcium concentration and responses of cancerous mammary cells in culture. *Cell Biochemistry and Function* **10**, 225–232 (1992).

[122] Zheng, J. Q. Turning of nerve growth cones induced by localized increases in intracellular calcium ions. *Nature* **403**, 89–93 (2000). URL http://www.ncbi.nlm.nih.gov/pubmed/10638759.

[123] Bradke, F., Fawcett, J. W. & Spira, M. E. Assembly of a new growth cone after axotomy: the precursor to axon regeneration. *Nature Reviews Neuroscience* **13**, 183–193 (2012). URL http://dx.doi.org/10.1038/nrn3176.

[124] Orive, G., Anitua, E., Pedraz, J. L. & Emerich, D. F. Biomaterials for promoting brain protection, repair and regeneration. *Nature reviews. Neuroscience* **10**, 682–692 (2009).

[125] Horner, P. J. & Gage, F. H. Regenerating the damaged central nervous system. *Nature* **407**, 963–970 (2000). URL http://www.ncbi.nlm.nih.gov/entrez/query.fcgi?cmd=Retrieve{&}db=PubMed{&}dopt=Citation{&}list{_}uids=11069169.

[126] Dinh, N.-D. *et al.* Microfluidic construction of minimalistic neuronal co-cultures. *Lab on a Chip* **13**, 1402 (2013). URL http://xlink.rsc.org/?DOI=c3lc41224e.

[127] Dinh, N.-D. *et al.* Preparation of neuronal co-cultures with single cell precision. *Journal of visualized experiments : JoVE* e51389 (2014). URL http://www.jove.com/video/51389/preparation-of-neuronal-co-cultures-with-single-cell-precision.

[128] Yamamoto, H. *et al.* Unidirectional signal propagation in primary neurons micropatterned at a single-cell resolution. *Applied Physics Letters* **109** (2016). URL http://dx.doi.org/10.1063/1.4959836.

[129] Ayako Yamado, Weber, C. D., Bradley, C. & Lonergan, M. C. In-mold patterning and actionable axo-somatic compartmentalization for on-chip neuron culture. *Journal of Materials Chemistry* **2**, 303 (2014). URL http://dx.doi.org/10.1039/C6LC00414H.

[130] Grau, C. M. & Greene, L. A. Use of PC12 cells and rat superior cervical ganglion sympathetic Neurons as Models for Neuroprotective Assays Relevant to Parkinson's Disease **846**, 1–10 (2012). URL http://link.springer.com/10.1007/978-1-61779-536-7.

[131] Wolfrum, B. *et al.* Nanoscale Electrochemical Sensor Arrays: Redox Cycling Amplification in Dual-Electrode Systems. *Accounts of Chemical Research* 2031–2040 (2016). URL http://pubs.acs.org/doi/abs/10.1021/acs.accounts.6b00333.

[132] Foulds, I. G., Johnstone, R. W. & Parameswaran, M. Polydimethylglutarimide (PMGI) as a sacrificial material for SU-8 surface-micromachining. *Journal of Micromechanics and Microengineering* **18**, 075011 (2008). URL http://stacks.iop.org/0960-1317/18/i=7/a=075011?key=crossref.ee0ccedf4ac5cbd21f5ced09eb887955.

[133] Chiriacò, M. S. *et al.* Fabrication of interconnected multilevel channels in a monolithic SU-8 structure using a LOR sacrificial layer. *Microelectronic Engineering* **164**, 30–35 (2016). URL http://dx.doi.org/10.1016/j.mee.2016.07.006.

[134] Deleglise, B. *et al.* Synapto-Protective Drugs Evaluation in Reconstructed Neuronal Network. *PLoS ONE* **8**, 1–9 (2013).

[135] Robinson, D. L., Venton, B. J., Heien, M. L. A. V. & Wightman, R. M. Detecting subsecond dopamine release with fast-scan cyclic voltammetry in vivo. *Clinical Chemistry* **49**, 1763–1773 (2003).

[136] Heien, M. L. A. V., Phillips, P. E. M., Stuber, G. D., Seipel, A. T. & Wightman, R. M. Overoxidation of carbon-fiber microelectrodes enhances dopamine adsorption and increases sensitivityElectronic supplementary information (ESI) available: National Instruments Data Acquisition System. See http://www.rsc.org/suppdata/an/b3/b307024g/. *The Analyst* **128**, 1413 (2003). URL http://xlink.rsc.org/?DOI=b307024g.

[137] Legault, M., Rompre, P. P. & Wise, R. A. Chemical stimulation of the ventral hippocampus elevates nucleus accumbens dopamine by activating dopaminergic neurons of the ventral tegmental area. *The Journal of neuroscience : the official journal of the Society for Neuroscience* **20**, 1635–42. (2000).

[138] Cheng, B.-C., Chang, C.-P., Liu, W.-P. & Lin, M.-T. Both mild hypothermia and dopamine D2 agonist are neuroprotective against hyperthermia-induced injury in PC12 cells. *Neuroscience Letters* **443**, 140–144 (2008). URL https://www.sciencedirect.com/science/article/abs/pii/S0304394008010781{#}aep-abstract-id10.

[139] Velnar, T., Bailey, T. & Smrkolj, V. The Wound Healing Process : an Overview of the Cellular and Molecular Mechanisms. *The Journal of International Medical Research* **37**, 1528–1542 (2009).

[140] Sixt, M. Cell migration: Fibroblasts find a new way to get ahead: Figure 1. *The Journal of Cell Biology* **197**, 347–349 (2012). URL http://www.jcb.org/lookup/doi/10.1083/jcb.201204039.

[141] Shreiber, D. I., Enever, P. A. & Tranquillo, R. T. Effects of PDGF-BB on Rat Dermal Fibroblast Behavior in Mechanically Stressed and Unstressed Collagen and Fibrin Gels. *Experimental Cell Research* **266**, 155–166 (2001). URL http://linkinghub.elsevier.com/retrieve/pii/S0014482701952085.

[142] Colpitts, C., Ektesabi, A. M., Wyatt, R. A., Crawford, B. D. & Kiani, A. Mammalian fibroblast cells avoid residual stress zone caused by nanosecond laser pulses. *Journal of the Mechanical Behavior of Biomedical Materials* **74**, 214–220 (2017). URL http://dx.doi.org/10.1016/j.jmbbm.2017.06.005.

[143] Wu, J. *et al.* Gradient biomaterials and their influences on cell migration. *Interface Focus* **2**, 337–355 (2012).

[144] Parkinson, C. Remarks on the Motility and Thermotactic Response of Fibroblasts* (1983).

AUTHOR'S LIST OF PUBLICATIONS (PEER-REVIEWED JOURNAL)

- Ka My Dang, Philipp Rinklin, Jan Schnitker, Bastian Haberkorn, Kathrin Zobel, Simona Gribaudo, Anselme L.Perrier, Jorne Carolus, Michaël Daenen, Stefan Weigel, Harald Luksch, Andreas Offenhäusser and Bernhard Wolfrum, Fabrication of precisely aligned microwire and microchannel structures: Toward heat stimulation of guided neurites in neuronal culture. *Physica Status Solidi (a)*, (214), No.9, 1600729 (2017). DOI: 10.1002/pssa.201600729

- K.M. Dang, P. Rinklin, D. Afanasenkau, G. Westmeyer, T. Schürholze, S. Wiegand and B. Wolfrum, Chip-based heat stimulation for modulating signal propagation in HL-1 cell networks. *in submission*

CONFERENCE PRESENTATIONS

- **Ka My Dang**, Philipp Rinklin, Nouran Adly, Korkut Terkan, Leroy Grob, Sabine Zips, and Bernhard Wolfrum, Thermals stimulation of cells, *International Winterschool on Bioelectronics 2018, Hirschegg, Austria*.
- **Ka My Dang**, Philipp Rinklin, Dzmitry Afanasenkau, Gil Westmeyer, Tobias Schrholz, Simone Wiegand and Bernhard Wolfrum, Chip-Based Heat Stimulation for Modulating Signal Propagation in HL-1 Cell Networks, *Bernstein Workshop 2018 in Tutzing*.
- **Ka My Dang**, Philipp Rinklin, Harald Luksch, Stefan Weigel and Bernhard Wolfrum, Towards heat stimulation of guided neurites growing inside microchannels, *Bernstein Workshop 2017 in Tutzing*.
- **Truong Ka My Dang**, Philipp Rinklin, Jan Schnitker, Bastian Haberkorn, Kathrin Zobel, Simona Gribaudo, Anselme L.Perrier, Jorne Carolus, Michal Daenen, Stefan Weigel, Harald Luksch, Andreas Offenhusser and Bernhard Wolfrum, Microwire array device for investigation of temperature-dependent neurite outgrowth in microchannel, *Enfi Conference 2016 in Berlin*.
- **Truong Ka My Dang**, Philipp Rinklin and Bernhard Wolfrum, Mechano and thermal stimulation of TRP channels, *International Winterschool on Bioelectronics 2016, Hirschegg, Austria*.

ACKNOWLEDGMENTS

First, I would like to express my gratefulness to my supervisor **Prof. Dr. Bernhard Wolfrum**, who has supported me throughout my PhD study with his patience, motivation, and immense knowledge. His guidance helped me overcome all the challenges during my PhD time and inspired me to do the research. I highly appreciate to learn that from my supervisor.

Second, I would like to thank **Prof. Dr Oliver Hayden** for kindly taking over the role of the second examiner of my work.

Third, I would like to send my sincere thanks to **Dr. Philipp Rinklin** for his invaluable support in every fields from biology to engineering. I learned a lot from him. I am thankful for his patience to give valuable comments in this thesis. His encouragement and great advice have been great helps in my PhD study.

Also, I wish to thank **Prof. Andreas Offenhäuser**, who provided me an opportunity to join his team in Forschungszentrum Jülich. This gave me the access to the laboratory and clean room facilities in my first year of PhD research. Here, I also would like to thank all the colleagues in PGI-8/ICS-8 institute for supporting and helping me in this time. In particular, **Marko Banzet** helped me in cleanroom processing and **Elke Brauweiler-Reuters** helped me for SEM images.

I would like to thank my colleagues in Neuroelectronics group, who create a pleasure-working environment and are always willing to support me. My special thanks goes to you all for such an excellent cooperation and for all of the given opportunities to conduct my research.

My special thanks are extended to all the colleagues in Bioengineering institute, who provided a cheerful atmosphere for me every time I come to work. Specifically, my thanks goes to **Josef Hintermair**, who helped me a lot in Biolab, **Dr. Kaye Morgan**, who gave me useful advice in image processing, and **Cagdas Ulas**, who introduced me the optical flow method. Moreover, I also want to thank **Anja Drescher** and **Ulrich Wanka**, who always bring joys and fun in my "Pause" time.

Last but not least, I would like to thank my family: my parents and my sister for supporting me spiritually throughout my PhD study and my life in general.